A Comprehensive Electromagnetic Analysis of AC Losses in Large Superconducting Cables

by

Yu Ju Chen

S.B., Massachusetts Institute of Technology (1990)
S.M., Massachusetts Institute of Technology (1990)

Submitted to the Department of Electrical Engineering and Computer Science
in partial fulfillment of the requirements for the degree of

Doctor of Philosophy in Electrical Engineering

at the

MASSACHUSETTS INSTITUTE OF TECHNOLOGY

September 1996

Author .....
Department of Electrical Engineering and Computer Science
September 4, 1996

Certified by .....
Jeffrey P. Freidberg
Professor
Thesis Supervisor

Accepted by .....
Frederic R. Morgenthaler
Chairman, Departmental Committee on Graduate Students

A Comprehensive Electromagnetic Analysis of AC Losses in Large Superconducting Cables

by

Yu Ju Chen

Submitted to the Department of Electrical Engineering and Computer Science
on September 4, 1996, in partial fulfillment of the
requirements for the degree of
Doctor of Philosophy in Electrical Engineering

Abstract

The issue of AC losses in full-size superconducting cables has been explored both theoretically and computationally in this thesis. A substantially accurate model is presented which captures the dominant physical behavior of a composite superconductor, whether it be a single multifilamentary strand or a large cable.

A set of analytic solutions, the first of its kind available, has been derived for a wide range of geometries. In the process, there is a formal proof that twisting filaments or strands reduce losses. The effect of cable terminations on current distribution and loss has been outlined and a criterion is given for determining the regions of validity for the infinite cable assumption. This assumption, in turn, lays the foundation for the implementation of the computational part of the thesis.

A nonlinear 2D computer program, which takes into the effect of superconducting saturation, has been developed and implemented. As a result, current distribution and loss profiles of a multifilamentary strand can be solved with great accuracy and efficiency, thereby adding new capabilities in the analysis of losses in multifilamentary strands.

A 3D code, tailored to the geometry of the proposed ITER cable-in-conduit conductor (CICC), is the final contribution of this thesis. The need to accurately describe the geometry of the CICC lead to the cable winder algorithm. From the derived strand trajectories, the 3D code produces current distributions and losses for transverse magnetic fields. Loss characteristics were compared against available experimental data. A new set of results and design recommendations emerged from the analysis.

Thesis Supervisor: Jeffrey P. Freidberg
Title: Professor

Acknowledgments

I would like to thank Prof. Jeff Freidberg, for which this thesis would not have been possible without his guidance and support.

I would also like to thank Prof. Richard Thornton and Dr. Bruce Montgomery for providing me with the opportunity to work on superconducting magnets. I consider myself fortunate for having been able to work on interesting projects such as MAGLEV and fusion.

Thanks go to Prof. Jacob White for taking time out of his busy schedule to be one of my thesis readers.

Throughout my years at MIT, I have made some great friends. Kudos go to Grundy for helping me out with some of the figures in this thesis. I am also grateful to my good friend up north, Alain (sheema) for some fruiftful technical discussions. And there is, of course, the people I befriended at Ashdown: my original dorm-mates, Karin and Anne, and of course my Athena buddy, JP, who followed me home after my PWE's. Gratitudes to my sisters-in-arms, Meechoo, Sue, Steph, for all those female-bonding sessions. I also have to thank Matt and Shiufun for all the times they put up with me being in their suite - all those TV nights have finally paid off! Finally, I want to thank my friends from undergraduate (Andrew, Jo, Wendy, Ting, Illy, Suz, etc.) for being such good friends during my undergraduate years here. Special thanks go to Lisa for being such a wonderful supportive friend and for always being there to share my experiences with me.

Last, but not least, I want to thank my parents for making me who I am - to my father who sparked my interest in the sciences and to my mother who always had faith and was always there to take care of me.

Contents

1 Introduction to AC losses **13**

1.1 Loss mechanisms in superconductors 16

1.2 Literature Survey 17

1.3 Scope of the thesis 20

2 The Model **25**

2.1 Field Distribution in Magnet Windings 26

2.1.1 Solenoids 26

2.1.2 Toroids 27

2.2 Ordering system 27

2.3 Governing equations 29

2.4 Constitutive relations 32

2.5 Formulation of Boundary Conditions 34

2.5.1 Magnet connected to a current source 34

2.5.2 Magnet in persistent mode 45

2.6 Conclusion 49

3 Analytic Results of Limiting Cases **51**

3.1 Open-circuited straight cable 51

3.2 Short-circuited current loop 57

3.2.1 Untwisted wires 57

3.2.2 Twisted wires 62

3.3 Finite length twisted cable 68

3.3.1 Short-circuited ends 68
3.3.2 Open-circuited ends 70
3.3.3 Short length limit 72
3.3.4 Long length limit 74
3.4 Conclusion 75

4 2D code **83**
4.1 Numerics 84
4.2 Benchmark cases 90
4.2.1 Case 1: Linear conductivity 91
4.2.2 Case 2: Wire with thin normalconducting shell 92
4.2.3 Case 3: Multilayer wire - SSC NbTi strand 93
4.2.4 Case 4: Field ramp with transport current 101
4.3 Conclusion 103

5 3D code **111**
5.1 The Cable Winder 112
5.1.1 The algorithm 112
5.1.2 Results of cable winder 118
5.1.3 Analytic model of $\rho\dot{\psi}$ 127
5.2 Governing equations for the ITER cable 129
5.3 Numerical strategy 132
5.4 Results 140
5.4.1 Field and Loss Profiles 148
5.4.2 Loss data 157
5.5 Design Recommendations 162
5.6 Conclusion 166

6 Conclusion **169**
6.1 Summary 169
6.2 Concluding remarks 172

List of Figures

1-1 Flux pinning vortices in type II superconductors 13

1-2 Pictures of single strand conductors 14

1-3 Sketch of different types of cables. 15

2-1 Flux lines in short solenoid magnet. 27

2-2 Definite of coordinate system 35

2-3 Prototype of ITER joint sample 41

2-4 Model of joint 42

2-5 Sketch of persistent loop 46

2-6 Model of persistent joint 48

3-1 Untwisted finite length cable. 52

3-2 Transport current loss for a persistent loop. 78

3-3 Dipole current loss for a persistent loop. 78

3-4 Transverse ac loss currents in single twist pitch cable 79

3-5 Current density for short and open-circuit ended cables 80

3-6 Loss for short-ended cable 81

3-7 Loss for open-ended cable 82

4-1 Schematic of multilayer strand 104

4-2 $E_{||}$: comparison of analytic and code-generated results 105

4-3 E_{ϕ} 106

4-4 E_{r} 106

4-5 Power loss in strand with outer shell 107

4-6 Picture of NbTi strand 108
4-7 Power loss of NbTi strand in ripple field 109
4-8 Transport current profile as affected by $\dot{B}$ 110

5-1 Cross-sectional view of ITER cable. 112
5-2 Winding process of ITER cable 113
5-3 Pictorial of cable winder algorithm 117
5-4 Strand locations in a leaflet 119
5-5 Path of a strand through the cable 120
5-6 $\dot{\rho}_i$ 121
5-7 $\rho\dot{\psi}_i$ 122
5-8 $\dot{\rho}$ in global coordinate 123
5-9 $\rho\dot{\psi}$ in global coordinate 124
5-10 α - the radial profile of $\rho\dot{\psi}$ 126
5-11 Top view of cable - verification of α 126
5-12 Radial profile of $\dot{\rho}$ 128
5-13 Comparison of analytic model with data of $\rho\dot{\psi}$ 130
5-14 Saturated vs. non-saturated power loss for $\dot{B}$= 1T/s 141
5-15 Saturated vs. non-saturated power loss for $\dot{B}$= 10T/s 141
5-16 $E_{||}$ and E_r profiles without α noise 144
5-17 Illustration of α noise 145
5-18 Mean-squared noise of α vs. radius of cable. 147
5-19 Cross-sectional profile of $E_{||}$ 149
5-20 Cross-sectional profile of E_ϕ 150
5-21 Cross-sectional profile of E_r 151
5-22 Cross-sectional profile of E_r 152
5-23 Cross-sectional profile of power density 153
5-24 p_d as function of $\sigma_\perp$ 154
5-25 p_d as function of $\dot{B}$ 154
5-26 p_d as function of t 155

5-27 Excitation field waveforms for benchmark experiment 159
5-28 Experimental data for sawtooth waveform 160
5-29 Experimental data for sine wave 161
5-30 Schematic depiction of the interplay between the fourth and fifth stage. 163
5-31 α profile of recommended ITER cable design. 164
5-32 $\dot{\rho}$ profile of recommended ITER cable design. 164
5-33 Power loss vs. time for recommended ITER cable design. 165
5-34 Region of zero-crossing 167

List of Tables

1.1 List of superconducting magnet applications 16

3.1 A table of analytic results for different conductor geometries and end conditions. 77

5.1 Specifications of ITER cable 114

5.2 Results using different number of harmonics for $E_{||}$ and Φ 147

Chapter 1

Introduction to AC losses

Since the discovery of the phenomenon of superconductivity in 1911 [1], there has been ongoing research to develop applications to utilize superconducting properties. As a result, there have been many types of materials and engineering products developed. This thesis is concerned with applications which utilize superconductors as large scale conductors.

Naturally occuring elements such as mercury fall into what are termed *type I* superconductors. These conductors, when cooled below a critical temperature and subjected to a magnetic field less than the critical field, expel flux by means of a very

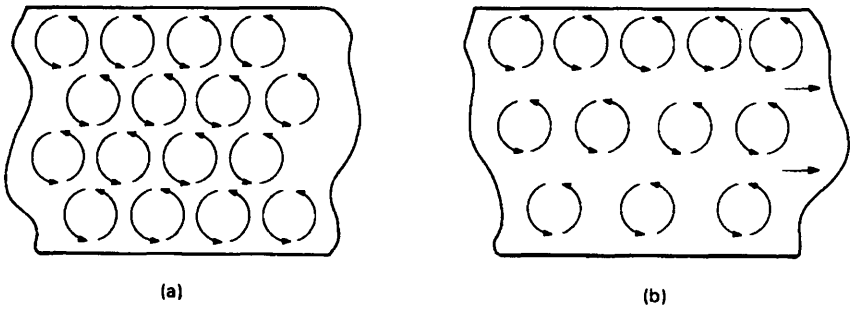

Figure 1-1: (a) A uniform array of vortex currents produces no net current density but (b) a gradient in the density of vortex currents produces a net current

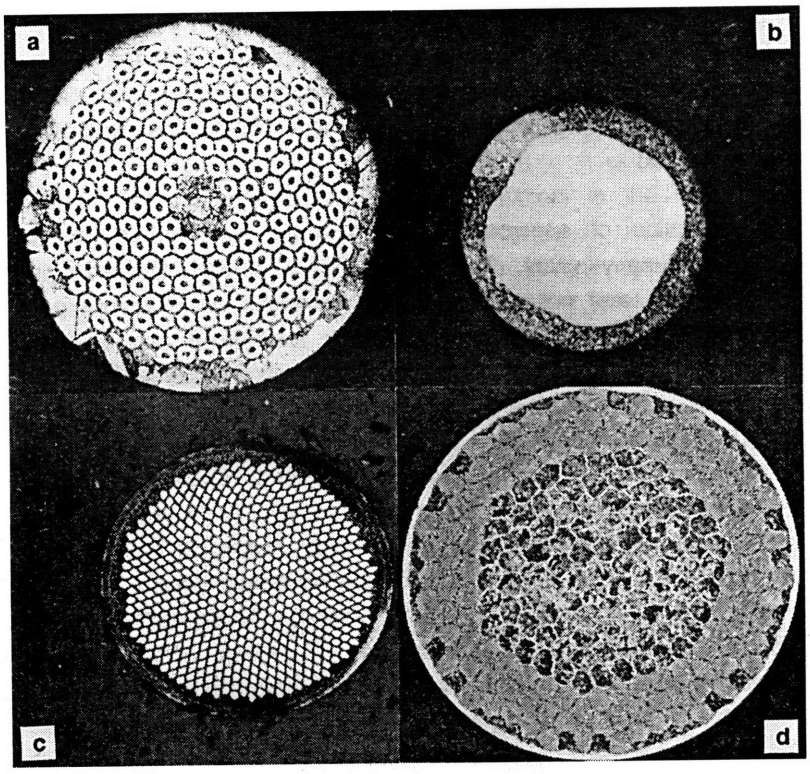

Figure 1-2: Several composite conductors: (a) Nb_3Sn multifilamentary conductor (b) NbTi monofilament conductor (c) Classical NbTi conductor (574 fil.) (d) AC conductor($\tilde{1}$5k fil.)

thin surface current. This phenomenon is termed the "Meissner" effect. Another class of bulk superconductors called *type II* superconductors operate in a "mixed state" by allowing a much larger magnetic field to penetrate before it becomes normal. This is made possible by the presence of flux pinning vortices. These "fluxoids" produce vortex currents as shown in Fig. 1-1. A gradient on the density of these currents produce a net current *inside* the conductor, not just on the surface. This is what allows the external magnetic field to penetrate the conductor and result in a much higher critical field. The composite conductors mentioned in this thesis use type II bulk superconductors.

The first application of superconductors involved magnets which were made of

Nb_3Sn thin tapes in 1957. In 1963, the first NbTi monofilament strands were produced. For stability reasons, these monofilament strands became multifilaments embedded in a normal conducting metal base (see Fig. 1-2). To reduce losses, the multiple filaments were also twisted.

For large systems, high-current cables were developed. These cables are manufactured from many multifilamentary strands. The following two types of cables are often used:

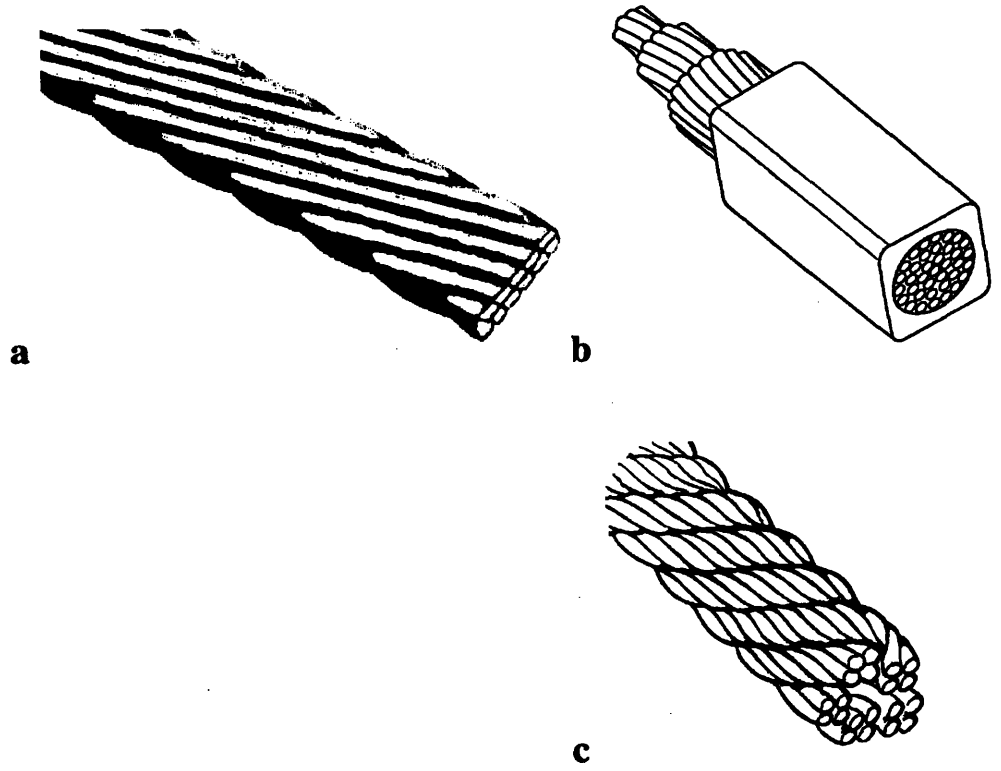

Figure 1-3: (a) 11-strand Rutherford-type cable (b) Cable-in-conduit conductor (c) Cable without a jacket.

- Rutherford cables (see Fig. 1-3(a)) are flat multi-strand cables. Because Lorentz forces can displace strands which in turn can cause quenches, these cables are packed tightly (90% fill fraction).

Application		Conductor	Max. field on conductor [T]	Field-sweep rate [T/s]
Solenoids	Small bore	W	20	10^{-2}
	Large bore	C	15	small
NMR		W	20	small
Fusion	Toroidal coil	CIC	13	0.1-10
	Transformer coil	CIC	13	0.1-10
High-energy physics	Beam-guiding	RC	12	10^{-2}
	Detectors	C	6	small
MRI		W	0.5-2	10^{-3}
SMES	Pulsed	C,RC	5-10	10^{3}-10^{4}
	Low frequency	C,RC	5-10	small
MAGLEV		W	5	0-10
DC motors		RC	2-5	small
AC generators		RC	2-6	10
Magnetic separation		C	8	small
MHD		RC	8	small

Table 1.1: The main characteristics of superconducting magnets. W=wire, RC=Rutherford-type cable, CIC=cable-in-conduit, C=cable without jacket.

- The cable-in-conduit conductor (CICC) as shown in fig. 1-3(b) is manufactured in several stages, each stage with its own sub-bundles twisted together. An incoloy jacket supports the conductor and contains the liquid helium. The forced flow cooling gives additional heat transfer inside the cable.

The main applications for superconducting magnets are outlined in Table 1.1. In this thesis the emphasis is on the electromagnetic properties of circular multi-strand cables such as the CIC conductor used in fusion machines and on proposed magnetically-levitated (MAGLEV) trains.

1.1 Loss mechanisms in superconductors

When the transport current inside a superconductor and/or the magnetic field it experiences do not vary with time, there is no power loss. This is a primary reason for using superconductors. With a time-varying magnetic field and/or transport

current, electric fields are induced and joule heating ensues. These losses demand more refrigeration or in worse cases, they may be the culprit to quenches in the system. There are three major types of losses - loss due to magnetization in the bulk superconductor, resistive loss due to coupling currents flowing in the normal metal region of the composite conductor (across the copper matrix inside a strand or strand-strand current via contact conductance), and loss incurred by transport current when it experiences a finite resistance.

Magnetization or hysteretic loss is well-understood and predictable [29][11]. Since these losses occur in the filaments, their magnetization effect is small. The maximum magnetization M_p of a round filament is $\frac{4}{3\pi}\mu_0 J_c a$ where J_c is the critical current density and a the filament radius. Typical values of J_c =1×10^{9}A/m^3 and $a = 1\mu$m give $M_p = 5.33 \times 10^{-4}$T, which is negligible.

Therefore, the objective of this thesis is to develop and analyze models which predict the AC losses caused by electric fields and currents flowing macroscopically in and between strands in multistrand CICC. The losses predicted by this model can aid in the design of the refrigeration system, in future cables, or in predicting possible quench mechanisms. The current distributions and time dependence behavior obtained from the model can shed light on ramp-rate limitations of magnets which require fast ramp rates (for instance, the central solenoid of a fusion reactor like ITER).

1.2 Literature Survey

Current redistribution in full-size cables, as applicable to the calculation of AC losses and stability, has not as yet been adequately treated in the literature. Methods vary in sophistication, from one as simple as that used in the ITER coil design guidelines [7]

to a full-scale electromagnetic treatment of the problem as presented in a paper from the University of Twente [10].

It has been experimentally observed that the rate of decay of induced currents inside these superconducting cable is orders of magnitude longer than that of a single strand. It is thus safe to say that the behavior of a cable is a far departure from that of a strand. There are two major differences. First of all, the geometry of a cable is more complicated. The strands not only twist helically but transpose on each other radially. A wire that is skirting the perimeter of the cable at some position along the cable may find itself somewhere near the center or even on the other side further down the length of the cable.

The other major difference is in the ratio of the parallel conductivity to the perpendicular conductivity. In a strand, when a filament saturates, the current flows at critical current density and any excess current will spill into the next filament or into the copper matrix surrounding it. The perpendicular conductivity is simply equal to some fraction of the conductivity of copper. In other words, in the saturated region(s) of a strand, due to competing conductivities in the parallel and perpendicular direction, large transverse fields and currents are induced. In the case of a cable, when a strand saturates, the remaining current will spill into the normal metal region of the strand or transfer to a neighboring strand via the interstrand conductivity. However, unlike filaments in a strand, the transverse interstrand conductivity is orders of magnitude smaller than for copper. Even in saturation, it is much smaller than the parallel conductivity of the strand. Under these conditions, parallel fields will remain small compared to their transverse counterpart. Even more importantly, because the transverse currents are also small, one sees a much smaller shielding effect than in the single strand. The following section briefly outlines the existing literature which attempt to solve for losses in a complex cable.

For the proposed ITER coil, the formulae most commonly used to calculate coupling loss due to strand-to-strand contact are the same as those used for a single strand. They are simple and fully analytic, and use an experimentally derived time constant and unknown geometric factor, $n\tau$, of the cable. Because it is essentially only an equation for power dissipation, no insight into the current distribution of the cable can be gleaned from this calculation.

Turck [8] and Ciazynski [2] evaluate the current distribution of two twisted strands. Their model consists entirely of discrete circuit elements. They calculate the self-inductance of the wires, the mutual inductance between them, and model the contact resistance with resistors periodically placed along the length of the twisted strands. From the behavior of two twisted strands, they extrapolate an estimate of the current transfer behavior within the ITER cable.

Several papers from Japan [5] [6] and one by Egorov [3], use the same approach in solving for AC losses caused by interstrand coupling. They all obtain analytical solutions for the voltage induced in each of these strands by a uniform transverse magnetic field. From these voltages, one can find the voltage drop across two adjacent strands to calculate the amount of interstrand coupling current. In [5], they examine three and seven strands twisted together. Egorov treats the interstrand currents for the entire cable with the same method. Similarly in [6], the voltage induced in the strands are used to calculate interstrand current distibutions. They find, via the finite element method, the current distribution in the normal metal region of the strand which surrounds the filament region.

They were able to obtain an analytical solution for the induced voltages by assuming that the electric field along these strands is zero. The magnetic field distribution is assumed to be constant across the cross-section and along the length of the braided strands, i.e. no induced magnetic fields are included in these analyses. Because any

shielding effects are neglected, the field in the structure is equal to the applied field. These assumptions are valid for relatively small or slow field variations. In addition, the limited number of wires in their model makes the assumption of negligible induced magnetic fields reasonable. Finally, the complex effect of transport current on current distribution was not fully discussed in either of these papers.

The work from the University of Twente is the first to attempt to solve the complete AC loss and stability problem in full-sized cables [9] [13]. Discrete circuit equations are used to model the cable. A simple relationship between V and I for a single strand is used to capture the nonlinear behavior of the superconducting strands. This V vs. I relationship is crucial to modelling if and when wires in the cable saturate. L.J.M. van de Klundert reports that due to the wires' non-linear behavior and strong dependence on $\frac{dB}{dt}$, the solutions are difficult to obtain [9]. A. Verweij [18] recently published a Ph.D thesis on the analysis of Rutherford cables used in accelerator magnets. No definitive electromagnetic model of full-size three dimensional cables have as yet been reported.

The estimates on the AC losses in CICC are contingent on an experimentally derived parameter, the time constant. In order to predict the behavior of a system, one should rely solely on physical parameters to make an estimation. The time constant should be part of a set of results, not the means to a result. In other words, at the present time, there in no direct way to reliably estimate AC losses given the available analytical and numerical tools. This is the prime motivation for the thesis.

1.3 Scope of the thesis

Our model is philosophically most similar to the work done at the University of Twente. The major difference is that our model is spatially continuous and thus

uses E's and J's versus V's and I's. Another difference in modelling arises from the fact that during manufacturing of cables, the substages are compressed to fit through specified die sizes. This results in strands that do not necessarily rotate around fixed radii. Our model can trace through the current paths of each strand in the cable. From the strand trajectories, one can then solve for the field distribution inside the cable.

The next chapter describes the model we use. It lists the assumptions and ordering system for which the model is based. The ordering is based on a long, thin approximation where the geometry and the excitation source vary slowly in z, the axial coordinate of the conductor. The result is a general set of two coupled differential equations derived from Maxwell's equations with two unknowns: $E_{||}$, the magnitude of the electric field parallel to the superconducting portion of the geometry, and Φ, the transverse potential. The nonlinear constitutive relationship between $\sigma_{||}$ and $E_{||}$ found in Carr [12] and Rem [4] is used in the governing equations. Boundary conditions along the rim and ends of a cylindrical geometry are derived. The model can be applied to a composite conductor of arbitrary geometry, as long as the inner geometry is not too tightly twisted.

In chapter 3, the governing equations and boundary conditions are used to derive analytic results for geometries containing one twist pitch. The tractable solutions are summarized here:

- Infinite length conductor (twisted)
- Infinite length conductor in a closed-loop (twisted)
- Finite length conductor with open ends (untwisted)
- Finite length conductor with open ends (twisted)

- Finite length conductor with shorted ends (twisted)

The analytic results when taken to the appropriate limit match those found in literature. In addition, a constraint on the regime of validity for the infinite cable has been derived. This is important for conducting experiments and for understanding the applicability of theories which use the infinite cable assumption.

Chapter 4 marks the beginning of the computational section of the thesis. With the differential equations, constitutive relations, and boundary conditions derived, a "2D" code was developed and implemented. The purpose of creating this code is to benchmark the model. The code solves for problems in polar coordinates r and ϕ and can be applied to long cables. The numerical strategy for solving the differential equations and for treating the nonlinearity in $\sigma_{||}$ is outlined. A number of cases with various geometries have been used for comparison against both analytic solutions from chapter 3 and well-established literature results.

The problem of the CICC cannot be solved simply by the code described in chapter 4 because the inherent geometry of the cable is three-dimensional. Chapter 5 describes a "3D" code which solves for the current distributions and AC losses given the strand trajectories produced by the cable winder program. The results presented in this chapter are quite surprising. Due to the relationship between the last and the second to last stage twist pitch, a "zero-crossing" phenomenon corresponding to an effective untwisting of the cable appears which results in increased and highly localized joule heating. In addition, a new time constant, τ_l was discovered and it is much larger than the $n\tau$ value extrapolated from experimental energy loss data. This implies that the geometric factor n is much smaller than that for a helically twisted cable. A long time constant can actually be seen in some preliminary AC loss data for a 192-strand cable which is 1/6th the size of the ITER design cable.

An analytic expression was derived to approximate the azimuthal strand trajectory

coefficients. These aided in the conceptual design of a new cable which can potentially yield better performance from an AC loss point of view. The loss results of the recommended design closes the final section of the thesis.

Chapter 2

The Model

A cable is usually built of several stages, each stage consisting of several substages of wires twisted together with its corresponding twist pitch. For most large scale applications, these full-size cables contain on the order of a thousand strands. With such a large number of wires, one is motivated to use a macroscopic continuum approach to solve this structure. Instead of treating each wire discretely, one can model the cross-section as a continuous medium, with "locally averaged" parameters and characteristics. This avoids the gruesome task of finding self and mutual inductances and specifying differential equations for each and every one of the one thousand plus strands in the cable.

The continuum model is coupled with an ordering system which implies all parameters and fields vary slowly with z. This long, thin approximation is applied to Maxwell's equations. A set of coupled differential equations emerge. These equations need to be solved in the two variables $E_{||}$ and Φ. The geometry of the problem is encapsulated in the unit vector $\hat{e}_{||}$. The conductivity of the superconductor, $\sigma_{||}$, is the nonlinear portion of the problem and is explained in section 2.4. Finally, boundary conditions for a circularly shaped cable are derived along with end conditions which

arise from cable-joint interface.

2.1 Field Distribution in Magnet Windings

There are several types of superconducting magnets. Each have their unique field profile which is pertinent to the calculation of AC losses. Whole books have been written on the subject of field calculation so here, only the essentials are outlined. There are two important characteristics of the B-fields inside the magnet windings. In most windings, both the static and the pulsed field are perpendicular to the cylindrical conductor. In addition, if the cross-section of the conductor is small enough compared to the total cross-section of the magnet, it is safe to assume the B-field is uniform across the conductor.

2.1.1 Solenoids

The simplest solenoid is that of the infinitely long one. The field everywhere is in the axial direction, is perfectly uniform across the bore, and falls to zero at the outer edge of the winding. Each section will contribute a field within its own bore of $\Delta B = \mu_0 J \Delta r$ where Δr is the radial thickness of the conductor section. For the nth layer of conductors in the solenoid, the self-field would be $B_0 = \mu_0 n J \Delta r$. If $n >> 1$, then $\Delta B << B_0$.

In coils of finite length, (pancake-wound or racetrack coils would be the extreme cases), the situation becomes much more complicated because of the way in which field lines curve around the ends of the coil. Fig. 2-1 shows the flux line pattern for a short solenoid, together with contours of constant-field amplitude, normalized to the central field.

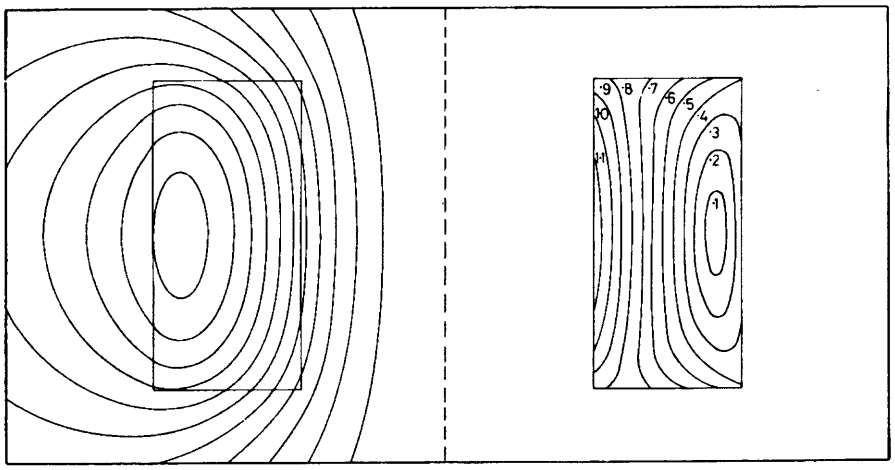

Figure 2-1: Flux lines in short solenoid magnet.

2.1.2 Toroids

Toroidal windings are frequently used in thermonuclear fusion research. Numerical methods must be used when high accuracy is required, when the field must be calculated inside the coils. Again, the fields are predominantly perpendicular to the coils and for thick coils, the B-field across one layer can be to first order considered uniform.

2.2 Ordering system

The current of a strand is written as

$$\bar{J}_{||} = \sigma_{||}\bar{E}_{||} \tag{2.1}$$

$$\bar{J}_{\perp} = \sigma_{\perp}\bar{E}_{\perp} \tag{2.2}$$

Converting to the Eulerian x-y-z coordinate system of the cable, we define a unit vector in the parallel direction to a given strand as shown in fig. 2-2.

$$\hat{e}_{||} = \frac{\dot{X}(x,y,z)\hat{x} + \dot{Y}(x,y,z)\hat{y} + \hat{z}}{(1+\dot{X}^2+\dot{Y}^2)^{\frac{1}{2}}} \tag{2.3}$$

where $\dot{X}$ and $\dot{Y}$ are the x and y component of the directional derivatives of the strand path as it winds down the length of the cable. As mentioned before, these are not constants but functions of x, y, and z. A three-dimensional cable winder program has been developed that traces the position of each strand down the length of the cable for a given set of cable specifications and will be covered in chapter 5. A significant simplification occurs if we make the following assumptions: the twist pitch of any given strand is long compared to its diameter and that the conductivity along the direction of the strand is large compared to the conductivity perpendicular to the strand, as mentioned earlier. If we introduce a small ordering parameter $\epsilon << 1$, then we can define a maximal asymptotic expansion which contains the maximum amount of physics described by these equations.

$$\begin{aligned} \dot{X}, \dot{Y} &\sim \epsilon \\ \frac{\partial}{\partial z}/\nabla_T &\sim \epsilon \\ \frac{\sigma_\perp}{\sigma_{||}} &\sim \epsilon^2 \\ E_z/\left|\bar{E}_T\right| &\sim \epsilon \\ \left|\bar{J}_T\right|/J_z &\sim \epsilon \\ \mu_0\sigma_{||}\frac{\partial}{\partial t}/\nabla_T^2 &\sim 1 \end{aligned} \tag{2.4}$$

Here the subscript T denotes the transverse (x, y) plane. The ordering implies slow variation along z with most of the current in the z direction. The small perpendicular

conductivity implies that the largest component of the electric field is in the transverse direction. For practical situations, only the diffusion time associated with $\sigma_{||}$ may be comparable to the time scale of field variation. The transverse diffusion time associated with $\sigma_{\perp}$ is always very short and can be neglected (assume instantaneous equilibration on the $\sigma_{\perp}$ time scale).

2.3 Governing equations

Using the expansion, the fields and vectors can now be expressed as

$$\hat{e}_{||} \approx \dot{X}\hat{x} + \dot{Y}\hat{y} + \hat{z} \tag{2.5}$$

$$\begin{aligned} \bar{E}_{||} &= (\bar{E} \cdot \hat{e}_{||})\hat{e}_{||} = E_{||}\hat{e}_{||} \\ &\approx (E_z + \dot{X}E_x + \dot{Y}E_y)\hat{e}_{||} \end{aligned} \tag{2.6}$$

$$\begin{aligned} \bar{E}_{\perp} &= \bar{E} - \bar{E}_{||} \\ &\approx E_x\hat{x} + E_y\hat{y} \end{aligned} \tag{2.7}$$

Neglecting the higher order terms in each current component, we have

$$J_x \approx \dot{X}\sigma_{||}E_{||} + \sigma_{\perp}E_x \tag{2.8}$$

$$J_y \approx \dot{Y}\sigma_{||}E_{||} + \sigma_{\perp}E_y \tag{2.9}$$

$$J_z \approx \sigma_{||}E_{||} \tag{2.10}$$

Since the conductivity of the cable is highly anisotropic, one must be careful when solving Maxwell's equations. The quasistatic equations for Ampere's and Faraday's

laws are

$$\nabla \times \bar{E} = -\frac{\partial}{\partial t}\bar{B} \tag{2.11}$$

$$\nabla \times \bar{H} = \bar{J} \tag{2.12}$$

Taking the curl of the first equation, we have

$$\nabla \times \nabla \times \bar{E} = -\mu_0 \frac{\partial}{\partial t}\bar{J} \tag{2.13}$$

In rectangular coordinates, the above equation is broken down into three equations, two corresponding to the transverse components (x and y) and one corresponding to the longitudinal component z.

$$\nabla^2 \bar{E}_T - \nabla_T \nabla \cdot \bar{E} = \mu_0 \frac{\partial}{\partial t}\bar{J}_T \tag{2.14}$$

$$\nabla^2 E_z - \frac{\partial}{\partial z}(\nabla \cdot \bar{E}) = \mu_0 \frac{\partial}{\partial t} J_z \tag{2.15}$$

Introducing the asymptotic expansion and neglecting all second order terms reduces the above equations to

$$\nabla_T^2 \bar{E}_T - \nabla_T \nabla_T \cdot \bar{E}_T = 0 \tag{2.16}$$

$$\nabla_T^2 E_z - \frac{\partial}{\partial z}\nabla_T \cdot \bar{E}_T = \mu_0 \frac{\partial}{\partial t} J_z \tag{2.17}$$

Rewriting the two components of the transverse equation gives

$$\begin{aligned} \frac{\partial}{\partial y}\left(\frac{\partial}{\partial y}E_x - \frac{\partial}{\partial x}E_y\right) &= 0 \\ -\frac{\partial}{\partial x}\left(\frac{\partial}{\partial y}E_x - \frac{\partial}{\partial x}E_y\right) &= 0 \end{aligned} \tag{2.18}$$

These two equations yield the single piece of information that $\frac{\partial}{\partial y}E_x - \frac{\partial}{\partial x}E_y = f(z,t)$. We assume that no zeroth order parallel B_z is present, which is usually a good approximation when only a purely transverse field is applied. Hence, the free integration function $f(z,t) = 0$.

We can thus define a pseudo potential function Φ to reduce the number of unknowns.

$$\bar{E}_T(x,y,z,t) = -\nabla_T \Phi(x,y,z,t) \tag{2.19}$$

At this point, we have two unknowns (E_z and Φ) and one unsatisfied equation (the $\nabla_T^2 E_z$ equation). The remaining equation results from annihilating the redundancy in the two components of the $\nabla_T^2 E_T$ equations. This is accomplished by forming the operation $\nabla \cdot \bar{J} = 0$ to obtain the second equation. We have

$$\frac{\partial}{\partial x}(\dot{X}\sigma_{||}E_{||} + \sigma_{\perp}E_x) + \frac{\partial}{\partial y}(\dot{Y}\sigma_{||}E_{||} + \sigma_{\perp}E_y) + \frac{\partial}{\partial z}\sigma_{||}E_{||} = 0 \tag{2.20}$$

where $E_{||} = E_z + \dot{X}E_x + \dot{Y}E_y$ replaces E_z as one of the dependent variables.

Substituting the potential function into the two differential equations 2.17 and 2.20 yields

$$\nabla_T^2(E_{||} + \dot{X}\frac{\partial}{\partial x}\Phi + \dot{Y}\frac{\partial}{\partial y}\Phi + \frac{\partial}{\partial z}\Phi) = \mu_0 \frac{\partial}{\partial t}\sigma_{||}E_{||} \tag{2.21}$$

$$\nabla_T \cdot \sigma_{\perp}\nabla_T\Phi = \nabla \cdot (\sigma_{||}E_{||}\hat{e}_{||}) \tag{2.22}$$

These two equations will in general have to be solved numerically for Φ and $E_{||}$. Keep in mind that $\sigma_{\perp}$ can also be variant in space. The solution of the electric field gives rise to the current distribution. The power dissipated per unit volume is simply the

sum of the two components of $\bar{E} \cdot \bar{J}$.

$$\begin{aligned} p_d &= \sigma_{||} E_{||}^2 + \sigma_{\perp} E_{\perp}^2 \\ &= \sigma_{||} E_{||}^2 + \sigma_{\perp} (\nabla_T \Phi)^2 \end{aligned} \tag{2.23}$$

2.4 Constitutive relations

Much like W. Carr's [12] continuum model for the single strand, fields, currents and physical properties are averaged over a representative local cross-section of the cable. For well-defined boundary conditions, Maxwell's equations can be solved for the fields and currents. The V vs. I constitutive relation for a single strand has been explored in-depth by L.J.M. van der Klundert [9] and a variation of it will be used in our model. The derivation is not explained in depth here but can be found in [4].

Under normal operating conditions, a superconducting strand has very low loss and a very high conductivity associated with it. In some analysis, the conductivity is assumed to be infinite. However, there is a dynamic resistivity associated with superconductors under AC conditions that gives these strands an effective finite conductivity. Once the entire strand reaches its critical current density, it saturates. Any current above the critical current flows into the normal metal region surrounding the saturated filaments. Therefore, the longitudinal or parallel conductivity is piecewise linear and is expressed as follows

$$J_{||} = (1 - \lambda_v) \begin{cases} \left(\frac{\lambda j_c}{\varepsilon_0} + (1 - \lambda) \sigma_m \right) E_{||} & \text{if } \left| J_{||} \right| \leq \lambda j_c + (1 - \lambda) \sigma_m \varepsilon_0 \\ \lambda j_c \text{sign}(E_{||}) + (1 - \lambda) \sigma_m E_{||} & \text{if } \left| J_{||} \right| \geq \lambda j_c + (1 - \lambda) \sigma_m \varepsilon_0 \end{cases} \tag{2.24}$$

where

$\varepsilon_0 = \frac{8}{3\pi}\dot{B}R_f$

$\dot{B} \equiv$ time-varying magnetic field

$R_f \equiv$ filament radius

$\sigma_m \equiv$ conductivity of strand matrix

$j_c(B,T) \equiv$ critical current density dependent on B-field and temperature

$\lambda \equiv$ fraction of superconductor volume in strands

$\lambda_v \equiv$ void fraction of cable

If one looks at a typical cross-section of a cable, one can see that the current in each strand is flowing predominantly in the z-direction. However the transverse component of these currents (although small) is almost haphazard. Unlike filaments in the strand, there are several twist pitches involved and therefore, the current directions are not constant throughout the cross-section of the cable. This implies that the anisotropy in the conductivity is non-uniform in space. There are thus two different coordinate systems to keep in mind - the local coordinate system following the strand (Lagrangian) and the global coordinate system of the cable (Eulerian). The conductivity of the cable is naturally defined in terms of the local coordinate system, with two components - parallel to the strand and perpendicular to the strand. Here, the conductivities are denoted by $\sigma_{||}$ and $\sigma_{\perp}$ respectively. Ultimately, it must be expressed in terms of the global coordinates in order to obtain a solution to the problem. It is assumed that the individual components of the conductivity are constant over a local cross-sectional area representing the fractional area of each strand. From eqn. 2.24, $\sigma_{||}$ is given by

$$\sigma_{||} = (1-\lambda_v)\begin{cases} \frac{\lambda j_c}{\varepsilon_0} + (1-\lambda)\sigma_m & \text{if } \left|E_{||}\right| \leq \varepsilon_0 \\ \frac{\lambda j_c}{\left|E_{||}\right|} + (1-\lambda)\sigma_m & \text{if } \left|E_{||}\right| \geq \varepsilon_0 \end{cases} \tag{2.25}$$

$\sigma_\perp$ is deduced from measured transverse resistances of the cable. In general $\sigma_\perp << \sigma_m$ because of strand coatings, contact resistance, and only partial contact between adjacent strands. The complexity of the problem is partially associated with the nonlinearities and anisotropy of the conductivity matrix, although perhaps more important is the complicated and convoluted geometry associated with variation of the local parallel and perpendicular geometry.

2.5 Formulation of Boundary Conditions

2.5.1 Magnet connected to a current source

Boundary condition on perimeter of cable

For treatment of a circularly shaped cable, all of the parameters are converted to polar coordinates. The coefficients are now defined as (see fig. 2-2)

$$\dot{\rho}(x,y,z) = \dot{X}\cos\phi + \dot{Y}\sin\phi \tag{2.26}$$

$$\rho\dot{\psi}(x,y,z) = -\dot{X}\sin\phi + \dot{Y}\cos\phi \tag{2.27}$$

where $\dot{\rho}$ and $\rho\dot{\psi}$ are the $\hat{r}$ and $\hat{\phi}$ components of a strand path as it traverses down the length of the cable. The reason for the different notation is to keep the coordinates of the cable separate from the local coordinate system of each strand.

The governing equations are now

$$\nabla_T^2(E_{||} + \dot{\rho}\frac{\partial}{\partial r}\Phi + \frac{\rho\dot{\psi}}{r}\frac{\partial}{\partial\phi}\Phi + \frac{\partial}{\partial z}\Phi) = \mu_0\frac{\partial}{\partial t}\sigma_{||}E_{||} \tag{2.28}$$

$$\nabla_T\cdot\sigma_\perp\nabla_T\Phi = \frac{1}{r}\frac{\partial}{\partial r}r(\dot{\rho}\sigma_{||}E_{||}) + \frac{1}{r}\frac{\partial}{\partial\phi}(\rho\dot{\psi}\sigma_{||}E_{||}) + \frac{\partial}{\partial z}\sigma_{||}E_{||} \tag{2.29}$$

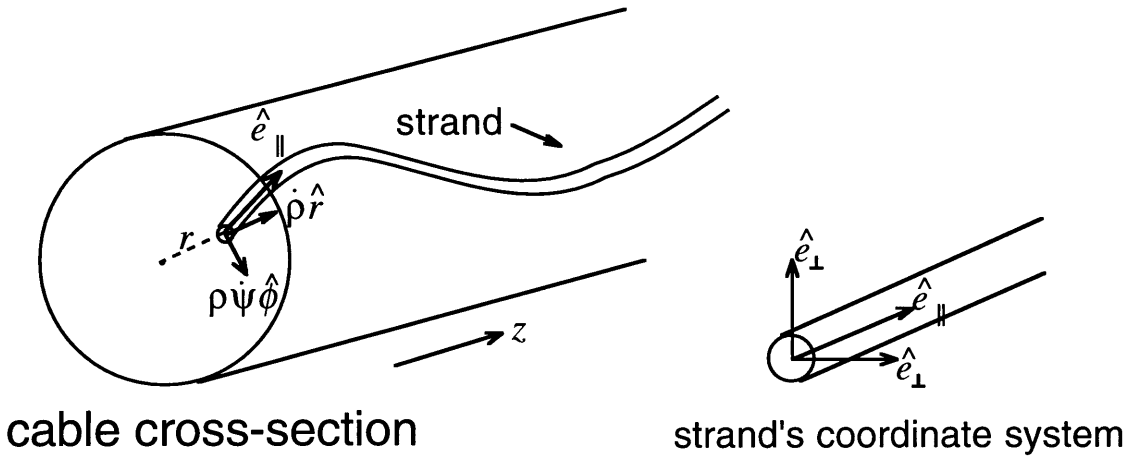

Figure 2-2: Definition of coordinate system and vector components.

So far we have the differential equations to solve for the electric field. We need boundary conditions to complete the formulation.

Boundary conditions for a range of magnet operations must be accurately specified in order to achieve solutions that make physical sense. Modes of operation vary from current loops running in persistent mode (MAGLEV) with a highly conducting switch to a cable connected to a source with finite impedance (e.g. fusion application magnets) to a completely open-circuited section of cable often used in AC loss experiments. At first glance, it seems that a new set of boundary conditions is required for each specific case. Fortunately, this is not necessary. In fact, with some realistic assumptions, a *general* set of radial boundary conditions can be derived for the electric fields at the perimeter of the cable. It is only the boundary conditions at the *ends* that need to be specified for each separate case.

The total magnetic field is the combination of the applied and the induced field. The applied field can come from an external source or it can be self-generated by means of an applied current. For the general case of externally applied field and a

transport current I, the total field outside a straight cable is

$$\bar{H}^{tot} = \bar{H}^{A} + \frac{I}{2\pi r}\hat{\phi} - \nabla\Psi \tag{2.30}$$

where $I = I^{A} + I^{ind}$. If one is looking at the cross-section of just one turn in a multi-turn coil, that particular turn will experience fields from two different sources. The applied field term is actually a combination of an external field coming from some other source (perhaps another magnet) *and* by the magnet's own current but from other turns in the same coil.

The scalar magnetic potential Ψ, which corresponds to any induced multipole fields, satisfies Laplace's equation in free space. In our ordering system,

$$\nabla^2\Psi \approx \nabla_T^2\Psi = 0 \tag{2.31}$$

Therefore, Ψ can be expressed as a summation of harmonics in ϕ only.

$$\Psi = \sum_{n=1}^{\infty} r^{-n} \left\{ \begin{array}{c} a_n \\ b_n \end{array} \right\} \left\{ \begin{array}{c} \sin n\phi \\ \cos n\phi \end{array} \right\} \tag{2.32}$$

The magnetic field at the cable surface $r = R$ is then

$$\begin{aligned} H_r^{ind} &= -\frac{\partial}{\partial r}\Psi \\ &= \sum_{n=1}^{\infty} nR^{-n-1} \left\{ \begin{array}{c} a_n \\ b_n \end{array} \right\} \left\{ \begin{array}{c} \sin n\phi \\ \cos n\phi \end{array} \right\} \qquad (2.33) \\ H_\phi^{ind} &= \frac{I^{ind}}{2\pi R} - \frac{1}{R}\frac{\partial}{\partial\phi}\Psi \\ &= \frac{I^{ind}}{2\pi R} + \sum_{n=1}^{\infty} nR^{-n-1} \left\{ \begin{array}{c} b_n \\ -a_n \end{array} \right\} \left\{ \begin{array}{c} \sin n\phi \\ \cos n\phi \end{array} \right\} \qquad (2.34) \end{aligned}$$

If we assume that the dimensions of the cable are smaller than the gradient length of any external field it experiences, then the task of matching boundary conditions is much simplified. Otherwise, one would have to calculate the exact field at the perimeter of the cable due to outside sources and from neighboring turns and Fourier decompose them in ϕ. However, let us assume that these magnets are usually fairly large compared to just one cable dimension. Therefore, it is a good approximation to assume that the applied field across the cable is uniform and predominantly transverse to the winding.

For a transverse field in the $+\hat{y}$ direction of magnitude H^A, we have

$$\begin{aligned} \bar{H}^A &= H^A \hat{y} \\ &= H^A \sin\phi\, \hat{r} + H^A \cos\phi\, \hat{\phi} \end{aligned} \tag{2.35}$$

The total field can be rewritten as

$$\bar{H} = (H^A \sin\phi - \frac{\partial}{\partial r}\Psi)\, \hat{r} + (H^A \cos\phi - \frac{1}{r}\frac{\partial}{\partial \phi}\Psi + \frac{I}{2\pi R})\hat{\phi} \tag{2.36}$$

Next consider each separate harmonic in ϕ. This will allow us to determine the boundary conditions in terms of the Fourier harmonics. For the total field, we find, at $r = R$

zeroth harmonic:

$$H_r^{(0)} = 0 \tag{2.37}$$

$$H_\phi^{(0)} = \frac{I}{2\pi R} \tag{2.38}$$

nth harmonic $\left\{ \begin{array}{c} \sin n\phi \\ \cos n\phi \end{array} \right\}$:

$$H_r^{(n)} = \left\{ \begin{array}{c} H^A \delta_{n-1} + a_n \\ b_n \end{array} \right\} R^{-n-1} \tag{2.39}$$

$$H_\phi^{(n)} = \left\{ \begin{array}{c} b_n \\ H^A \delta_{n-1} - a_n \end{array} \right\} R^{-n-1} \tag{2.40}$$

where δ_n is the Kronecker delta. These expressions contain the as yet unknown diamagnetic responses a_n and b_n. If we combine some of these expressions, we can eliminate the unknown coefficients a_n and b_n as follows.

$$H_{r,sin}^{(n)} \sin n\phi + H_{\phi,cos}^{(n)} \cos n\phi = 2H^A \delta_{n-1} + \frac{I}{2\pi R}\delta_n \tag{2.41}$$

$$H_{r,cos}^{(n)} \cos n\phi - H_{\phi,sin}^{(n)} \sin n\phi = 0 \tag{2.42}$$

To express these boundary conditions in terms of $E_{||}$ and Φ, we start by introducing a Fourier series similar to that of the scalar magnetic potential.

$$\begin{aligned} E_{||} &= \sum_n \left\{ \begin{array}{c} E_{ns}(r,z) \\ E_{nc}(r,z) \end{array} \right\} \left\{ \begin{array}{c} \sin n\phi \\ \cos n\phi \end{array} \right\} \\ \Phi &= \sum_n \left\{ \begin{array}{c} \Phi_{ns}(r,z) \\ \Phi_{nc}(r,z) \end{array} \right\} \left\{ \begin{array}{c} \sin n\phi \\ \cos n\phi \end{array} \right\} \end{aligned} \tag{2.43}$$

From Faraday's Law,

$$\frac{1}{r}\frac{\partial}{\partial \phi} E_z - \frac{\partial}{\partial z} E_\phi = -\dot{B}_r \tag{2.44}$$

$$\frac{\partial}{\partial z} E_r - \frac{\partial}{\partial r} E_z = -\dot{B}_\phi \tag{2.45}$$

At the perimeter of the cable, all current must flow tangential to the surface so $\dot{\rho} = 0$ and $J_r \propto E_r = 0$. $E_z|_R$ is then simply equal to $E_{||} - \rho\dot{\psi}E_\phi = E_{||} + \frac{\rho\dot{\psi}}{R}\frac{\partial}{\partial\phi}\Phi$. At $r = R$,

$$\frac{1}{R}\frac{\partial}{\partial\phi}(E_{||} + \frac{\rho\dot{\psi}}{R}\frac{\partial}{\partial\phi}\Phi + \frac{\partial}{\partial z}\Phi) = -\dot{B}_r(r = R) \tag{2.46}$$

$$\frac{\partial}{\partial r}(E_{||} + \frac{\rho\dot{\psi}}{r}\frac{\partial}{\partial\phi}\Phi) = \dot{B}_\phi(r = R) \tag{2.47}$$

In an actual cable, the geometry is axisymmetric so $\rho\dot{\psi}$ has no ϕ dependence. Substituting (2.43) into the above two equations and applying (2.41) yields

$$-(\frac{\partial}{\partial r}\bigg|_R + \frac{n}{R})E_{ns} + \frac{n}{R}\left[\frac{\partial}{\partial r}\bigg|_R \rho\dot{\psi} + (n-1)\frac{\rho\dot{\psi}}{R}\right]\Phi_{nc} - \frac{n}{R}\frac{\partial}{\partial z}\Phi_{ns} = 0 \tag{2.48}$$

$$(\frac{\partial}{\partial r}\bigg|_R + \frac{n}{R})E_{nc} + \frac{n}{R}\left[\frac{\partial}{\partial r}\bigg|_R \rho\dot{\psi} + (n-1)\frac{\rho\dot{\psi}}{R}\right]\Phi_{ns} + \frac{n}{R}\frac{\partial}{\partial z}\Phi_{nc} = \frac{\mu_0}{2\pi R}\dot{I}\delta_n + 2\dot{B}^A\delta_{n-1} \tag{2.49}$$

The second boundary condition comes from restricting any currents from flowing in or out of the boundary. Since $E_r = 0$ at $r = R$,

$$-\frac{\partial}{\partial r}\Phi = 0 \tag{2.50}$$

Eqn. 2.49 and 2.50 are the desired general radial boundary conditions.

End Conditions

The fashion which cable ends are terminated must be modeled in order to satisfy the required number of boundary conditions. The most straightforward method is to assume no ends, i.e. the cables are so long that it can be assumed to be infinite. However, in an actual cable, the ends are terminated with low-resistance "joints"

which electrically and mechanically connect cable sections together or to a power supply. Often times with experimental samples, the ends of a cable are open.

Figure 2-3 shows a cross-sectional view of a joint design for the ITER magnet which connects the ends of a cable to the power supply. The end of a cable is stripped of it's outer metal jacket and the strands within are straightened out, and soldered together. It is then wrapped with a metal sheath and soldered to the current bus line. This configuration, where the contact between the current bus and the end of the cable is long, ensures that the current distribution flowing to the cable is more or less uniform. We can model this joint interface in three parts. Figure 2-4 shows the three regions. The leftmost region (2) models the metal-to-metal contact between the bus and the joint. Region 1 is the joint itself where we will assume that the diffusion time of the currents are negligible thus capturing the uniform current behavior of a real joint.

The governing equation is

$$\nabla \times \nabla \times \bar{E} = -\mu_0 \frac{\partial}{\partial t} \bar{J} \tag{2.51}$$

In the joint region (1), the conductivities are anisotropic. The same set of equations that are used to solve the cable region are also needed for the joint region. The difference is that $\sigma_\perp$ here is homogenous since the solder that fills the void between strands makes a uniform conductivity close to the conductivity of copper. Therefore, $\sigma_\perp = \sigma_{cu}$.

In region 2, the conductivity is simply that of copper - homogeneous and isotropic. The differential equation is

$$\nabla^2 \bar{E} = \mu_0 \sigma_\perp \frac{\partial}{\partial t} \bar{E} \tag{2.52}$$

Since current is only in the longitudinal direction at the entrance to the structure,

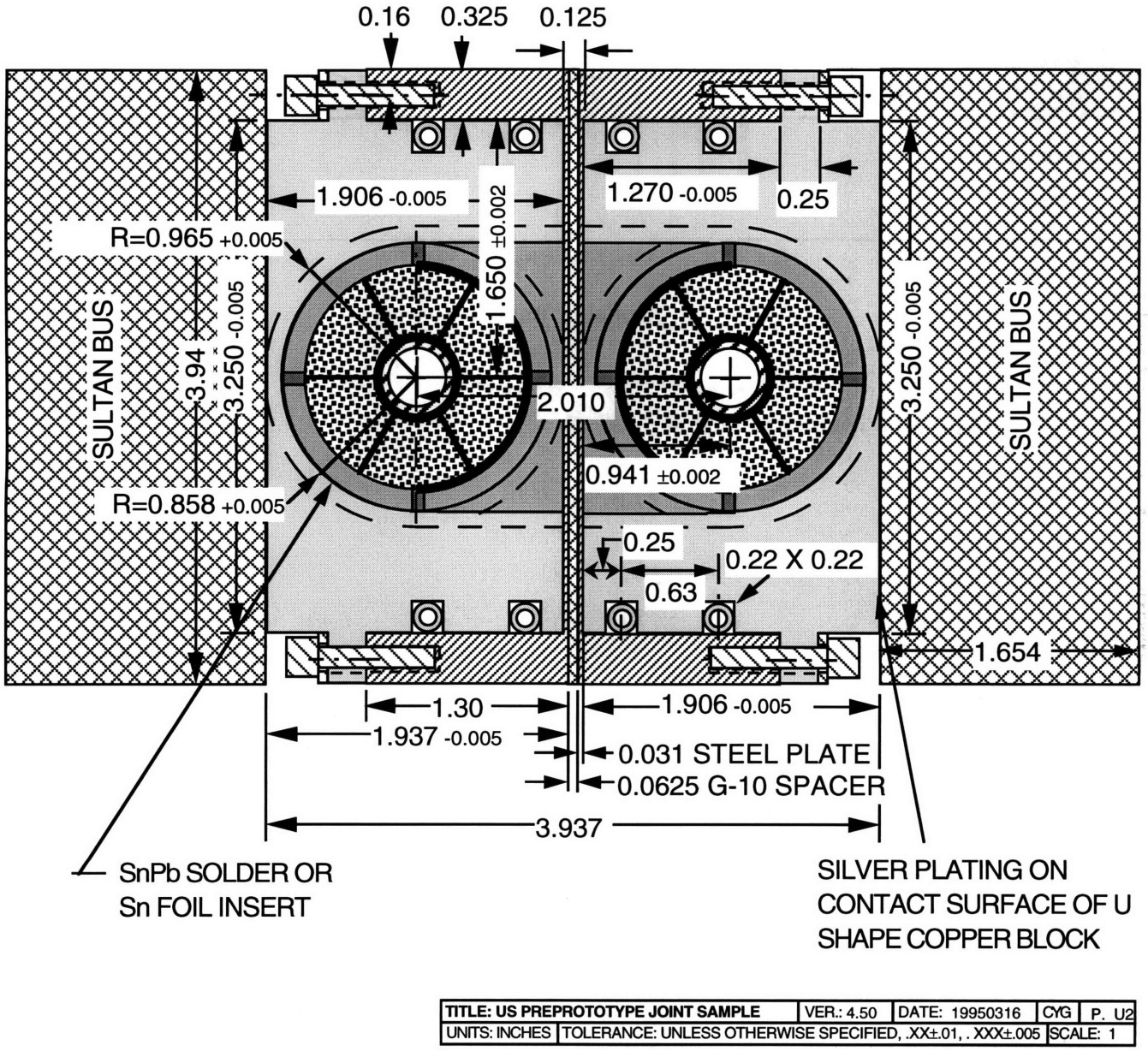

Figure 2-3: Schematic of joint design for ITER coil.

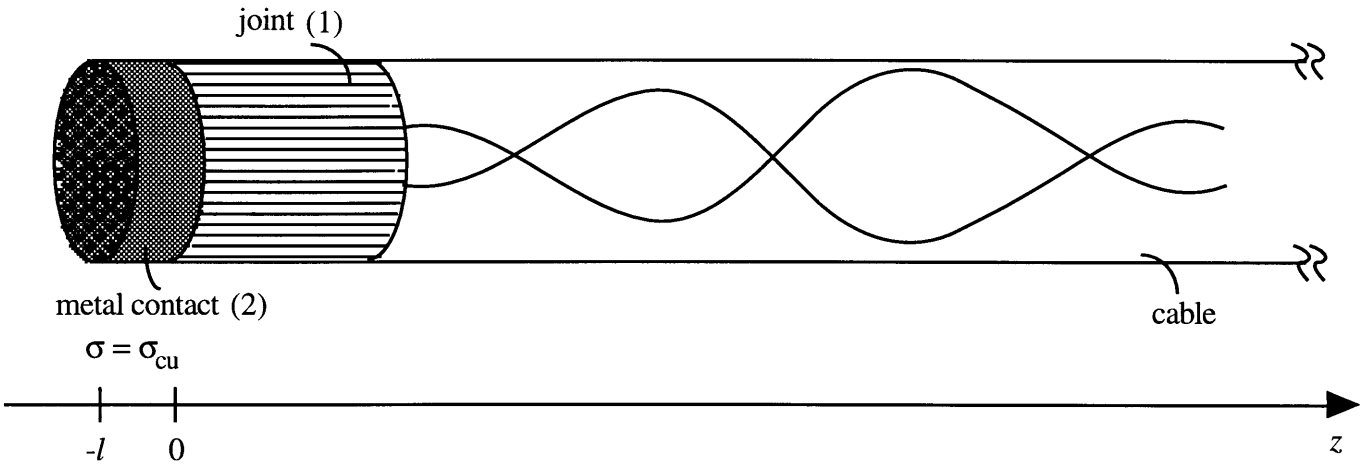

Figure 2-4: Model of joint at source.

the boundary conditions are at $z = -l$,

$$\begin{aligned} E_z^{(2)} &= \frac{I}{\sigma_{cu}\pi R^2} \\ E_r^{(2)} &= 0 \\ E_\phi^{(2)} &= 0 \end{aligned} \tag{2.53}$$

at $z = 0$,

$$\begin{aligned} E_r^{(1)} &= E_r^{(2)} \\ E_\phi^{(1)} &= E_\phi^{(2)} \\ \sigma_{||} E_z^{(1)} &= \sigma_{cu} E_z^{(2)} \end{aligned} \tag{2.54}$$

at $r = R$,

$$E_r^{(1)} = E_r^{(2)} = 0 \tag{2.55}$$

The superscripts (1) and (2) indicate the regions.

Region (2)

If we were to assume small enough changes in $\bar{B}$ such that $\nabla \times E = -\frac{\partial}{\partial t}\bar{B} \approx 0$ coupled with a divergence-free current density which yields $\nabla \cdot J = \nabla \cdot E = 0$, these two conditions imply that the scalar potential can be used.

$$\bar{E} = -\nabla\Phi \tag{2.56}$$

Φ in turn would satisfy Laplace's equation.

$$\nabla^2\Phi = 0 \tag{2.57}$$

To be consistent with the boundary conditions at $r = R$ and $z = -l$, the general solution for Φ should be

$$\Phi^{(2)}(r,\phi,z) = -\frac{I}{\sigma_{cu}\pi R^2}z + \sum_n\sum_m \Phi_{mn}J_m(k_n r)\left\{\begin{array}{c}\sin m\phi\\ \cos m\phi\end{array}\right\}\cosh k_n(z+l) \tag{2.58}$$

Therefore

$$\begin{aligned} E_r &= -\frac{\partial}{\partial r}\Phi \\ &= \sum_n\sum_m\left[\frac{m}{r}J_m(k_n r) - k_n J_{m-1}(k_n r)\right]\left\{\begin{array}{c}\sin m\phi\\ \cos m\phi\end{array}\right\}\cosh k_n z \qquad (2.59)\\ E_\phi &= -\frac{1}{r}\frac{\partial}{\partial\phi}\Phi = \sum_n\sum_m\frac{m}{r}J_m(k_n r)\left\{\begin{array}{c}\sin m\phi\\ -\cos m\phi\end{array}\right\}\cosh k_n z \qquad (2.60)\\ E_z &= -\frac{\partial}{\partial z}\Phi = \frac{I}{\sigma_{cu}\pi R^2} + \sum_n\sum_m k_n J_m(k_n r)\left\{\begin{array}{c}\sin m\phi\\ \cos m\phi\end{array}\right\}\sinh k_n z \qquad (2.61)\end{aligned}$$

k_n has to satisfy the condition that

$$mJ_m(k_nR) - k_nrJ_{m-1}(k_nR) = 0 \tag{2.62}$$

Region (1)

The last equation of (2.54) dictates the continuity of current. The summation term in $E_z^{(2)}$ is scaled by both $\sigma_{cu}/\sigma_{||}$ and $\sinh k_n l$. Therefore, neglecting the $\frac{\sigma_{cu}}{\sigma_{||}}$ terms and assuming $l << 1/k_n$, we obtain

$$\begin{aligned} E_z^{(1)} &= \frac{\sigma_{cu}}{\sigma_{||}} E_z^{(2)} \\ &\approx \frac{I}{\sigma_{||}\pi R^2} \end{aligned} \tag{2.63}$$

We have arrived at a simple and straightforward boundary condition at $z = 0$. The joint will just be an extension of the cable with a different perpendicular conductivity and can be solved numerically. The boundary condition at the end of the joint, at the joint-metal contact interface, will be that of a uniform field distribution, it's magnitude determined by the current source. The fields and thereby the loss in the metal contact region can be found by equating the transverse fields at the boundary $z = 0$ to find the coefficients $E_{zmn}^{(2)}$ and $E_{rmn}^{(2)}$.

As mentioned before, the above derivation is only for one joint design. The condition on dipole fields and therefore currents at $z = 0$ is identical to that of an open-ended cable. There is a range of conditions on the ends, each dictated by the type of joint design.

For the US-DPS coil, ribbon joints were built. These are manufactured by taking strands at the end of the cable, straightening them out and flattening the cable geometry from a circular to a flat rectangular cross-section. The strands are then

soldered together and placed in a metal sheath. Because the strands were soldered together such that there is no void space, the transverse contact resistivity approaches that of the solder metal resistivity and is much higher than the rest of the cable. However, $\sigma_\perp$ is still much smaller than $\sigma_{||}$. This becomes a true multi-regional and anisotropic problem.

It has been proposed, but not implemented, that the strands are stripped of their normal metal and compacted together. This would represent the opposite extreme to the ITER joint. Now, $\sigma_\perp = \sigma_{||}$ and the boundary condition at $z = 0$ becomes $E_r = 0$ or $\Phi = 0$. This is equivalent to the short-circuited end condition.

2.5.2 Magnet in persistent mode

In applications where magnets are not connected to any external source, the magnet is said to be operating in *persistent* mode. It is one of the great advantages of having superconducting cables - the decay time is so large that any flux or current trapped in the magnet will stay trapped for a long time. This mode of operation can be found in NMR machines and can be used for such applications as MAGLEV where the cost of having an onboard power supply for each electromagnetic magnet is impractical.

Boundary Conditions

The major difference between this problem and that of a magnet with a current source is that here, the transport current is no longer a source term. In fact, the current is an unknown variable, a combination of an applied and an induced current. Unlike the previous case where any induced back EMF is absorbed by the power supply (i.e. any induced voltage appears across the source), the induced current produced by the

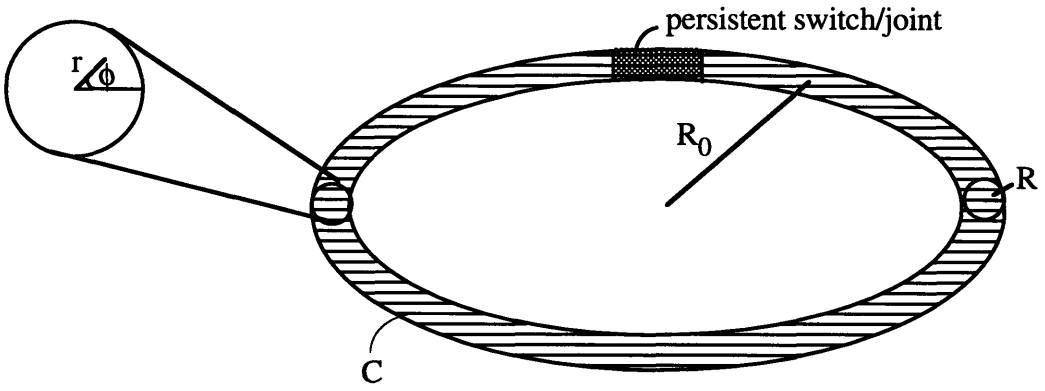

Figure 2-5: Sketch of magnet in an electrically closed loop.

EMF can determine a significant portion of the total transport current. Thus,

$$I = I^A + I^{ind} \tag{2.64}$$

Consider one single loop of radius R_0 as shown in figure 2-5. The specifications for boundary conditions are a bit tricky due to the implicit curvature of the problem. *However, one can show that if all terms of order R/R_0 or higher are neglected, the formulation for a straight wire case can be used here.* This is saying that the size of the magnet is so large compared to the radius of the cable, the curvature effect can be neglected.

Faraday's law dictates that for a time-varying magnetic field, the electric field along the cable must satisfy

$$\oint_c \bar{E} \cdot d\bar{l} = -\frac{\partial}{\partial t}\lambda \tag{2.65}$$

where λ is the total flux linked.

The flux linkage term consists of an external field, field due to current in the

cable, and any multipole fields. Since multipole fields die away as r^n and since the magnitude of these fields are already small, the contribution to the flux linkage due to these induced terms will be neglected.

The externally applied magnetic field is uniform. The induced field is a function of the transport current.

$$\int_{-\pi R_0}^{\pi R_0} E_z dz = -\dot{B}^A \pi R_0^2 - \frac{\partial}{\partial t} \oiint B^{ind}(I, r, \phi, z) d\bar{a} \tag{2.66}$$

This can be rewritten as

$$\int_{-\pi R_0}^{\pi R_0} (E_z + \frac{\partial}{\partial t} A_z) dz = -\dot{B}^A \pi R_0^2 \tag{2.67}$$

where A_z corresponds to the vector potential of the loop current at the boundary. This saves us some time in calculating the field due to a loop of current and then having to integrate it over the internal area of the loop. The complete expression for $A_z(r, \phi)$ can be found in Jackson's book[12]. However since we are ignoring the effect of the curvature of the loop, A_z is dependent only on I. At the cable boundary $r = R$,

$$A_z = \frac{\mu_0 I}{2\pi} C \tag{2.68}$$

where C is a constant calculated from the average value of A_z around the cable perimeter and is dependent on the size of the cable. As an example, for $R = 1.9$cm and $R_0 = 19$cm, $C \approx 4.9$.

Therefore, we have an additional boundary condition that links the current to the applied magnetic field.

$$\oint_l (E_z(r{=}R) + \frac{\mu_0 \dot{I}}{2\pi} C)\, dz = -\dot{B}^A \frac{R_0}{2} \tag{2.69}$$

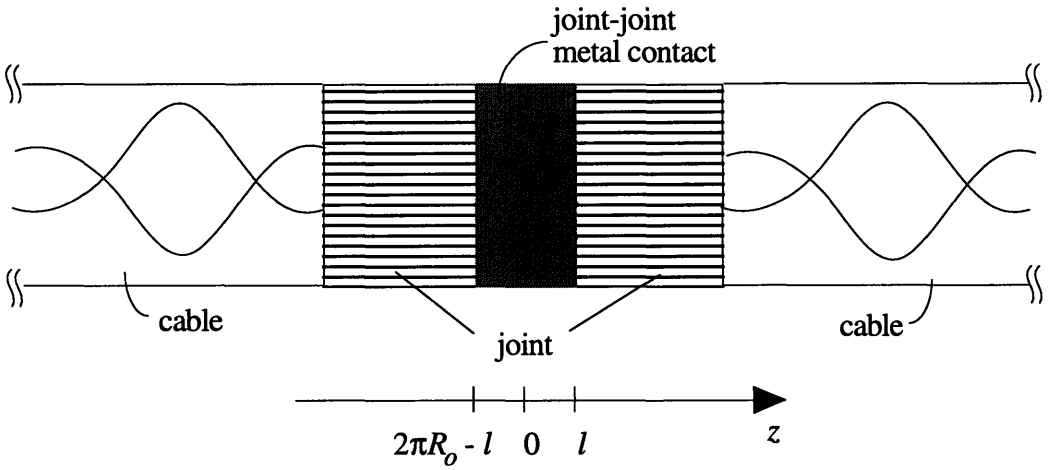

Figure 2-6: Model of persistent switch (joint that closes the loop).

End conditions

Since the ends are wrapped on itself, the term "end" conditions is a bit misleading but we will use this terminology since the specifications are fairly similar to that of a magnet connected to a source. More commonly, this joint interface is referred to as a "persistent switch".

Figure 2-6 shows the model of the joint between the two ends of the coil. Again, we assume that the current is uniform in the metal contact region. Here is the boundary condition at $z = l$ and $2\pi R_0 - l$.

$$E_z = \frac{I}{\sigma_{||}\pi R^2} \tag{2.70}$$

This also means that there is a resistive voltage drop across the metal region. Since

we know that the current is uniform, the voltage is simply

$$V_{res} = \frac{2l}{\sigma_{cu}\pi R^2} I \tag{2.71}$$

The boundary condition is now refined to

$$\int_l^{2\pi R_0 - l} (E_z + \frac{\mu_0 \dot{I}}{2\pi} C) dz - \frac{2l}{\sigma_{cu}\pi R^2} I = -\dot{B}^A \frac{R_0}{2} \tag{2.72}$$

2.6 Conclusion

An elegant yet powerful electromagnetic model has been developed for the study of current distribution and AC loss in composite superconductors. An ordering system, which captures most of the physics of the problem, has been instrumental in reducing the governing equations to a tractable form. Two equations for two unknowns, $E_{||}$ (the electric field along the direction of a superconducting filament or strand) and Φ(the transverse potential), describe the entire system.

To complete the formulation of the model, a general set of boundary conditions were derived for circulary shaped cables with joints at both ends. These cable ends can be connected to a source or with each other in "persistent mode".

Chapter 3

Analytic Results of Limiting Cases

The objective of this chapter is to derive several analytic solutions from the governing equations in special limits. It is always desirable to be able to rely on closed-form solutions for any problem if they are available. Numerics are useful when analytic results cannot be obtained. Some simple geometries have analytic solutions thereby allowing certain physical laws describing the behavior of these strands and cables to be ascertained.

This chapter outlines the derivations to the solutions of untwisted or single twist pitch composite conductors with various end conditions. The conductivity $\sigma_{||}$ will be treated as a constant. Results of interesting limits to these solutions will be analyzed and, when possible, compared to existing literature.

3.1 Open-circuited straight cable

The first limiting case is that of a straight, finite section of cable of length $2L$ which is open-circuited at both ends. The wires inside are untwisted and no saturation occurs.

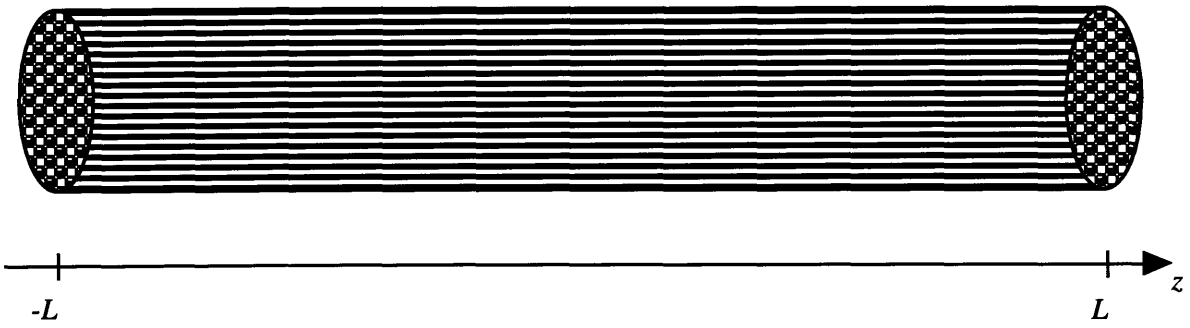

Figure 3-1: Untwisted finite length cable.

Since there is no twisting, $\dot{\rho} = 0$ and $\rho\dot{\psi} = 0$ so that $\hat{e}_{||} = \hat{e}_z$. The differential equations are reduced to simply

$$\nabla_T^2(E_{||} + \frac{\partial}{\partial z}\Phi) = \mu_0 \frac{\partial}{\partial t}\sigma_{||}E_{||} \tag{3.1}$$

$$\sigma_\perp \nabla_T^2 \Phi = \sigma_{||}\frac{\partial}{\partial z}E_{||} \tag{3.2}$$

Taking $\frac{\partial}{\partial z}$ of (3.2) and substituting into (3.1) yields one equation for $E_{||}$. For simplicity, we assume $\frac{\partial}{\partial t} = 0$, i.e. we are solving for stationary solutions.

$$\left(\nabla_T^2 + \frac{\sigma_{||}}{\sigma_\perp}\frac{\partial^2}{\partial z^2}\right) E_{||} = \mu_0 \frac{\partial}{\partial t}\sigma_{||}E_{||} \approx 0 \tag{3.3}$$

These solutions can be applied with a decent amount of accuracy for slow field variations. For sinusoidal field variations, the time derivative does not complicate the analysis. For this example, we will examine a ramped field to illustrate how the losses scale. In addition, no saturation of the wires and uniform conductivities are also assumed.

The boundary conditions are

The boundary conditions are

1. At the ends ($z = \pm L$), $J_z \approx J_{||} = 0$ or since $E_{||} = J_{||}/\sigma_{||}$

$$E_{||}\Big| = 0$$

2. Since there is no path for any net transport current to loop back on itself, $I = 0$ everywhere.

3. The boundary conditions on the perimeter $r = R$ are taken directly from (2.49) and (2.50). Since we are solving for the stationary solution (induced fields due to shielding currents neglected), and t the problem is symmetric around $\phi = \frac{\pi}{2}$, we can throw away all $\sin\phi$ terms.

$$\frac{\partial}{\partial r}\Big|_R E_{nc}(r,z) + \frac{n}{R}\left[E_{nc}(R,z) + \frac{\partial}{\partial z}\Phi_{nc}(R,z)\right] = 2\dot{B}^A\delta_{n-1}$$

4. At $r = R$,

$$\frac{\partial}{\partial r}\Phi = 0$$

Boundary condition #1 dictates that the longitudinal fields have to go to zero at the ends. This forces automatic z-dependence on the field. Also, the dc component (zero ϕ harmonic) which is needed to satisfy the other boundary conditions, will have to come from averaging over the harmonics in z. In other words, there is no purely z-independent term. The appropriate waveforms that go to zero at the ends and have a dc component are odd harmonics of $\cos k_p z$ where $k_p = (p + \frac{1}{2})\frac{\pi}{L}$. Since the magnetic field has only one ϕ harmonic and we have already assumed that the time-derivative of Maxwell's equation is zero, we can safely assume that there is only one ϕ harmonic for the electric field or $E_{nc} = E_{1c}$. Therefore, the longitudinal electric

field is expressed as

$$\begin{aligned} E_{||}(r,\phi,z) &= E_{1c}(r,z)\cos\phi \\ &= \sum_{p=0}^{\infty} E_{1p}(r)\cos\phi\cos k_p z \end{aligned} \tag{3.4}$$

Substituting into (3.3) yields for each harmonic in z,

$$\left[\nabla_T^2 E_{1p}(r) - \frac{\sigma_{||}}{\sigma_\perp}k_p^2 E_{1p}(r)\right]\cos\phi\cos k_p z = 0 \tag{3.5}$$

The solution for this differential equation is in the form of modified Bessel functions. Since fields are regular at the origin, we pick modified Bessel functions of the first kind.

$$E_{1p}(r) = E_{1p} I_1(k_{rp} r) \tag{3.6}$$

where $k_{rp} = \sqrt{\frac{\sigma_{||}}{\sigma_\perp}}k_p$.

From (3.1), the differential equation relating $E_{||}$ and Φ without the time derivative is

$$-\frac{\partial}{\partial z}\nabla_T^2\Phi = \nabla_T^2 E_{||} \tag{3.7}$$

This gives two possible relationships - a homogeneous and particular one.

$$\nabla_T^2\Phi = 0 \tag{3.8}$$

$$-\frac{\partial}{\partial z}\Phi = E_{||} \tag{3.9}$$

The solution that satisfies both equataions is in the form

$$\Phi = \sum_{p=0}^{\infty}[b_{1p} r - \frac{1}{k_p}E_{1p} I_1(k_{rp} r)]\cos\phi\sin k_p z \tag{3.10}$$

where b_{1p} and E_{1p} are constants to be determined.

Now we are ready to substitute the equations for $E_{||}$ and Φ into the remaining boundary conditions to solve for the unknown coefficients E_{1p} and b_1. From b.c. #3,

$$\sum_p [E_{1p}\beta_{1p} + k_p b_{1p}] \cos k_p z = 2\dot{B}^A \tag{3.11}$$

where $\beta_{1p} = \frac{\partial}{\partial r}\Big|_R I_1(k_{rp}r)$.

Integrating both sides by $\frac{1}{2L}\int_{-L}^{L} \cos k_q z \, dz$, we get when $q = p$

$$\beta_{1p}E_{1p} + k_p b_{1p} = \begin{cases} \frac{4}{k_p L}\dot{B}^A & \text{even } p \\ -\frac{4}{k_p L}\dot{B}^A & \text{odd } p \end{cases} \tag{3.12}$$

or

$$E_{1p} = \frac{\pm 4\dot{B}^A - k_p^2 L b_{1p}}{k_p L \beta_{1p}} \tag{3.13}$$

From b.c.#4, we have another relationship between E_{1p} and b_{1p},

$$E_{1p} = \frac{k_p b_{1p}}{\beta_{1p}} \tag{3.14}$$

which yields

$$E_{1p} = \pm\frac{2\dot{B}^A}{k_p L \beta_{1p}} \tag{3.15}$$

$$b_{1p} = \pm\frac{2\dot{B}^A}{k_p^2 L} \tag{3.16}$$

Therefore, the solutions for the fields are

$$Ep = 2\dot{B}^A \sum_p (-1)^p \frac{I_1(k_{rp}r)}{k_p L \beta_p} \cos\phi \cos k_p z \tag{3.17}$$

$$E_r = -2\dot{B}^A \sum_p (-1)^p \frac{1}{k_p^2 L}[1 - \frac{k_{rp}}{\beta_p} I_0(k_{rp}r) + \frac{1}{\beta_p r} I_1(k_{rp}r)] \cos\phi \sin k_p z \quad (3.18)$$

$$E_\phi = 2\dot{B}^A \sum_p (-1)^p \frac{1}{k_p^2 L}[1 - \frac{1}{\beta_p r} I_1(k_{rp}r)] \sin\phi \sin k_p z \quad (3.19)$$

where $\beta_p = \beta_{1p} = k_{rp} I_0(k_{rp}R) - \frac{1}{R} I_1(k_{rp}R)$.

To find the power dissipated, we need to integrate σE^2 over the volume of the cable.

$$P = P_{||} + P_\perp \quad (3.20)$$

$$= \int_{-L}^{L} \int_0^{2\pi} \int_0^R (\sigma_{||} E_{||}^2 + \sigma_\perp E_r^2 + \sigma_\perp E_\phi^2) r \, dr \, d\phi \, dz \quad (3.21)$$

After some messy algebra, we have the solution for power dissipated as a summation over the z harmonics.

$$P_{||} = (2L)(\pi R^2)\sigma_{||}(\dot{B}^A)^2 \sum_{p=0}^{\infty} \frac{I_1^2(k_{rp}R) - I_0(k_{rp}R) I_2(k_{rp}R)}{(\beta_p k_p L)^2} \quad (3.22)$$

$$P_\perp = (2L)(\pi R^2)\sigma_\perp(\dot{B}^A)^2 \sum_{p=o}^{\infty} \left\{ 2 - \frac{4}{\beta_p R} I_1(k_{rp}R) \right.$$
$$\left. - \frac{1}{(\beta_p R)^2} \left[2I_1^2(k_{rp}R) + (k_{rp}R)^2 [I_1^2(k_{rp}R) - I_0^2(k_{rp}R)] \right] \right\} / k_p^4 L^2 \quad (3.23)$$

If the cable is really long, i.e. when $\sqrt{\frac{\sigma_{||}}{\sigma_\perp}} R/L << 1$, then

$$\beta_p \to \frac{k_{rp}}{2}$$

$$P_{||} \to (\frac{1}{2\pi^2})\sigma_{||}(2L)(\pi R^2)(\dot{B}^A R)^2 \sum_{p=0}^{\infty} \frac{1}{(p + \frac{1}{2})^2}$$

$$\to \frac{\sigma_{||} L R^2}{2} (\pi R^2 \dot{B}^{A2}) \quad (3.24)$$

$$P_\perp \to 0 \quad (3.25)$$

This is the case of the infinite cable.

We see that the power dissipated in the longitudinal direction goes as R^4L and that cross-current dissipation becomes negligible with a long cable.

In the other extreme, if the conductor is very good, i.e. if $\sqrt{\frac{\sigma_{||}}{\sigma_\perp}}R/L >> 1$,

$$\begin{aligned} \beta_p &\rightarrow k_{rp}I_n(\text{large argument}) \qquad (3.26) \\ P_{||} &\rightarrow 0 \\ P_\perp &\rightarrow (\frac{2L^2}{\pi^4})\sigma_\perp(2L)(\pi R^2)(\dot{B}^A)^2 \sum_{p=0}^{\infty} \frac{1}{(p+\frac{1}{2})^4} \\ &\rightarrow 12\sigma_\perp L^3(\pi R^2 \dot{B}^{A2}) \qquad (3.27) \end{aligned}$$

In this case, most of the power is dissipated in circulating cross-currents. Since P scales as R^2L^3 in this case, it seems like the better the conductor is, the more sensitive the loss is to the length of the cable. This illustrates clearly how the power dissipated can become very large with long superconducting cables and the motivation for twisting the wires in such cables becomes evident. The advantage of twisting will become apparent in the next section.

3.2 Short-circuited current loop

3.2.1 Untwisted wires

Let's solve a simple case. Assume the wires inside are straight and the ends short-circuited to each other; in other words, the joint that connects them is perfect. For untwisted wires, $E_z = E_{||}$ and since the problem is z-independent ($\hat{e}_{||} \cdot \nabla = \frac{\partial}{\partial z} = 0$):

$$\oint_C E_{||} dz = 2\pi R_0 E_{||} \qquad (3.28)$$

Eqn. 2.69 reduces to

$$E_{||}(r=R) = -\dot{B}^A R_0/2 - \frac{\mu_0 \dot{I}}{2\pi} C \tag{3.29}$$

We again need to solve the following equation

$$\nabla_T^2 E_{||} = \mu_0 \frac{\partial}{\partial t} \sigma_{||} E_{||} \tag{3.30}$$

In this case, the time derivative cannot be neglected because the "steady-state" solution *is* time-dependent. This differential equation can be solved analytically by using Laplace transforms.

$$\nabla_T^2 \hat{E}(s) = \mu_0 \sigma_{||} s[\hat{E}(s,r) - E_{||}(t=0)] \tag{3.31}$$

Assuming $E_{||} = 0$ at $t = 0$, we have a second order differential equation for $\hat{E}(s,r)$.

$$\nabla_T^2 \hat{E}(s) - \mu_0 \sigma_{||} s \hat{E}(s,r) = 0 \tag{3.32}$$

for which the corresponding solution is

$$\hat{E} = A I_0(kr) \tag{3.33}$$

where A is a coefficient yet to be determined, $k = \sqrt{\mu_0 s \sigma_{||}}$, and $I_0(kr)$ is the zeroth order modified Bessel function of the first kind.

Substituting the above solution for $\hat{E}$ into eqn. 3.29 yields for the field at $r = R$,

$$\begin{aligned} \hat{E}(r=R) &= A I_0(kR) \\ &= -\mathcal{L}\{\dot{B}^A\} \frac{R_0}{2} - \frac{\mu_0}{2\pi} C s \hat{I}(s) \end{aligned} \tag{3.34}$$

Eqn. 2.21 yields the other relation between $\hat{E}$ and $\hat{I}$.

$$\left.\frac{\partial}{\partial r}\right|_R \hat{E} = \frac{\mu_0}{2\pi R} s\hat{I} \tag{3.35}$$

Substituting (3.34) into (3.35) gives

$$kAI_1(kR) = \frac{\mu_0}{2\pi R} s\hat{I} \tag{3.36}$$

Combining (3.33), (3.34), and (3.36) yields

$$\hat{E}(r,s) = -\mathcal{L}\{\dot{B}^A\}\frac{R_0}{2}\frac{I_0(kr)}{I_0(kR) + kRCI_1kR} \tag{3.37}$$

As an example, take a sinusoidal field with a vanishing time derivative at $t = 0$.

$$B^A = B_0(1 - \cos\omega t) \tag{3.38}$$

The Laplace transform is

$$\mathcal{L}\{\dot{B}^A\} = B_0\frac{\omega^2}{s^2 + \omega^2} \tag{3.39}$$

and

$$\hat{E} = \frac{-\omega^2 B_0 R_0}{2(s^2 + \omega^2)}\frac{I_0(kr)}{I_0(kR) + kRCI_1(kR)} \tag{3.40}$$

The expression for $\hat{E}$ must be inverse transformed to obtain the solution in the time domain.

$$E_{||}(r,t) = \mathcal{L}^{-1}\{\hat{E}(r,s)\} = \int_{-i\infty}^{i\infty} \hat{E}(r,s)e^{st}ds \tag{3.41}$$

We can apply the Residue Theorem and integrate from $i\infty$ to $-i\infty$ with a contour that encloses the left hand s-plane. The poles are at $s_1 = i\omega$, $s_2 = -i\omega$ and where s

satisfies the transcendental equation

$$I_0(kR) + kRCI_1(kR) = 0 \tag{3.42}$$

There are an infinite number of roots but only a few that dominate the solution. However upon numerically solving this equation, it becomes clear that there exists one dominant s value, corresponding to the smallest root. Physically, this would correlate to the characteristic time constant of the system. s_1 and s_2 are the driving terms. From this relation, one can find the time constant(s) of the system given the conductivity and the geometry.

Recognizing the fact that $k_2 = \sqrt{\mu_0 s_2 \sigma_{||}} = k_1^*$ and that $I_n(k^* r) = I_n^*(kr)$, the total electric field is

$$\begin{aligned} E_{||}(r,t) = \quad & -\frac{\omega B_0 R_0}{2} \Im \left[\frac{I_0(k_1 r)}{I_0(k_1 R) + k_1 RCI_1(k_1 R)} e^{i\omega t} \right] \\ & - B_0 R_0 \omega^2 \sum_q \frac{s_q I_0(k_q r) e^{s_q t}}{(s_q^2 + \omega^2)[k_q R I_1(k_q R) + (k_q R)^2 C I_0(k_q R)]} \end{aligned} \tag{3.43}$$

where s_q are the poles and $k_q = \sqrt{\mu_0 \sigma_{||} s_q}$. The first term has a $\sin \omega t$ dependence and a phase lag. The second term in the above equation is a transient term. For the values of

$$\begin{aligned} B_0 &= 1\text{T} \\ R &= 1.9\text{cm} \\ R_0 &= 19\text{cm} \\ C &= 4.9 \qquad (3.44) \\ \sigma_{||} &= 1 \times 10^{14}\text{mho/m} \\ \omega &= 2\pi/60\text{sec} \qquad (3.45) \end{aligned}$$

the dominant time constant of the system is $\tau = 1.17 \times 10^5$sec. The parallel steady state power dissipation, which corresponds to the loss incurred by an oscillating transport current, is plotted in figure 3-2.

If we take the realistic limit of $|k_1 R|$ and $|k_2 R| >> 1$ and substitute $-\frac{1}{\tau}$ as the leading order s_q value, we can rewrite the complex amplitude of $E_{||}$ (from (3.43)) as

$$\hat{E} \overset{|k_1 R|>>1}{\approx} \frac{-\omega B_0 R_0}{2} \frac{I_0(k_1 r)}{k_1 R C I_1(k_1 R)} + B_0 R_0 (\omega\tau)^2 \frac{I_0(k_q r) e^{-t/\tau}}{\tau[1+(\omega\tau)^2][k_q R I_1(k_q R) + (k_q R)^2 C I_0(k_q R)]} \quad (3.46)$$

The ratio of the second term to the first term in the above equation is approximately $\frac{|k_1|R}{\omega\tau}$ or $\sqrt{\frac{1}{\omega\tau}} k_q R$. $k_q R$ is of order unity but $\omega\tau$ is generally very large due to the large value of τ. Therefore, the second transient term is negligible. This simplifies the task of finding the power loss. The sinusoidal steady-state rms power loss density is simply

$$< p_d >= \frac{1}{2} \Re\{\sigma_{||} \hat{E} \hat{E}^*\} \quad (3.47)$$

Therefore, the power loss is

$$\begin{aligned} < P_d > &= L \int_0^{2\pi} \int_0^R < p_d > r \, dr \, d\phi \\ &= 2\pi\sigma_{||} L \left(\frac{\omega B_0 R_0}{2RC}\right)^2 \frac{1}{|k_1|^2 |I_0(k_1 R)|^2} \int_0^R I_0(k_1 r) I_0(k_1^* r) r \, dr \\ &= 2\pi\sigma_{||} L \left(\frac{f B_0 L}{RC}\right)^2 \frac{1}{|k_1|^2 |I_0(k_1 R)|^2} \left[\frac{\Im\{k_1 r I_0(k_1 r) I_1^*(k_1 r)\}}{\Im\{k_1^2\}}\right]_0^R \\ &\approx 2\pi\sigma_{||} L \left(\frac{f B_0 L}{RC}\right)^2 \left[\frac{1}{\sqrt{2}} \frac{\sqrt{\mu_0 \sigma_{||} \omega}}{(\mu_0 \sigma_{||} \omega)^2}\right] R \\ &= \frac{\sigma_{||} L^3}{C^2} \left(\frac{\delta}{R}\right)^3 (\pi R^2 f^2 B_0^2) \end{aligned} \quad (3.48)$$

where $\delta = \sqrt{\frac{2}{\mu_0 \sigma_{||} \omega}}$ is the skin depth associated with the cable. Additionally, $2L = 2\pi R_0$ and $f = \frac{\omega}{2\pi}$. The next section will show the difference in amplitude between loss due to the induced transport current and loss due to cross-coupling currents.

3.2.2 Twisted wires

We can add a helical twist to the short circuit loop problem. Assume now that the wires are helically twisted with a twist pitch L_p. This is equivalent to a cable with only one stage. To recap, the boundary conditions are

$$E_z^{(0)}(r=R) = -\frac{\dot{B}^A R_0}{2} - \frac{\mu_0 \dot{I}}{2\pi C} \tag{3.49}$$

$$\left.\frac{\partial}{\partial r}\right|_R E_z^{(0)} = \frac{\mu_0 \dot{I}}{2\pi R} \tag{3.50}$$

$$\left.\frac{\partial}{\partial r}\right|_R \Phi^{(0)} = 0 \tag{3.51}$$

$$\left.\frac{\partial}{\partial r}\right|_R E_z^{(1)}(r,t) + \frac{1}{r} E_z^{(1)}(r=R,t) + \frac{2\pi}{L_p}\frac{\partial}{\partial \phi}\Phi^{(1)}(r=R,t) = 2\dot{B}^A \tag{3.52}$$

$$\left.\frac{\partial}{\partial r}\right|_R \Phi^{(1)} = 0 \tag{3.53}$$

where the (0) and (1) superscripts depict the zeroth and first harmonics in ϕ.

The path of each strand has the direction $\hat{z} + \frac{2\pi}{L_p} r\hat{\phi}$. The path components are thus

$$\dot{\rho} = 0 \tag{3.54}$$

$$\rho\dot{\psi} = \frac{2\pi}{L_p} r \tag{3.55}$$

$$E_{||} = E_z - \frac{2\pi}{L_p}\frac{\partial}{\partial \phi}\Phi \tag{3.56}$$

The differential equations reduce to

$$\nabla_T^2(E_{||} + \frac{2\pi}{L_p}\frac{\partial}{\partial\phi}\Phi) = \mu_0\frac{\partial}{\partial t}\sigma_{||}E_{||} \tag{3.57}$$

$$\sigma_\perp\nabla_T^2\Phi = \frac{2\pi}{L_p}\sigma_{||}\frac{\partial}{\partial\phi}E_{||} \tag{3.58}$$

Separating into zeroth and first harmonics in ϕ and assuming that $\mu_0\frac{\partial}{\partial t}\sigma_{||}E_1(r,\phi,t) \approx 0$ yields (we can make this assumption if $\dot{B}^A$ is large compared to any induced terms), zeroth harmonic:

$$\nabla_T^2 E_0(r,t) = \mu_0\frac{\partial}{\partial t}\sigma_{||}E_0(r,t) \tag{3.59}$$

$$\sigma_\perp\nabla_T^2\Phi_0(r,t) = 0 \tag{3.60}$$

first harmonic:

$$\nabla_T^2(E_1(r,\phi,t) + \frac{2\pi}{L_p}\frac{\partial}{\partial\phi}\Phi_1(r,\phi,t)) = 0 \tag{3.61}$$

$$\nabla_T^2\Phi_1(r,\phi,t) = \frac{2\pi}{L_p}\frac{\sigma_{||}}{\sigma_\perp}\frac{\partial}{\partial\phi}E_1(r,\phi,t) \tag{3.62}$$

There is no solution for $\Phi_0(r,t)$ that would give regular field at the origin except for $\Phi_0(r,t) = 0$. Since $\Phi_0 = 0$ and thus $E_0(r,t) = E_z^{(0)}(r,t)$, the differential equations and the boundary conditions for the zeroth harmonic fields are the same as for the untwisted cable. This zero harmonic corresponds to the transport current loss. Now all we have left are the first harmonic fields to solve.

Combining (3.61) and (3.62), we obtain

$$\nabla_T^2 E_1(r,t)\cos\phi + (\frac{2\pi}{L_p})^2\frac{\sigma_{||}}{\sigma_\perp}\frac{\partial^2}{\partial\phi^2}E_1(r,t)\cos\phi = 0 \tag{3.63}$$

The solution to this equation takes the form

$$E_1(r,\phi,t) = AI_1(kr)\cos\phi \tag{3.64}$$

where

$$k = \frac{2\pi}{L_p}\sqrt{\frac{\sigma_{||}}{\sigma_\perp}} \tag{3.65}$$

and A is a coefficient to be evaluated.

Plugging (3.64) back into (3.62) yields for Φ_1,

$$\nabla_T^2\Phi_1(r,\phi,t) = -\frac{\sigma_{||}}{\sigma_\perp}\frac{2\pi}{L_p}AI_1(kr)\sin\phi \tag{3.66}$$

$\Phi_1(r,\phi,t)$ has a homogeneous and a particular solution.

$$\Phi_1(r,\phi,t) = \Phi_{1p}I_1(kr)\sin\phi + \Phi_{1h}r\sin\phi \tag{3.67}$$

Substituting this solution into (3.66), we have

$$\Phi_{1p} = -\frac{L_p}{2\pi}A \tag{3.68}$$

Applying boundary condition (3.52), we obtain

$$A\beta + \frac{2\pi}{L_p}\Phi_{1h} = 2\dot{B}^A \tag{3.69}$$

where

$$\begin{aligned}\beta &= \left.\frac{\partial}{\partial r}\right|_R I_1(kr) \\ &= kI_0(kR) - \frac{I_1(kR)}{R}\end{aligned} \tag{3.70}$$

To find A, we need boundary condition (3.53).

$$\begin{aligned} \left.\frac{\partial}{\partial r}\right|_R \Phi_1(r,t) &= -\frac{L_p}{2\pi} A\beta + \Phi_{1h} \\ &= 0 \end{aligned}$$

Therefore,

$$\begin{aligned} A &= \frac{\dot{B}^A}{\beta} \\ \Phi_{1h} &= \frac{L_p}{2\pi}\dot{B}^A \end{aligned}$$

The electric field components are thus

$$E_{||}(r,\phi,t) = \frac{\dot{B}^A}{\beta} I_1(kr)\cos\phi \tag{3.71}$$

$$\begin{aligned} E_\phi(r,\phi,t) &= -\frac{1}{r}\frac{\partial}{\partial\phi}\Phi(r,\phi,t) \\ &= \frac{L_p}{2\pi}\dot{B}^A\left(\frac{I_1(kr)}{\beta r} - 1\right)\cos\phi \end{aligned} \tag{3.72}$$

$$\begin{aligned} E_r(r,\phi,t) &= -\frac{\partial}{\partial r}\Phi(r,\phi,t) \\ &= \frac{L_p}{2\pi}\dot{B}^A\left(\frac{krI_0(kr) - I_1(kr)}{\beta r} - 1\right)\sin\phi \end{aligned} \tag{3.73}$$

The power dissipated for the first harmonic is

$$P = 2\pi R_0 \int_0^{2\pi}\int_0^R (\sigma_{||}E_{||}^2 + \sigma_\perp E_\phi^2 + \sigma_\perp E_r^2) r\, dr\, d\phi$$

The integrations are basically the same as those for the straight open-circuited

case. The power dissipated for the parallel and perpendicular components are

$$P_{||} = \sigma_{||}(2\pi R_0)(\pi R^2)(\dot{B}^A)^2 \frac{[I_1^2(kR) - I_0(kR)I_2(kR)]}{2\beta^2} \tag{3.74}$$

$$P_{\perp} = \sigma_{\perp}(2\pi R_0)(\pi R^2)(\dot{B}^A)^2(\frac{L_p}{2\pi})^2 \left\{1 - \frac{2}{\beta R}I_1(kR) - \frac{1}{2(\beta R)^2}\left[2I_1^2(kR) + (kR)^2[I_1^2(kR) - I_0^2(kR)]\right]\right\} \tag{3.75}$$

As $L_p \to \infty$ or $kR \to 0$,

$$P_{||} \to \frac{2(\dot{B}^A)^2}{\mu_0}\tau_{||}V \tag{3.76}$$

$$P_{\perp} \to 0 \tag{3.77}$$

where

$$\tau_{||} = \mu_0 \frac{R^2}{8}\sigma_{||} \tag{3.78}$$

$$V = (2\pi R_0)(\pi R^2) \tag{3.79}$$

This result matches that of the untwisted open-circuit infinite case discussed in section 3.1. The time constant is labeled the parallel time constant because it is associated with the diffusion time of the superconducting currents (current flowing parallel the superconductors). The time constant here is similar to the expression for the transport current time constant found in [22].

In the other, more realistic limit, when $kR \to \infty$,

$$E_{\phi} \to -\frac{L_p}{2\pi}\dot{B}^A \cos\phi \tag{3.80}$$

$$E_r(r, \phi, t) = -\frac{L_p}{2\pi}\dot{B}^A \sin\phi \tag{3.81}$$

$$P_{||} \rightarrow 0 \tag{3.82}$$

$$P_{\perp} \rightarrow \frac{1}{(kR)^2}\sigma_{||}(2\pi R_0)(\pi R^2)(\dot{B}^A R)^2$$

$$\rightarrow \frac{2(\dot{B}^A)^2}{\mu_0}\tau_{\perp} V \tag{3.83}$$

where

$$\tau_{\perp} = \frac{\mu_0}{2}\left(\frac{L_p}{2\pi}\right)^2 \sigma_{\perp} \tag{3.84}$$

This time constant is the familiar time constant of a single multifilamentary strand with helically twisted filaments of twist pitch L_p. This expression can be found in both [11] and [12]. Notice that the transverse fields E_ϕ and E_r simply add to a uniform negatively y-directed electric field of amplitude $\dot{B}^A L_p/2\pi$. A sketch of the cross-coupling currents due to this fields is shown in Fig. 3-7.

For a twist pitch $L_p = 2$ m, $\sigma_{\perp} = 1 \times 10^7$ mho/m and the same parameter values as in (3.45), the power dissipated is shown in figure 3-3. Surprisingly enough, the transport current loss is actually bigger than the usual "AC loss" due to the dipole currents. Notice a phase difference between graphs 3-2 and 3-3. This is due to the fact that there is considerable skin effect with the transport current because the $\mu_0\sigma_{||}\frac{\partial}{\partial t}$ term is significant.

One can see that the twist pitch is an important factor in reducing losses of a good conductor. Comparing this to the open circuited untwisted straight cable in eqn. 3.27, we obtain

$$\frac{P_{untwisted}}{P_{twisted}} \propto \left(\frac{2\pi L}{L_p}\right)^2 \tag{3.85}$$

Because the twist pitch and not the length of the cable limits the ac losses, it is advantageous to twist the wires.

3.3 Finite length twisted cable

Given a length of cable $2L$ and internal strands twisted with a pitch length L_p, the fields and power dissipation can be found for both shorted and open-circuited end conditions. The goal of this section is to derive analytic solutions for these conditions and to show under what conditions the assumption of an infinite cable may be used.

In steady-state, the governing equations are now

$$\nabla_T^2 E_{||} + \frac{\sigma_{||}}{\sigma_\perp}\left(\alpha\frac{\partial}{\partial\phi} + \frac{\partial}{\partial z}\right)^2 E_{||} = 0 \tag{3.86}$$

$$\nabla_T^2 \Phi = \frac{\sigma_{||}}{\sigma_\perp}\left(\alpha\frac{\partial}{\partial\phi} + \frac{\partial}{\partial z}\right) E_{||} \tag{3.87}$$

where $\alpha = \frac{2\pi}{L_p}$.

3.3.1 Short-circuited ends

The end conditions are, at $z = \pm L$,

$$\Phi(r,\phi) = 0 \tag{3.88}$$

The solutions for a varying B-field that satisfy boundary conditions at $r = R$ and the above end condition are

$$\begin{aligned}\Phi(r,\phi,z) &= \frac{2\dot{B}}{L}\left\{\sum_{p=1}\frac{E_{p1}}{k_p}\left[\beta_p r - I_1(kr)\right]\sin k_p z\cos(\phi-\alpha z)\right. \\ &\quad \left. -\sum_{p=0}\frac{E_{p2}}{k'_p}\left[\beta'_p r - I_1(k'r)\right]\cos k'_p z\sin(\phi-\alpha z)\right\} \qquad (3.89)\\ E_{||}(r,\phi,z) &= \frac{2\dot{B}}{L}\sum_{p=0}\{E_{p1}I_1(kr)\cos k_p z\cos(\phi-\alpha z)\end{aligned}$$

$$+E_{p2}I_1(kr)\sin k'_p z\sin(\phi-\alpha z)\Big\} \tag{3.90}$$

where

$$\begin{aligned}
k_p &= \frac{p\pi}{L} \\
k'_p &= (p+\frac{1}{2})\frac{\pi}{L} \\
k &= \sqrt{\frac{\sigma_{||}}{\sigma_\perp}}k_p \\
k' &= \sqrt{\frac{\sigma_{||}}{\sigma_\perp}}k'_p \\
\beta_p &= kI_0(kr)-\frac{I_1(kr)}{r} \\
\beta'_p &= k'I_0(k'r)-\frac{I_1(k'r)}{r} \\
E_{p1} &= \frac{\alpha}{\beta_p(\alpha^2-k_p^2)}\sin\alpha L\cos k_p L \\
E_{p2} &= \frac{\alpha}{\beta'_p(\alpha^2-k_p'^2)}\cos\alpha L\cos k_p L
\end{aligned} \tag{3.91}$$

The corresponding components of power dissipation are, for shorted ends,

$$P_{||} = (2\pi R)\left(\frac{R}{L}\right)\sigma_{||}\dot{B}^2\sum_p\left\{E_{p1}^2 f_{||}+E_{p2}^2 f'_{||}\right\} \tag{3.92}$$

$$P_r = (2\pi R)\left(\frac{R}{L}\right)\sigma_\perp\dot{B}^2\left\{\sum_{p=1}\left(\frac{E_{p1}}{k_pR}\right)^2 f_r+\sum_{p=0}\left(\frac{E_{p2}}{k'_pR}\right)^2 f'_r\right\} \tag{3.93}$$

$$P_\phi = (2\pi R)\left(\frac{R}{L}\right)\sigma_\perp\dot{B}^2\left\{\sum_{p=1}\left(\frac{E_{p1}}{k_pR}\right)^2 f_\phi+\sum_{p=0}\left(\frac{E_{p2}}{k'_pR}\right)^2 f'_\phi\right\} \tag{3.94}$$

where the functions are

$$f_{||} = I_1^2(kR)-I_0(kR)I_2(kR) \tag{3.95}$$

$$f_r = I_0^2(kR)[(kR)^2-1] - I_1^2(kR)[(kR)^2+1] - 4\beta_p R\left[I_1(kR) - \frac{I_0(kR)}{kR} + \frac{1}{kR}\right] + (\beta_p R)^2 + 1 \quad (3.96)$$

$$f_\phi = I_0^2(kR) - I_1^2(kR) - 4\frac{\beta_p}{k}[I_0(kR)-1] + (\beta_p R)^2 - 1 \quad (3.97)$$

For $f_{||}^{'}$, $f_r^{'}$, and $f_\phi^{'}$, replace the k's with k' in the above set of expressions.

3.3.2 Open-circuited ends

Here the end condition dictates no current to flow in or out at $z = \pm L$.

$$J_z = \sigma_{||} E_{||} = 0$$

Therefore,

$$E_{||} = 0 \quad (3.98)$$

The corresponding solutions for fields and power loss are

$$E_{||} = -\frac{2\dot{B}}{L}\left\{\sum_{p=1}\left(\frac{k_p E_{p1}}{\alpha}\right) I_1(kr)\sin k_p z \sin(\phi-\alpha z) + \sum_{p=0}\left(\frac{k_p' E_{p2}}{\alpha}\right) I_1(k'r)\sin k_p' z \sin(\phi-\alpha z)\right\} \quad (3.99)$$

$$\Phi(r,\phi,z) = -\frac{2\dot{B}}{L}\sum_{p=0}\left\{\frac{E_{p1}}{\alpha}[I_1(kr)-\beta_p r]\cos k_p z \sin(\phi-\alpha z) - \frac{E_{p2}}{\alpha}[I_1(kr)-\beta_p r]\sin k_p' z \cos(\phi-\alpha z)\right\} \quad (3.100)$$

$$P_{||} = (2\pi R)\left(\frac{R}{L}\right)\sigma_{||}\dot{B}^2\left\{\sum_{p=1}\left(\frac{k_p E_{p1}}{\alpha}\right)^2 f_{||} + \sum_{p=0}\left(\frac{k_p' E_{p2}}{\alpha}\right)^2 f_{||}^{'}\right\} \quad (3.101)$$

$$P_r = (2\pi R)\left(\frac{R}{L}\right)\sigma_\perp \dot{B}^2 \sum_{p=0}\left\{\left(\frac{E_{p1}}{\alpha R}\right)^2 f_r + \left(\frac{E_{p2}}{\alpha R}\right)^2 f_r^{'}\right\} \quad (3.102)$$

$$P_\phi = (2\pi R)\left(\frac{R}{L}\right)\sigma_\perp \dot{B}^2 \sum_{p=0}\left\{\left(\frac{E_{p1}}{\alpha R}\right)^2 f_\phi + \left(\frac{E_{p2}}{\alpha R}\right)^2 f'_\phi\right\} \tag{3.103}$$

A simple code was written that performs the summations in the field and power expressions. A cable with the following physical parameter values was used to generate field and power loss profiles:

$$\begin{aligned}
\dot{B}^A &= 1T/s \\
L_p &= 200\text{mm} \\
\sigma_\perp &= 1\times 10^7(\Omega\text{-m})^{-1} \\
\sigma_{||} &= 1\times 10^{11}(\Omega\text{-m})^{-1}(\text{close to saturation}) \\
R &= 10\text{mm}
\end{aligned}$$

Fig. 3-5(a) shows a plot of $J_{||}$ at $r = R$ near one of the ends for an open-circuit case. The flat part of the graph, which occupies the majority of the cable, has the same current density value as if it were treated as an infinite cable. Some oscillations near the end, at $z = 20$m, contribute to additional losses not otherwise predicted by an infinite cable model.

Fig. 3-5(b) shows the current density profile for short-circuited ends. Here, one can see that the behavior of the fields and current are strongly dependent on the relationship between L, the length of the cable, and L_p, the twist pitch. It seems the largest oscillations are induced when L is a multiple of L_p.

3.3.3 Short length limit

For cable lengths of the order of a twist pitch, the assumption that $\sqrt{\frac{\sigma_{||}}{\sigma_\perp}}\frac{\pi R}{L} >> 1$ holds true. The functions (3.96) and (3.97) reduce as follows. For $kR = 0$,

$$f_r = f_\phi = 0 \tag{3.104}$$

$$f_{||} = \frac{1}{2}R^2 \tag{3.105}$$

For $kR >> 1$, (all other terms)

$$f_r = f_\phi = (\beta_p R)^2 \tag{3.106}$$

$$f_{||} = \frac{1}{k^3 R} \tag{3.107}$$

Shorted ends are an attempt to model the very low resistant joints used to join cable sections to each other or to the power supply. Substituting the above expressions into the solutions for power loss, we obtain for shorted ends

$$P_{||} = (\pi R^2)(2L)\sigma_\perp \dot{B}^2 \left\{ \sum_{p=1} \left(\frac{\alpha}{k_p L}\right)^2 \frac{\sin^2 \alpha L}{(\alpha^2 - k_p^2)^2 kR} + \sum_{p=0} \left(\frac{\alpha}{k'_p L}\right)^2 \frac{\cos^2 \alpha L}{(\alpha^2 - k'^2_p)^2 k' R} + \frac{1}{2}\frac{\sigma_{||}}{\sigma_\perp}\left(\frac{R}{\alpha L}\right)^2 \sin^2 \alpha L \right\} \tag{3.108}$$

$$P_\perp = P_r + P_\phi = 2(\pi R^2)(2L)\sigma_\perp \dot{B}^2 \left\{ \sum_{p=1} \left(\frac{\alpha}{k_p L}\right)^2 \frac{\sin^2 \alpha L}{(\alpha^2 - k_p^2)^2} + \sum_{p=0} \left(\frac{\alpha}{k'_p L}\right)^2 \frac{\cos^2 \alpha L}{(\alpha^2 - k'^2_p)^2} \right\} \tag{3.109}$$

For the following nominal values,

$$\dot{B}^A = 1T/s$$

$$R = 10\text{mm}$$

$$\begin{aligned}\sigma_{||} &= 1 \times 10^{12}\Omega\text{-m}^{-1} \\ \sigma_{\perp} &= 1 \times 10^{7}\Omega\text{-m}^{-1} \\ L_p &= 200\text{mm}\end{aligned}$$

a plot of the total power loss normalized to the infinite cable result is shown in Fig. 3-6. One can see that the loss is highly sensitive to the length and its relation to the twist pitch. In fact, most of the contribution to the loss comes from the last term in $P_{||}$ which yields

$$P_{||} = \left(\frac{L_p}{2\pi}\right)^2 \frac{R}{L} R\sigma_{||}(\pi R^2 \dot{B}^2) \tag{3.110}$$

It can be deduced that it is more favorable to have the length of the cable a multiple of the twist pitch.

For cables left open on both ends (as is often done in AC loss experiments),

$$P_{\perp} = 2(\pi R^2)(2L)\sigma_{\perp}\dot{B}^2 \left\{ \sum_{p=1} \frac{\sin^2 \alpha L}{(\alpha^2 - k_p^2)^2 L^2} + \sum_{p=0} \frac{\cos^2 \alpha L}{(\alpha^2 - k_p'^2)^2 L^2} \right\} \tag{3.111}$$

$$P_{||} = (\pi R^2)(2L)\sigma_{\perp}\dot{B}^2 \left\{ \sum_{p=1} \frac{\sin^2 \alpha L}{(\alpha^2 - k_p^2)^2 L^2 kR} + \sum_{p=0} \frac{\cos^2 \alpha L}{(\alpha^2 - k_p'^2)^2 L^2 k' R} \right\} \tag{3.112}$$

It is immediately obvious that the contribution to loss from $P_{||}$ is small. It lacks the extra term that the shorted ends have. Therefore, it is a factor of $1/kR$ smaller than $P_{\perp}$.

Hartmann's thesis [13] (from the U. of Twente) treated the open ended cable where he assumed a current sheet. The expression derived in the thesis for the normalized power is

$$P_{tot}/P_{\infty} = 1 - \left(\frac{L_p}{2\pi L}\right)^2 \sin^2\left(\frac{2\pi L}{L_p}\right) \tag{3.113}$$

The cable problem he solved has no radial fields or currents and all of the transverse

fields were lumped into the ϕ component. Nevertheless, it seems to have yielded very similar results as the loss given in (3.111)-(3.112). A plot of P_{tot} normalized to the P_∞ is shown in Fig. 3-7.

3.3.4 Long length limit

If a cable is very long such that

$$kR \propto \sqrt{\frac{\sigma_{||}}{\sigma_\perp}}\left(\frac{R}{L}\right) << 1 \tag{3.114}$$

the fields and power loss expressions can be drastically simplified.

On inspection of the terms in the summations for $P_{||}$ for both shorted and open ends, it is clear that the most dominant term is when $\alpha \approx k_p$ due to the $\frac{1}{\alpha^2-k_p^2}$ dependence in E_{p1}. If $L >> L_p$, which is consistent with the long cable criterion, the peak of E_{p1} around $\alpha \approx k_p$ become sharper with increasing L/L_p ratio. Therefore, it is safe to estimate that the $k_p \approx \alpha$ term is the major term in the power summations and that the other terms may be neglected. Therefore,

$$E_{p1} = \frac{\alpha}{\beta_p(\alpha^2 - k_p^2)} \sin \alpha L \cos k_p L \approx \frac{L}{k} \tag{3.115}$$

Since p is always even for $\alpha = k_p$, $\cos k_p L = 1$.

Taking the asymptotic limit of the Bessel functions, we have

$$\begin{aligned} I_0(kR) &= \frac{e^{kR}}{\sqrt{2\pi kR}}(1 + \frac{1}{8kR}) \\ I_1(kR) &= \frac{e^{kR}}{\sqrt{2\pi kR}}(1 - \frac{3}{8kR}) \\ I_0(kR) &= \frac{e^{kR}}{\sqrt{2\pi kR}}(1 - \frac{15}{8kR}) \end{aligned}$$

For both shorted and open ends, the results converge.

$$P_{||} \approx \frac{1}{4}(\pi R^2)(2L)\left(\frac{L_p}{2\pi R}\right)\sqrt{\frac{\sigma_\perp}{\sigma_{||}}}\dot{B}^2\sigma_\perp\left(\frac{L_p}{2\pi}\right)^2 \tag{3.116}$$

$$P_\perp \approx (\pi R^2)(2L)\dot{B}^2\sigma_\perp\left(\frac{L_p}{2\pi}\right)^2 \tag{3.117}$$

Do the results for $P_\perp$ look familiar? They are the same as the ones derived in section 3.2.2 where the cable is assumed to be infinite! When L is much greater than L_p and satisfies (3.114), losses for all 3 cases (the short, open, and infinite cable) converge.

Therefore, in order to justify the formulation of an infinite cable problem, the criterion is that $\sqrt{\frac{\sigma_{||}}{\sigma_\perp}}\left(\frac{R}{L}\right) << 1$. As an example of how this affects a real magnet, let's examine the dimensions of an ITER cable. For $\sigma_{||} = 1 \times 10^{12}(\Omega\text{-m})^{-1}$ (a number between superconducting and saturated state), $\sigma_\perp = 1 \times 10^6(\Omega\text{-m})^{-1}$, and R=19mm,

$$L >> 19\text{m} \tag{3.118}$$

This is a reasonably short length, considering that a section of cable (from one joint region to the next) is several meters long. Even if one takes the unsaturated value, $\sigma_{||} = 1 \times 10^{14}(\Omega - m)^{-1}$, this still only requires $L >>$ 190m, which is well satisfied. Therefore, using an infinite cable model is a valid assumption.

3.4 Conclusion

What resulted is a set of solutions comprised of old familiar expressions and new ones. The table at the end of the chapter lists the results for different geometries and end conditions assuming a0 good conductor. The following is a brief synopsis of the

major discoveries of this chapter:

- The difference between a non-twisted cable of length L and one twisted with a pitch length of L_p is that the power density loss is proportional to L^2 for straight wires whereas the power density loss is proportional to L_p^2 for twisted wires. Therefore, twisting the filaments (as in the case of a strand) or wires limits the loss to the pitch length rather than the length of the entire cable.

- For shorted ends, an approximation to joints in a real magnet, the condition where $\sqrt{\frac{\sigma_{||}}{\sigma_\perp}}\left(\frac{R}{L}\right) << 1$, must be satisfied in order for the assumptions of an infinite cable to be valid. R is the radius and $2L$ is the length of the cable. For open ends, which are often the case with loss experiments, the less stringent criterion that $\left(\frac{2\pi L_p}{L}\right)^2 << 1$ must hold true for the infinite cable model to apply.

- For a helically twisted cable, there is a perpendicular time constant associated with the diffusion time of cross-coupling currents, $\tau_\perp = \frac{\mu_0}{2}\sigma_\perp\left(\frac{L_p}{2\pi}\right)^2$, which can be found in most literature on losses in multifilamentary strands. There is a parallel time constant associated with diffusion time of superconducting dipole or transport current,$\tau_{||} = \mu_0\sigma_{||}\frac{R^2}{8}$. This expression for the time constant is very similar to the one in [22].

- For magnets in persistent mode, i.e. in a closed loop formation, the nature of flux conservancy of these current loops dictate large amounts of transport current induced due to time-varying fields. These in turn produce large transport current loss and is the only time one would expect transport current loss to exceed cross-coupling current loss (the more traditional AC loss source).

Case	Coupling current power loss	Transport current power loss
Untwisted open-ckt. of length $2L$	$12L^3\sigma_\perp(\pi R^2\dot{B}^2)$	negligible
Short-ckt. loop of radius R_o	$(2\pi R_0)\left(\frac{L_p}{2\pi}\right)^2\sigma_\perp(\pi R^2\dot{B}^2)$	$\frac{(2\pi R_0)^3}{8C^2}\left(\frac{\delta}{R}\right)^2\sigma_\parallel(\pi R^2 f^2 {B_0}^2)$ (rms value for sin. excitation of freq f and amplitude B_0. δ is skin depth.)
Infinite cable (Long length limit)	$\left(\frac{L_p}{2\pi}\right)^2\sigma_\perp(\pi R^2\dot{B}^2)$ (per unit length)	negligible
Twisted short-ckt. (short lengths of length $2L$)	$\left(\frac{R}{L}\right)^2 L\left(\frac{L_p}{2\pi}\right)^2\sigma_\parallel(\pi R^2\dot{B}^2)\sin^2(\frac{2\pi L}{L_p})$ $+2L\left(\frac{L_p}{2\pi}\right)^2\sigma_\perp(\pi R^2\dot{B}^2)$	negligible
Twisted open-ckt. (short lengths of length $2L$)	$2L\left(\frac{L_p}{2\pi}\right)^2\sigma_\perp(\pi R^2\dot{B}^2)\left[1-\frac{L_p}{2\pi L}\sin^2(\frac{2\pi L}{L_p})\right]$	negligible

Table 3.1: This table lists the analytic expressions for power loss in the limit where $\sqrt{\frac{\sigma_\parallel}{\sigma_\perp}}\frac{R}{L_p} >> 1$.

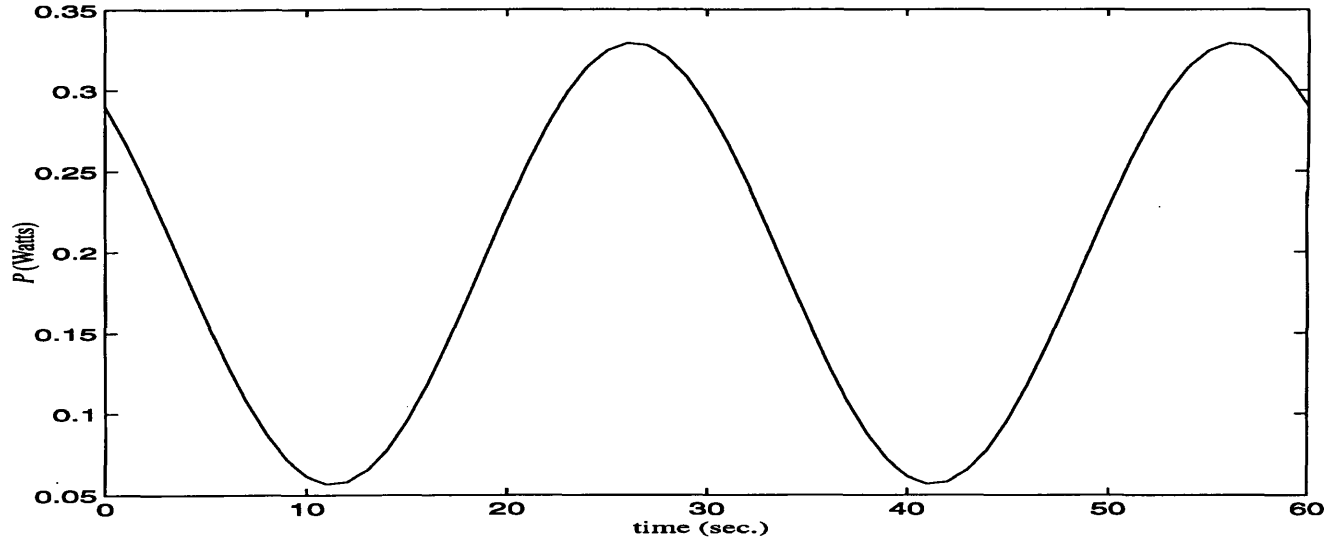

Figure 3-2: Transport current loss for a persistent loop.

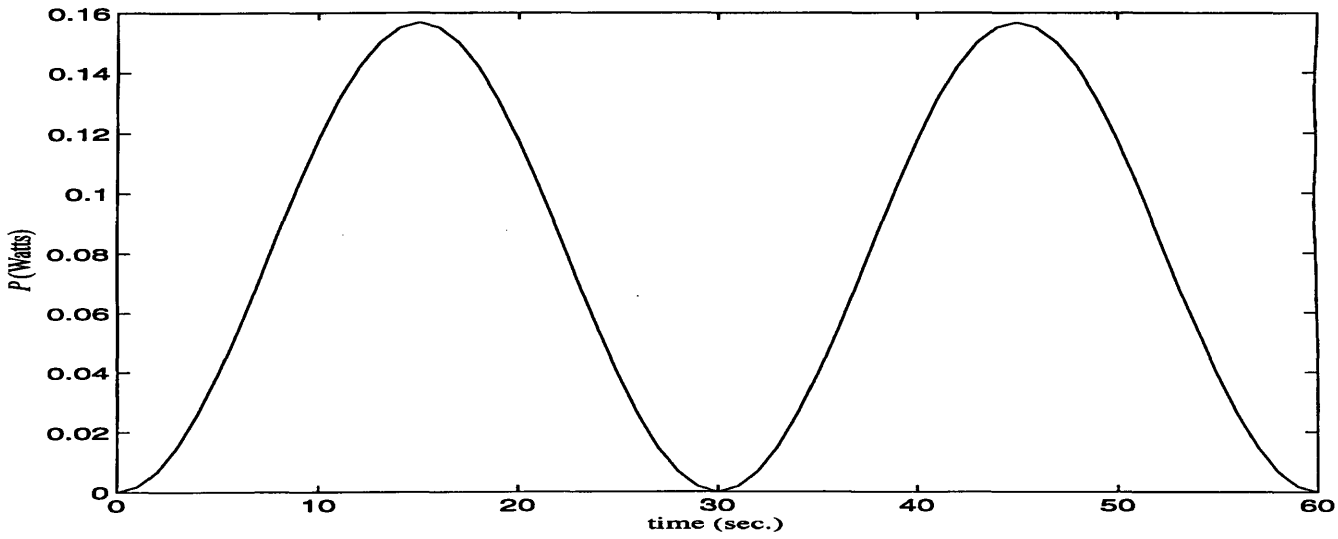

Figure 3-3: Dipole current loss for a persistent loop.

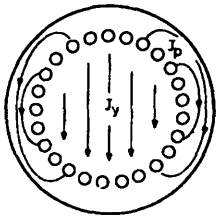

Figure 3-4: Coupling currents inside the conductor

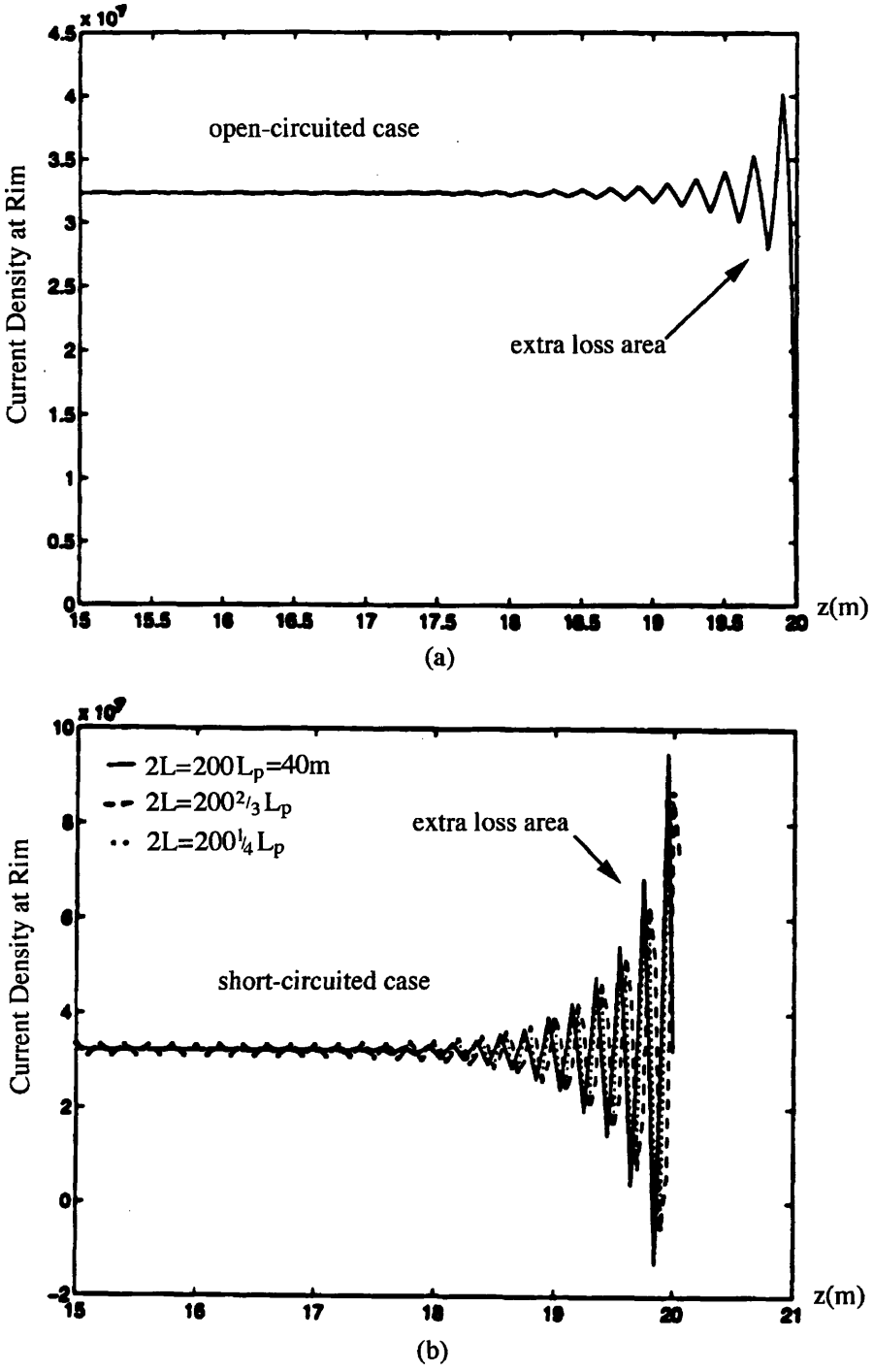

Figure 3-5: Current density profiles at rim of cable near (a) shorted and (b) open-circuited ends

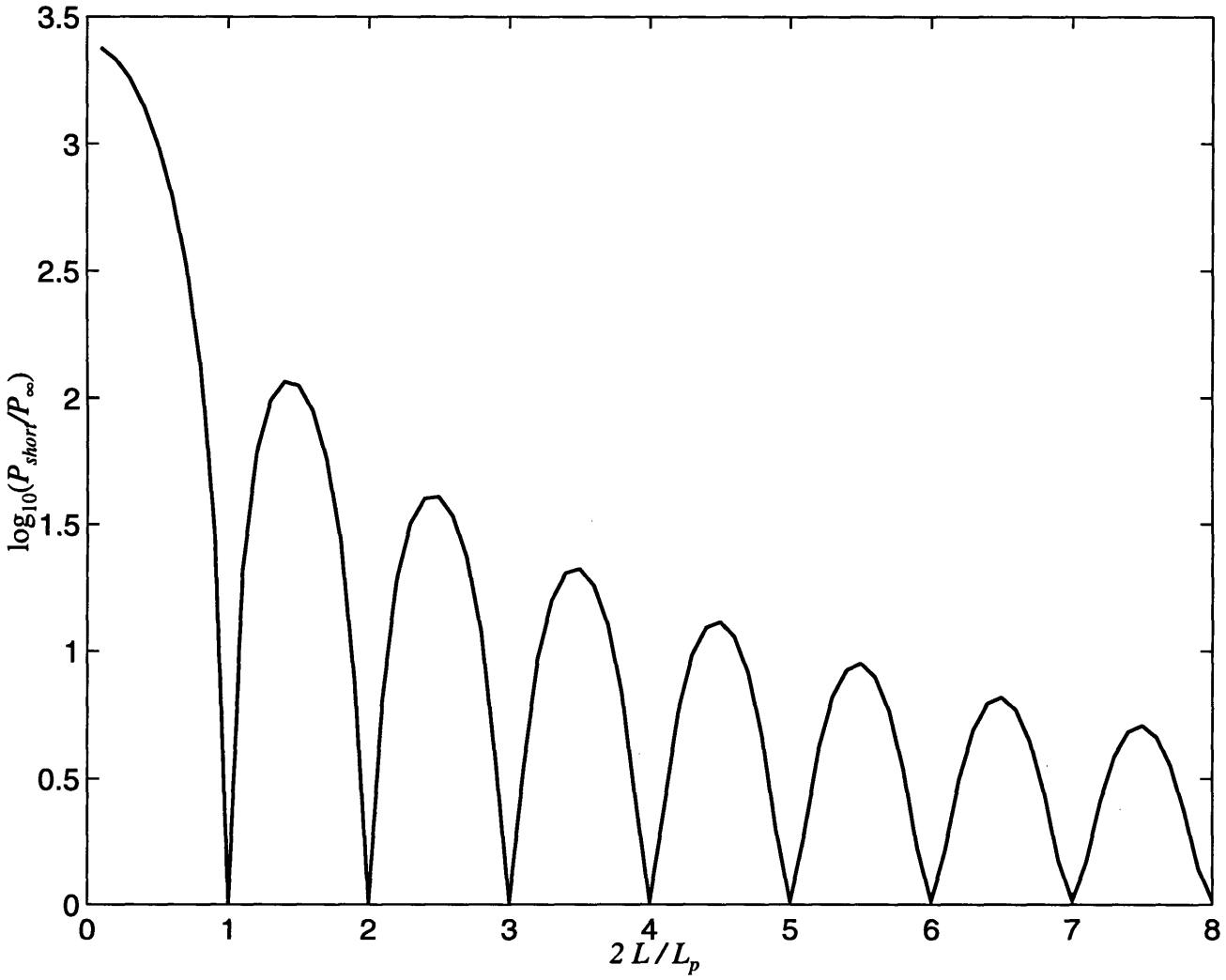

Figure 3-6: Power loss for shorted ends normalized to infinite cable

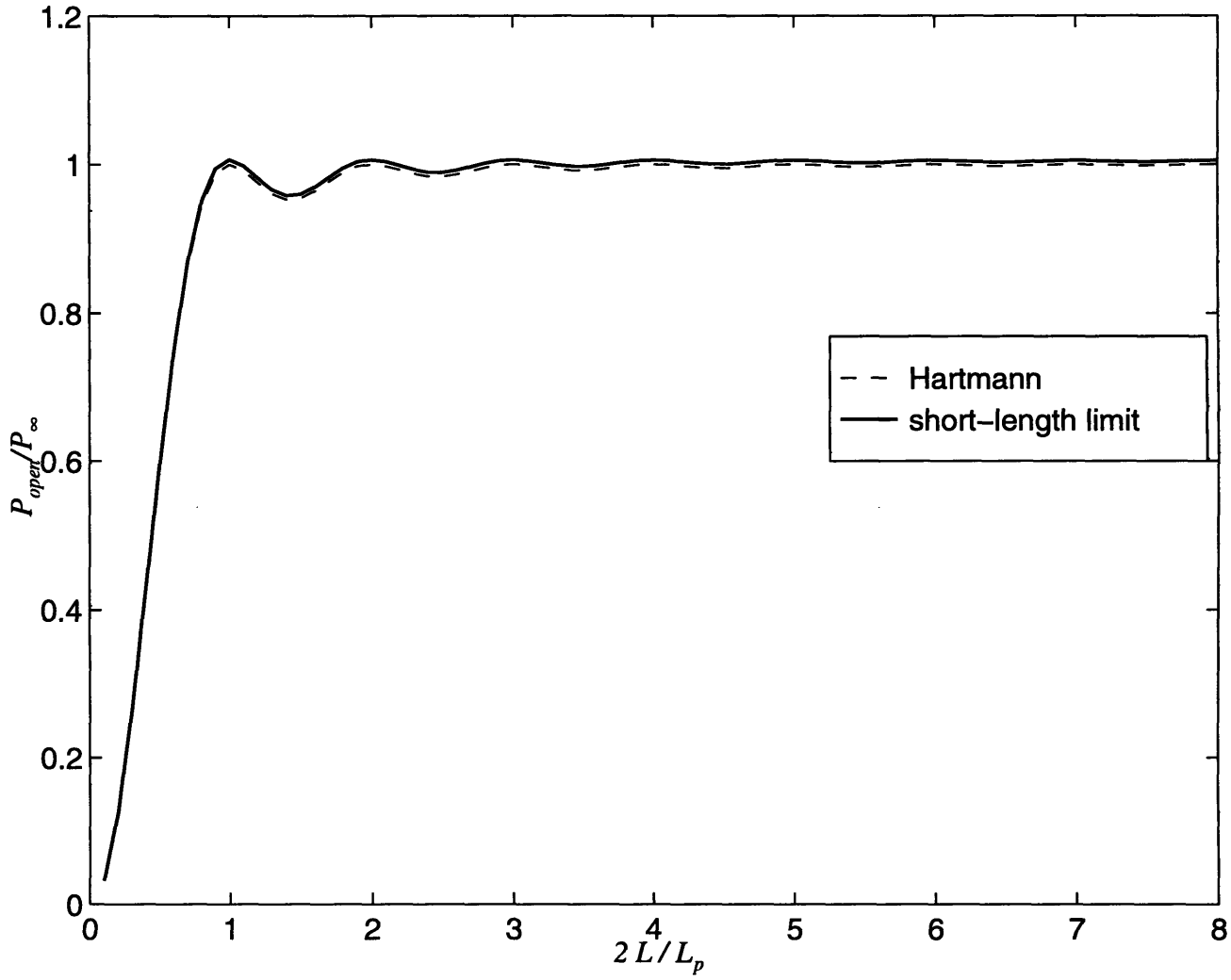

Figure 3-7: Power loss for open ends normalized to infinite cable as compared to analytically-derived expression from [13].

Chapter 4

2D code

A class of problems exist where the geometry is z-invariant. These can be solved by a "2D code" which we have developed. In most cases, the radial motion ($\dot{\rho}$) of a strand is usually the parameter that contributes to the three-dimensionality of the geometry. In addition, boundary conditions that are z-dependent can make a problem three-dimensional as well. A long cable which is either straight or has a single twist pitch is accurately described by a 2D model.

Another interesting 2D problem concerns the single strand itself. Multifilamentary strands of infinite length, with embedded superconducting filaments twisted such that each of them trace out a helical path of fixed radius, can also be solved in two dimensions - r and ϕ. At present, a compact, efficient code for solving for currents and losses is still lacking in the study of AC losses in 2 and 3 dimensions. However, simple analytical expressions exist for losses that are adequate for some cases. It is the intention of this section to make a comparison among closed form solutions found in literature, those derived in chapter 3, and results from the 2D code.

The following strand geometries and conditions are considered (see fig. 4-1):

1. MFZ only (no shell or core); linear $\sigma_{||}$, constant j_c, ramped field

2. MFZ + outer shell; ramped field

3. MFZ + inner core + outer shell; ripple field

4. MFZ only - ramped field and dc transport current

Each of these cases are compared against existing formulations.

4.1 Numerics

For an infinitely long helically twisted strand or cable, the physical parameters $\dot{\rho} = 0$ and $\frac{\partial}{\partial z} = 0$. The governing equations (2.21) and (2.22) then reduce to

$$\nabla_T^2 \left(E_{||} + \frac{\rho\dot{\psi}(r,\phi)}{r} \frac{\partial}{\partial \phi} \Phi \right) = \mu_0 \frac{\partial}{\partial t} \sigma_{||} E_{||} \tag{4.1}$$

$$\sigma_\perp \nabla_T^2 \Phi = \frac{1}{r} \frac{\partial}{\partial \phi} \left(\rho\dot{\psi}(r,\phi) \sigma_{||} E_{||} \right) \tag{4.2}$$

Expanding both equations and substituting the second into the first, we obtain

$$\nabla_T^2 E_{||} + \frac{\rho\dot{\psi}}{r} \left[\frac{\rho\dot{\psi}}{r} \frac{\partial^2}{\partial \phi^2} + 2\left(\frac{\partial}{\partial \phi} \frac{\rho\dot{\psi}}{r}\right) \frac{\partial}{\partial \phi} + \left(\frac{\partial^2}{\partial \phi^2} \frac{\rho\dot{\psi}}{r}\right) \right] \frac{\sigma_{||}}{\sigma_\perp} E_{||}$$
$$+ \left[\nabla_T^2 \left(\frac{\rho\dot{\psi}}{r}\right) + 2\left(\frac{\partial}{\partial r} \left(\frac{\rho\dot{\psi}}{r}\right) \frac{\partial}{\partial r} + \frac{1}{r^2} \left(\frac{\partial}{\partial \phi} \frac{\rho\dot{\psi}}{r} \right) \frac{\partial}{\partial \phi} \right) \right] \frac{\partial}{\partial \phi} \Phi = \mu_0 \frac{\partial}{\partial t} \sigma_{||} E_{||} \tag{4.3}$$

$$\nabla_T^2 \Phi = \frac{1}{\sigma_\perp} \left[\frac{1}{r} \left(\frac{\partial}{\partial \phi} \frac{\rho\dot{\psi}}{r} \right) \sigma_{||} E_{||} + \frac{\rho\dot{\psi}}{r} \frac{\partial}{\partial \phi} (\sigma_{||} E_{||}) \right] \tag{4.4}$$

With a single helicity cable or a multifilamentary strand, the filaments are twisted with one twist pitch of length L_p. This yields $\rho\dot{\psi} = \frac{2\pi}{L_p} r$ which reduces the equations

even further to

$$\nabla_T^2 E_{||} + \left(\frac{2\pi}{L_p}\right)^2 \frac{\partial^2}{\partial\phi^2}(\sigma_{||}E_{||}) = \mu_0 \frac{\partial}{\partial t}(\sigma_{||}E_{||}) \tag{4.5}$$

$$\nabla_T^2 \Phi = \frac{1}{\sigma_\perp}\frac{2\pi}{L_p}\frac{\partial}{\partial\phi}(\sigma_{||}E_{||}) \tag{4.6}$$

The basic approach is to Fourier decompose the equations and solve for each harmonic of $E_{||}$ and Φ. Assuming both to be summations of their Fourier components in ϕ, we can define the two variables as

$$E_{||}(r,\phi,t) = \sum_n E_n(r,t)\cos\phi \tag{4.7}$$

$$\Phi(r,\phi,t) = \sum_n \Phi_n(r,t)\sin\phi \tag{4.8}$$

to fit the boundary conditions. The time derivative on the right hand side of (4.5) can be treated with a second order forward differencing scheme. The time-differencing scheme, carried to the second order is given by

$$\frac{dJ(t)}{dt} \approx \frac{1}{C}[AJ(t) - BJ(t-\Delta t_1) + J(t-\Delta t_1 - \Delta t_2)] \tag{4.9}$$

where

$$A = \frac{(\Delta t_1 + \Delta t_2)^2}{\Delta t_1^2} - 1 \tag{4.10}$$

$$B = A + 1 \tag{4.11}$$

$$C = \frac{\Delta t_2}{\Delta t_1}(\Delta t_1 + \Delta t_2) \tag{4.12}$$

Thus, (4.5) and (4.6) transform into a set of 2xn number of coupled 1D ODE's. To extract the differential equations for the nth harmonic, we must integrate (4.5)

through by

$$\frac{1}{(2)\pi}\int_0^{2\pi}\cos n\phi d\phi$$

and (4.6) by

$$\frac{1}{(2)\pi}\int_0^{2\pi}\sin n\phi d\phi$$

After Fourier decomposition, the sets of equations are

$$\left(\frac{1}{r}\frac{\partial}{\partial r}r\frac{\partial}{\partial r}-\frac{n^2}{r^2}\right)E_n^i(r)+\left(\frac{2\pi}{L_p}\right)^2\int_0^{2\pi}\frac{\partial^2}{\partial\phi^2}\left(\sigma_{||}^i\sum_m E_m^i(r)\cos m\phi\right)\cos n\phi d\phi =$$
$$\mu_0\int_0^{2\pi}\left(A\sigma_{||}^iE_m^i-B\sigma_{||}^{i-1}+C\sigma_{||}^{i-2}E_m^{i-2}\right)\cos m\phi\cos n\phi d\phi \quad (4.13)$$

$$\left(\frac{1}{r}\frac{\partial}{\partial r}r\frac{\partial}{\partial r}-\frac{n^2}{r^2}\right)\Phi_n^i(r)=\frac{2\pi}{L_p}\int_0^{2\pi}\frac{\partial}{\partial\phi}\left(\sigma_{||}(E_{||})\sum_m E_m^i(r)\cos m\phi\right)\sin n\phi d\phi \quad (4.14)$$

where the subscripts $i, i-1$, and $i-2$ denote the present, previous, and second previous time step, respectively. These equations are fed into a general ODE solver named COLSYS [19]. Remember that $\sigma_{||}$ is dependent on the magnitude of $E_{||}$ and $\dot{B}$.

For simplicity, we will make the assumption that $\dot{B}\approx\dot{B}^A$ for the calculation of $\sigma_{||}$. Since these are non-linear equations, the most straightforward and robust method was to solve them fully-implicitly since COLSYS has the capability to solve nonlinear equations. Unfortunately, not only did COLSYS take a long time to search for the solution, often times a solution was not even found.

The second approach was to feed these as linear equations into COLSYS and iterate to the correct solution. Since $\sigma_{||}$ is a function of $E_{||}$, one can do a linear projection of $E_{||}$ based on the previous time steps for the purpose of finding $\sigma_{||}$. For the initial guess,

$$E_{||}^i=2E_{||}^{i-1}-E_{||}^{i-2} \quad (4.15)$$

The predicted $\sigma_{||}$ value is plugged into the equations and a new set of $E_{||}$ values are calculated. These are then used to find $\sigma_{||}$ again and the whole process is iterated until some error tolerance is achieved. The code then increments to the next time step.

In the original version of the code, the Fourier integrals were evaluated using the Romberg integration method. This turned out to be very time consuming. To save computation time, a mesh was set up whereby the integrals in (4.13) and (4.14) were evaluated at fixed points in r and then given to COLSYS. The values of the integrals were then interpolated from the mesh as needed.

This strategy, albeit a time saver, introduced new numerical difficulties. Because the Fourier integral coefficients have sharp gradients (they are directly proportional to the ratio $\sigma_{||}/\sigma_{\perp}$), small errors introduced by the interpolation scheme could lead to instabilities and error in the results. Therefore, a new approach was devised.

The general derivative of $J_{||}$, i.e. $\frac{\partial}{\partial \bar{x}}(\sigma_{||}E_{||})$, can be rewritten as

$$\begin{aligned}\frac{\partial}{\partial \bar{x}}(\sigma_{||}E_{||}) &= \sigma_{||}\frac{\partial}{\partial \bar{x}}E_{||} + E_{||}\frac{\partial}{\partial \bar{x}}\sigma_{||} \\ &= (\sigma_{||} + \frac{\partial}{\partial E_{||}}\sigma_{||})\frac{\partial}{\partial \bar{x}}E_{||} \\ &= \sigma\frac{\partial}{\partial \bar{x}}E_{||} \end{aligned} \tag{4.16}$$

It was discovered that σ has a very simple form where

$$\sigma = \begin{cases} \lambda\frac{j_c}{\epsilon_0} & \text{if } \left|E_{||}\right| \leq \varepsilon_0 \\ (1-\lambda)\sigma_{cu} & \text{if } \left|E_{||}\right| \geq \varepsilon_0 \end{cases} \tag{4.17}$$

This allows one to integrate the Fourier integrals analytically!

The Fourier integrals in (4.13) and (4.14) reduce to

$$\left(\frac{1}{r}\frac{\partial}{\partial r}r\frac{\partial}{\partial r}-\frac{n^2}{r^2}\right)E_n^i(r)-\left(\frac{2\pi}{L_p}\right)^2\sum_m mE_m^i(r)\int_0^{2\pi}\frac{\partial}{\partial\phi}(\sigma\sin m\phi)\cos n\phi\,d\phi=$$
$$\frac{\mu_0}{C}\sum_m\left(AE_m^i-BE_m^{i-1}+E_m^{i-2}\right)\int_0^{2\pi}\sigma\cos m\phi\cos n\phi d\phi \qquad (4.18)$$

$$\left(\frac{1}{r}\frac{\partial}{\partial r}r\frac{\partial}{\partial r}-\frac{n^2}{r^2}\right)\Phi_n^i(r)=-\frac{2\pi}{L_p}\sum_m E_m^i(r)\int_0^{2\pi}\sigma\sin m\phi\sin n\phi d\phi \qquad (4.19)$$

Unfortunately, the integrand in the first Fourier integral

$$\frac{\partial}{\partial\phi}(\sigma\sin m\phi)\cos n\phi$$

contains delta functions due to the step-function transition of σ at $|E_{||}|=\varepsilon_0$. In order to avoid this particular numerical anomaly, one can convert this Fourier integral into something more user-friendly.

$$\begin{aligned}\sum_m mE_m\int_0^{2\pi}\frac{\partial}{\partial\phi}(\sigma\sin m\phi)\cos n\phi d\phi&\\ &=\sum_m mE_m\left[(\sigma\sin m\phi\cos n\phi)|_0^{2\pi}+\int_0^{2\pi}n\sigma\sin m\phi\sin n\phi d\phi\right]\\ &=n\sum_m mE_m\int_0^{2\pi}\sigma\sin m\phi\sin n\phi d\phi \qquad (4.20)\end{aligned}$$

The first term is zero since σ is a periodic function. Therefore, the equations now look, in the form to be used by COLSYS,

$$\begin{aligned}\frac{\partial^2}{\partial r^2}E_n^i&=\left(-\frac{1}{r}\frac{\partial}{\partial r}+\frac{n^2}{r^2}\right)E_n^i+\left(\frac{2\pi}{L_p}\right)^2 n\sum_m mSS(m,n)E_m^i\\ &\quad+\frac{\mu_0}{C}\sum_m CC(m,n)(AE_m^i-BE_m^{i-1}+E_m^{i-2}) \qquad (4.21)\\ \frac{\partial^2}{\partial r^2}\Phi_n^i&=\left(-\frac{1}{r}\frac{\partial}{\partial r}+\frac{n^2}{r^2}\right)\Phi_n^i-\left(\frac{2\pi}{L_p}\right)\sum_m mSS(m,n)E_m^i \qquad (4.22)\end{aligned}$$

where

$$SS(m,n) = \int_0^{2\pi} \sigma \sin m\phi \sin n\phi d\phi \tag{4.23}$$

$$CC(m,n) = \int_0^{2\pi} \sigma \cos m\phi \cos n\phi d\phi \tag{4.24}$$

The code is also capable of solving for a strand with a normal metal shell and/or core. Fpr copper, $\sigma_\perp$ transitions from σ_{cu} to $\frac{(1-\lambda)}{(1+\lambda)}\sigma_{cu}$ at the boundary between the copper region and the superconducting matrix. This gives equation 4.4 an extra term. The left hand side now looks

$$\nabla_T \cdot (\sigma_\perp \nabla_T \Phi) = \frac{\partial}{\partial r}\sigma_\perp \frac{\partial}{\partial r}\Phi + \sigma_\perp \nabla_T^2 \Phi \tag{4.25}$$

At the boundary between the normal conducting region and the superconducting matrix, $\sigma_\perp$ goes through a sharp transition. At either side of the boundary, $\frac{\partial}{\partial r}\sigma_\perp = 0$. One can actually cirumvent this transition numerically. There is an input to COLSYS named FIXPNT which are points other than the boundaries that are "fixed points" in the meshes COLSYS creates. It is actually *between* mesh points that the equations are evaluated. Thus, specifying the radius of the boundary as a fixed point will prevent COLSYS from evaluating the equations at that point where the conductivities are discontinuous.

For either a pure transport current or external field excitation, the number of ϕ harmonics needed is small. In fact, one could get away with using the same harmonics as the excitation. The zeroth harmonic is needed for transport current and the 1st harmonic is neede for an external B-field (see chapter 2). When both sources are excited, there is strong coupling between the zeroth and first harmonic which leads to appearance of higher harmonics.

The initial temporal step size used is 1/100th the estimated time constant of the geometry. For a strand, the perpendicular time constant is typically of the order of a millisecond which means that Δt is of the order of 10μsec. The other restraint on Δt is the level of saturation. Δt must be small enough so that the first two time steps are not in the saturation regime. The code automatically adjusts Δt for efficiency as it progresses in time.

Once saturation occurs, the code iterates to produce the "correct" solution, or at least to converge to the specified tolerance at each time step. For an error tolerance of 1e-4, the typical number of iterations at each time step is under 10, with 1 iteration for below saturation. This, of course, depends on the level of saturation. On a DEC Alpha machine, an iteration averages .15sec for 2 harmonics(0th and 1st) or 8 equations and .3sec for 4 harmonics(0th-3rd) or 16 equations. Above saturation, 2 harmonics yield a CPU time of 1.19sec/iteration and 4 harmonics yield 1.5sec/iteration. When the strand/cable is saturated, the CPU time goes up a factor 5 to 8 times(per iteration). This is mainly due to the evaluation of the σ Fourier integrals in (4.23) and (4.24) and the evaluation of the $P_{||}$ integral. A typical run with saturation will take about 2 hours.

4.2 Benchmark cases

Four sets of cases are presented to verify results from the code. The first wire geometry has only a multifilamentary region (no inner or outer stabilizers) and is for illustration purposes only. $\sigma_{||}$ is set to a constant and the external B-field is ramped until steady state is reached. The numerical results for field profiles and losses are matched against analytic solutions derived in chapter 2.

The second set of results are for a wire with the same dimensions as the first

case except that there is a thin outer normal conducting shell of varying thickness as shown in fig. 4-1. Loss results generated by the code are compared against loss expressions for thin outer shell geometries found in Wilson [11] and those derived by Turck [24] without the thin shell approximation.

The third cluster of data aims to show the effect of a sinusoidal field on an actual wire geometry. These cases are important to such applications as superconducting generators and motors, and MAGLEV where sinusoidal fields are the mode of operation. The loss values for varying frequencies are compared against existing expressions found in Wilson, Turck, and Ito [26].

Finally, the tricky condition where transport current and B-field changes occur simultaneously is examined. The physical parameters are taken from Sumiyoshi [22]. A wire with an initially uniform transport current density is subjected to an externally ramped B-field and the transport current distribution is analyzed and compared against existing hypotheses.

These sets of results are used to validate the code. They are in no way an exclusive nor exhaustive set.

4.2.1 Case 1: Linear conductivity

The purpose of this run is to compare fields and loss values generated by the code against equations 2.21 and 2.22 where $\sigma_{||}$ is assumed to be linear.

The agreement between analytical solutions and that produced by the code is exact. The code was executed to ten times the perpendicular time constant $\tau_{\perp}$ (see eqn. 3.84). Figures 4-2 to 4-4 show a comparison of $E_{||}$, E_{ϕ}, and E_r as generated by the code and analytic solutions for the following values:

$$\dot{B}^A = 1\text{T/sec}$$
$$r_f = 8\mu\text{m}$$
$$R_1 = R_f = .405\text{mm}$$
$$L_p = 4.05\text{mm}$$
$$j_c = 1\times10^9\text{A/m}^2$$
$$\lambda = .5$$
$$\sigma_{cu} = 2\times10^9(\Omega\text{-m})^{-1}$$

For all of the runs, $\sigma_\perp = (1-\lambda)/(1+\lambda)\sigma_{cu}$.

4.2.2 Case 2: Wire with thin normalconducting shell

Expression of losses for multifilamentary strands with a thin normal conducting shell/sheath can be found in Wilson. An effective time constant was found for this geometry assuming a thin shell approximation ($R_1 - R_f << R_f$). (A more in-depth derivation of multilayer geometry can be found in the next section.)

$$\tau = \frac{\mu_0}{2\rho_{eff}}\left(\frac{L_p}{2\pi}\right)^2 \tag{4.26}$$

where

$$\frac{1}{\rho_{eff}} = \left(\frac{R_f^2}{R_1^2}\right)\left[\sigma_\perp + \sigma_{cu}\frac{R_1 - R_f}{R_f} + \sigma_{cu}R_f(R_1 - R_f)\left(\frac{2\pi}{L_p}\right)^2\right] \tag{4.27}$$

The last term is associated with what literature coins as 'eddy current loss'. A distinction is made between axial currents flowing in the shell as a result of normal eddy currents due to a time-varying B-field and 'coupling' losses due to transverse currents caused by induced voltages in the multifilamentary region. The first two terms in the above equation contribute to the coupling loss and the last term contributes to the eddy current loss.

For a ramped field, the steady state power loss per unit volume is simply

$$p_d = 2\frac{\dot{B}_i^2}{\mu_0}\tau \tag{4.28}$$

where B_i is the internal electric field.

Fig. 4-5 shows the comparison between numerical results and the above expression given the following parameter values.

$$\dot{B}^A = 1\text{T/sec}$$
$$r_f = 8\mu\text{m}$$
$$R_1 = .405\text{mm}$$
$$L_p = 4.05\text{mm}$$
$$j_c = 1\times10^8\text{A/m}^2$$
$$\lambda = .5$$
$$\sigma_{cu} = 2\times10^9(\Omega\text{-m})^{-1}$$

One can see that the thin shell approximation deviates from code results with increasing shell thickness.

4.2.3 Case 3: Multilayer wire - SSC NbTi strand

The physical parameters for the NbTi multifilamentary strand proposed for the SSC project is used in the third set of runs. The strand, schematically drawn in 4-1 and pictured in 4-6, has a central copper core, a multifilamentary zone (MFZ), and a surrounding copper sheath. A bias field of 3T with a 10% peak-to-peak ripple is used as the excitation. It is also to show the capability of the code in solving multimedia conductors and in handling excitations of various waveforms. The dimensions are

$$B_{dc} = 3.0T$$

$$r_f = 7.2\mu\text{m}$$

$$R_1 = .404\text{mm}$$

$$R_f = .324\text{mm}$$

$$R_0 = .112\text{mm}$$

$$L_p = 12.7\text{mm}$$

$$j_c(B) = \text{critical current density as a function of } B$$

$$\lambda = .3775$$

$$\sigma_{cu} = 1/\rho_{cu}$$

where

$$\rho_{cu} = \rho_a/\rho_b + \rho_c B_{dc}$$

$$\rho_a = 2.0\times10^{-8}(\Omega\text{-m})$$

$$\rho_b = 40.0$$

$$\rho_c = 4.8\times10^{-11}(\Omega\text{-m})/\text{T}$$

Ito and Turck have derived analytic expressions for multizone conductors which have also been experimentally verified. Their derivations (with a slight modification to include eddy current loss in the core) will be used to benchmark the code results.

Turck's formulation

Expressions for steady-state field and potential distributions were derived for multiple layers of normal conductors surrounding a multifilamentary zone region. Here we will review his derivations specifically for our NbTi wire.

Any shielding effect of the outer layer on the multifilamentary region was neglected. This is a fairly valid assumption since skin depth for copper or any other normal metal is much larger compared to that of a superconductor. Therefore, the

solution for the potential distribution at R_f is the same with or without the normal metal sheath(s). The familiar equation for the steady-state electric potential is

$$V = \left(\frac{L_p}{2\pi}\right) \dot{B}^A r \sin\phi \tag{4.29}$$

This dictates the boundary condition for the inner rim of the sheath ($r = R_f$).

At the outer rim of the wire, the boundary condition is

$$J_r(r = R_1) = 0 \tag{4.30}$$

or

$$E_r(r = R_1) = -\frac{\partial}{\partial r} V = 0 \tag{4.31}$$

In steady state, the potential satisfies Laplace's equation

$$\nabla_T^2 V = 0 \tag{4.32}$$

A solution to V is of the form

$$V(r, \phi) = (ar + \frac{b}{r}) \sin\phi \tag{4.33}$$

where a and b are constants determined by boundary conditions given in (4.29) and (4.31). At $r = R_f$,

$$V = (aR_f + \frac{b}{R_f}) \sin\phi = \frac{L_p}{2\pi} \dot{B}^A R_f \sin\phi \tag{4.34}$$

At $r = R_1$,

$$\frac{\partial}{\partial r} V = (a - \frac{b}{R_1^2}) \sin\phi = 0 \tag{4.35}$$

These two equations give

$$a = \frac{L_p}{2\pi}\dot{B}\frac{R_f^2}{(R_1^2+R_f^2)} \tag{4.36}$$

$$b = \frac{L_p}{2\pi}\dot{B}\frac{(R_1R_f)^2}{(R_1^2+R_f^2)} \tag{4.37}$$

Therefore the solution for the electric potential for $R_f \leq r \leq R_1$ is

$$V(r,\phi) = \frac{L_p}{2\pi}\dot{B}\frac{R_f^2}{R_f^2+R_1^2}(r+\frac{R_1^2}{r}\sin\phi) \tag{4.38}$$

For the inner core, $0 \leq r \leq R_0$, V has the boundary condition that it is non-singular in the middle. Therefore,

$$V(r \leq R_0,\phi) = \frac{L_p}{2\pi}\dot{B}r\sin\phi \tag{4.39}$$

which is the same solution as that in the multifilamentary region.

To summarize, the solution for the electric potential in all three regions is

$$V(r,\phi) = \begin{cases} \frac{L_p}{2\pi}\dot{B}r\sin\phi & \text{if } 0 \leq r \leq R_f \\ \frac{L_p}{2\pi}\dot{B}\frac{R_f^2}{R_f^2+R_1^2}(r+\frac{R_1^2}{r}\sin\phi & \text{if } R_f \leq r \leq R_1 \end{cases} \tag{4.40}$$

The fields are then

$$E_r(r,\phi) = -\frac{\partial}{\partial r}V = \begin{cases} -\frac{L_p}{2\pi}\dot{B}\sin\phi & \text{if } 0 \leq r \leq R_f \\ -\frac{L_p}{2\pi}\dot{B}\frac{R_f^2}{R_f^2+R_1^2}(1-\frac{R_1^2}{r^2})\sin\phi & \text{if } R_f \leq r \leq R_1 \end{cases} \tag{4.41}$$

$$E_\phi(r,\phi) = -\frac{1}{r}\frac{\partial}{\partial\phi}\Phi = \begin{cases} -\frac{L_p}{2\pi}\dot{B}\cos\phi & \text{if } 0 \leq r \leq R_f \\ -\frac{L_p}{2\pi}\dot{B}\frac{R_f^2}{R_f^2+R_1^2}(1+\frac{R_1^2}{r^2})\cos\phi & \text{if } R_f \leq r \leq R_1 \end{cases} \tag{4.42}$$

E_z is neglected in this set of derivations. It will come into play when "eddy current

losses" are considered.

Power loss per unit volume is defined as (remember that E_z is neglected),

$$p_d \approx \frac{1}{A_{cs}} \int_0^{2\pi} \left\{ \int_0^{R_0} \sigma_{cu} + \int_{R_0}^{R_f} \sigma_\perp + \int_{R_f}^{R_1} \sigma_{cu} \right\} (E_r^2 + E_\phi^2) r \, dr \, d\phi \tag{4.43}$$

where A_{cs} is the cross-sectional area. After substituting in (4.41) and (4.42) into the above equation, we obtain for the total coupling power loss per unit volume

$$p_d = \dot{B}^2 \left(\frac{L_p}{2\pi}\right)^2 \left(\frac{R_f}{R_1}\right)^2 [k\sigma_\perp + (l+m)\sigma_{cu}] \tag{4.44}$$

where

$$k = \frac{R_f^2 - R_0^2}{R_f^2} \tag{4.45}$$

$$l = \frac{R_0^2}{R_f^2} \tag{4.46}$$

$$m = \frac{R_1^2 - R_f^2}{R_1^2 + R_f^2} \tag{4.47}$$

(4.44) has one less 'coupling' term which has been neglected from ignoring E_z. This is the normal eddy current that is induced in the copper regions, independent of the voltages induced in the MFZ.

Ito gives the expression for eddy current loss in the *outer* sheath as

$$p_e = \frac{\dot{B}^2}{4} \sigma_{cu} \left(\frac{R_1^4 - R_f^4}{R_1^2} \right) \tag{4.48}$$

He has not, however, mentioned the eddy current loss in the core. To solve the complete problem, once again, we can make the assumption that one can take the solution in the multifilamentary region and use it as a boundary condition for the

copper core region. Here, we have to refer back to chapter 3 for the solutions to $E_{||}$ and Φ to extract the expression for E_z in the multifilamentary region.

$$E_z(r,\phi) = E_{||}(r,\phi) + \frac{2\pi}{L_p}\frac{\partial}{\partial\phi}\Phi(r,\phi) \tag{4.49}$$

(3.71) and (3.72) give

$$E_{||}(r = R_0) \approx 0 \tag{4.50}$$

$$\Phi(r = R_0, \phi) \approx \frac{L_p}{2\pi}\dot{B}R_0 \sin\phi \tag{4.51}$$

so that the boundary condition on E_z is then

$$E_z(r = R_0, \phi) = \dot{B}R_0 \cos\phi \tag{4.52}$$

E_z inside the copper region should satisfy Laplace's equation

$$\nabla_T^2 E_z = 0 \tag{4.53}$$

The solution

$$E_z = \dot{B}r\cos\phi \tag{4.54}$$

is a solution that satisfies the equation and the boundary condition.

Therefore, the additional eddy current loss in the core is simply

$$p_{e,core} = \frac{\dot{B}^2}{4}\frac{R_0^4}{R_1^2}\sigma_{cu} \tag{4.55}$$

Therefore, the total coupling/eddy current loss is

$$p_c = p_d + p_e = \frac{\dot{B}^2}{R_1^2}\left[\left(\frac{L_p}{2\pi}\right)^2 R_f^2(k\sigma_\perp + (l+m)\sigma_{cu}) + \frac{\sigma_{cu}}{4}(R_1^4 - R_f^4 + R_0^4)\right] \quad (4.56)$$

If we define $p_{tot} = \frac{2\dot{B}}{\mu_0}\tau_{eff}$, an effective time constant extracted from the above equation gives

$$\tau_{eff} = \frac{\mu_0}{2R_1^2}\left[\left(\frac{L_p}{2\pi}\right)^2 R_f^2(k\sigma_\perp + (l+m)\sigma_{cu}) + \frac{\sigma_{cu}}{4}(R_1^4 - R_f^4 + R_0^4)\right] \quad (4.57)$$

The total coupling energy loss Q_c is dependent on the shape of the excitation field. Here we will examine the effect of a ripple field on the total coupling loss. Loss per unit volume per cycle is defined as

$$Q_c = \int_0^T p_c dt \quad (4.58)$$

where $T = 2\pi/\omega$. The internal magnetic field is approximately [11]

$$B_i = B^A - \dot{B}_i\tau_{eff} \quad (4.59)$$

For an excitation field of $B^A = \frac{1}{2}B_m e^{i\omega t}$, the solution for the above time-differential equation yields

$$B_i = \frac{B_m}{2(\omega^2\tau_{eff}^2 + 1)^{\frac{1}{2}}} e^{i\omega t - \delta} \quad (4.60)$$

where δ is a phase lag satisfying $\tan\delta = \omega\tau_{eff}$. The loss per unit volume per cycle is

$$\begin{aligned} Q_c &= \int_0^{\frac{2\pi}{\omega}} \frac{2\dot{B}_i^2}{\mu_0}\tau_{eff}\, dt \\ &= \frac{B_m^2}{2\mu_0}\frac{\pi\omega\tau_{eff}}{(\omega^2\tau_{eff}^2 + 1)} \end{aligned} \quad (4.61)$$

Code results

Due to the multiple layers in a conductor, the boundaries between layers must be treated with care. Both $\sigma_\perp$ and $\sigma_{||}$ in the governing equations are discontinuous across the boundaries. $E_{||}$ is also discontinuous since α is non-zero only in the multifilamentary region. Φ however is continuous. In order to circumvent the numerical difficulties of a discontinuous solution for $E_{||}$, we can still define α as if it were twisted such that it is continuous across boundaries and assign appropriate conductivities to the isotropic regions. Since the inner and outer regions are homogeneous, it does not matter what the value of α is as long as it is $<< 1$.

In the copper regions,

$$\begin{aligned} J_z &= \sigma_{||} E_{||} = \sigma_{cu} E_z \\ J_r &= \sigma_\perp E_r = \sigma_{cu} E_r \\ J_\phi &= \sigma_\perp E_\phi + \alpha \sigma_{||} E_{||} = \sigma_{cu} E_\phi \end{aligned} \tag{4.62}$$

If we keep α the same in the copper region as in the MFZ, i.e. α is continuous across the boundary, then we can also keep $E_{||}$ continuous as well. We can replace the conductivities as

$$\begin{aligned} \sigma_{||} &\rightarrow \sigma_{cu} \\ \sigma_\perp &\rightarrow \sigma_{cu} \end{aligned}$$

and according to our ordering system, the current density equations of (4.62) can be achieved.

A dc bias field of 3T with a peak-to-peak ripple amplitude of .3T (10%) is applied at a range of frequencies from 5Hz to 75Hz. J_c is allowed to vary as a function of B^A.

The time constant for this wire is about $\tau = 1.34$msec. and the results from Ito's expression's and the code are plotted against f in fig. 4-7.

The graph shows that the discrepancy between the two methods grow with increasing frequency. This trend is actually consistent with experimental results found in Kwasnitza [32]. A possible explanation for the overestimation of the loss from eqn. 4.61 can be attributed to the fact that there is a combination of high coupling loss and thicker penetration of dipole currents at these frequencies which the analytical model does not treat well. In fact, high levels of saturation tend to decrese losses - both hysteresis and coupling losses. Experimental data tend to fit (4.61) at very high frequencies ($\omega\tau >> 1$) because coupling losses are so low that errors are less pronounced.

4.2.4 Case 4: Field ramp with transport current

The interaction between transport current and dipole currents induced by an externally changing field has been of great interest and debate in the ac loss community. Turck [25] claims that time-varying external fields tends to even out transport current. Sumiyoshi [22] claims the same 'uniforming' effect but on a much longer time scale than previously expected. Our formulation agrees with Sumiyoshi's prediction.

Because the transport current does not have to cross the copper matrix, the time constant for the rate of diffusion of transport current is dictated by $\sigma_{||}$ and not $\sigma_{\perp}$ as with dipole currents. Although $\sigma_{||}$ is highly dependent on $\dot{B}$, it is nevertheless a large value, one much bigger than $\sigma_{\perp}$.

The parallel time constant is (as given in Sumiyoshi),

$$\tau_{||} = \tau_{||,0}(1 - \beta^2) \tag{4.63}$$

where

$$\tau_{||,0} = \mu_0 \frac{2}{k_1^2} \frac{\lambda j_c}{|\dot{B}| r_f} R_f^2 \tag{4.64}$$

k_1 is the first zero in the first order Bessel function ($J_1(k_1) = 0$) and

$$\beta = \tau_\perp |\dot{B}| H_{pw} \tag{4.65}$$

$$\tau_\perp = \frac{\mu_0}{2} \left(\frac{L_p}{2\pi} \right)^2 \sigma_\perp \tag{4.66}$$

$$H_{pw} = \frac{2}{\pi} \lambda j_c R_f \tag{4.67}$$

H_{pw} is the amount of transverse field needed to penetrate the wire to its center. Basically β is the thickness of the saturation region occupied by the dipole current.

The parallel time constant in chapter 3 is similar to eqn. 4.63. The major difference is in the $(1-\beta^2)$ term which takes into account the reduced radius due to penetration of dipole currents. The β^2 factor is actually quite small. For instance, given $\dot{B}^A = 10\text{T/sec}$, $\tau_\perp = 1\text{msec}$, $\lambda j_c = 6.5\times10^8 \text{A/m}^2$, and $R_f = .5\text{mm}$, we have $\beta^2 = .043$. Even at a high field rate of 10T/sec., the reduction in radius is still small.

The geometrical factor between the present derivation and Sumiyoshi's is slightly different as well. The parallel time constant from 3.78 is

$$\tau_{||} = \frac{\mu_0 \sigma_{||} R_f^2}{8} \tag{4.68}$$

$$\approx \mu_0 \frac{3\pi}{64} \frac{\lambda j_c}{|\dot{B}| r_f} R_f^2 \tag{4.69}$$

Sumiyoshi's geometrical factor is $2/k_1^2 \approx .138$ (where $k_1 \approx 3.8$) and the present geometrical factor is $3\pi/64 \approx .147$. The discrepancy is less than 10%.

The idea is that if, initially, there exists a uniform transport current distribution and a field is ramped, there will be a "bunching up" of transport current as it gets

pushed inward due to the dipole current. This phenomena is due to the fact that the dipole current reaches steady state much faster than the transport current. Thus, before the transport current reaches steady state, it is concentrated in an outer rim of current and diffuses it's way towards a new uniform current density with the time constant $\tau_{||}$. In fact, in fig. 4-8, we do confirm this trend, as produced by the code. The transport current density is plotted against radius (r) and one can see initially, at $t = \tau_c$, there is a layer of concentrated current and at $t = 10 \times \tau_{||}$, the current density has become uniform.

4.3 Conclusion

A computer program designed to solve the nonlinear differential equations in 2 dimensions, r and ϕ, have been put to use to solve AC losses in strands and cable manufactured with only one twist pitch.

Code results were compared against analytic solutions from chapter 3 and derivations found in literature. Field profiles were shown for a simple filament matrix geometry. Loss values were plotted for multilayered media, external ramped and ripple fields, and a combination of transport current and ramped field excitation. The ability to solve the problem with a B-field dependence of j_c is a feature of the code one could not find anywhere else. Such results were shown to benchmark as well as to demonstrate the versatility of the code.

The numerical results agree quite well with literature. In fact, for a ripple field excitation, the code is more accurate for mid-frequency range where the expressions found in literature are the least accurate. In addition, for strands with a thick outer copper shell, the code is also more accurate than existing work.

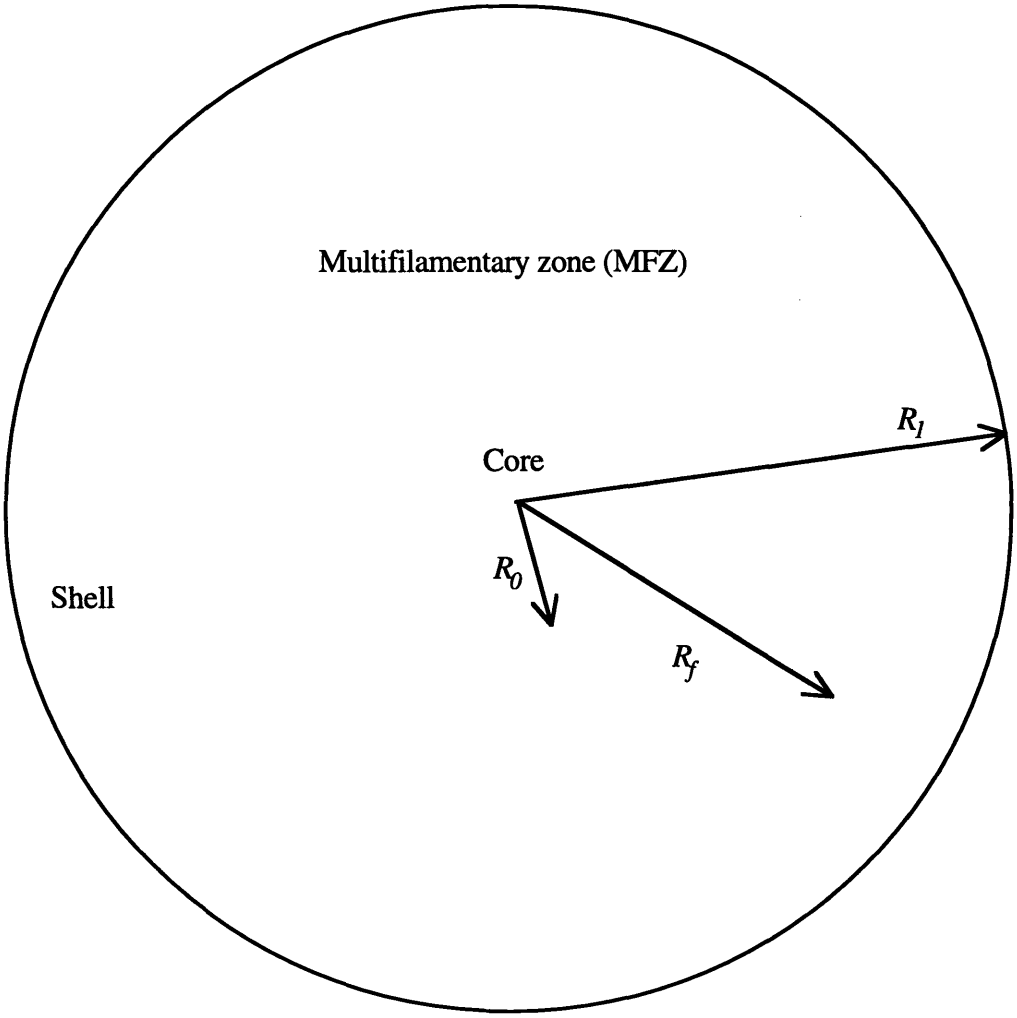

Figure 4-1: Cross-section of multilayer strand

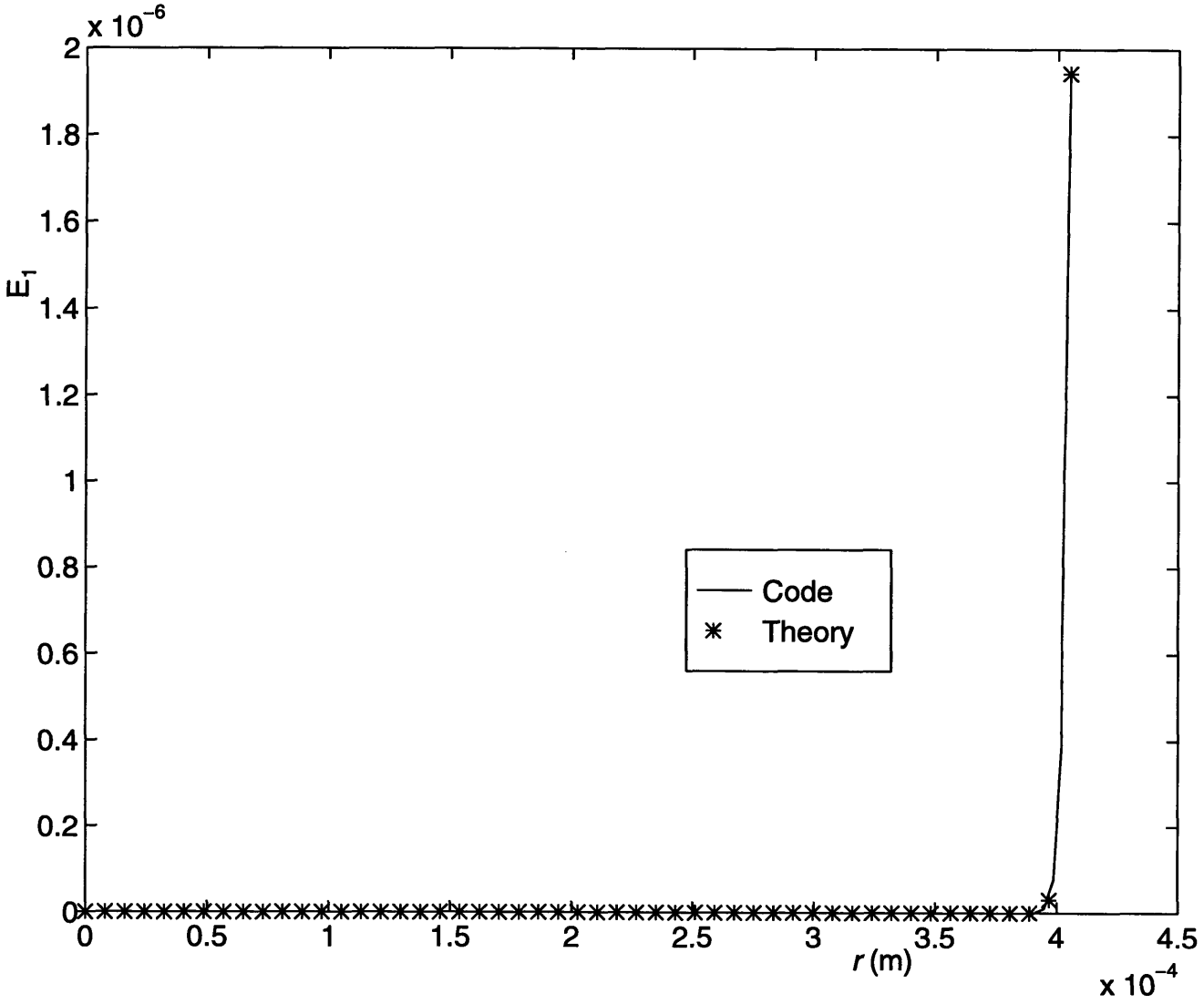

Figure 4-2: Comparison of $E_{||}$ between analytical expressions in section () and numerical results from code for linear $\sigma_{||}$ and $\dot{B}^A$=1 T/sec.

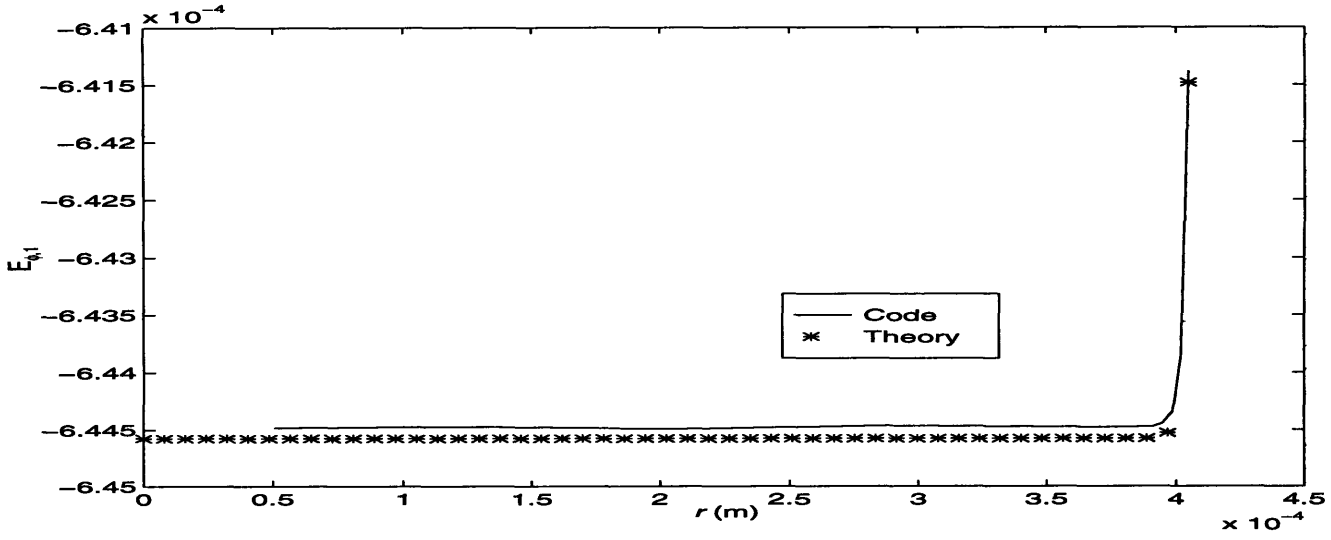

Figure 4-3: Comparison of E_ϕ between analytical expressions in section () and numerical results from code for linear $\sigma_{||}$ and $\dot{B}^A$=1 T/sec.

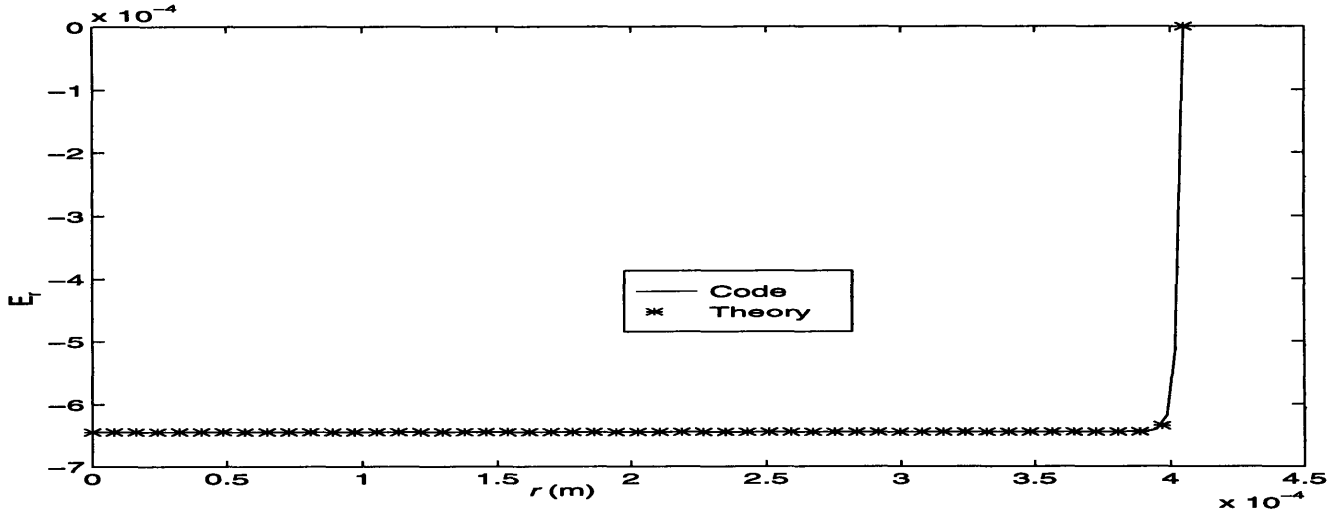

Figure 4-4: Comparison of E_r between analytical expressions in section () and numerical results from code for linear $\sigma_{||}$ and $\dot{B}^A$=1 T/sec.

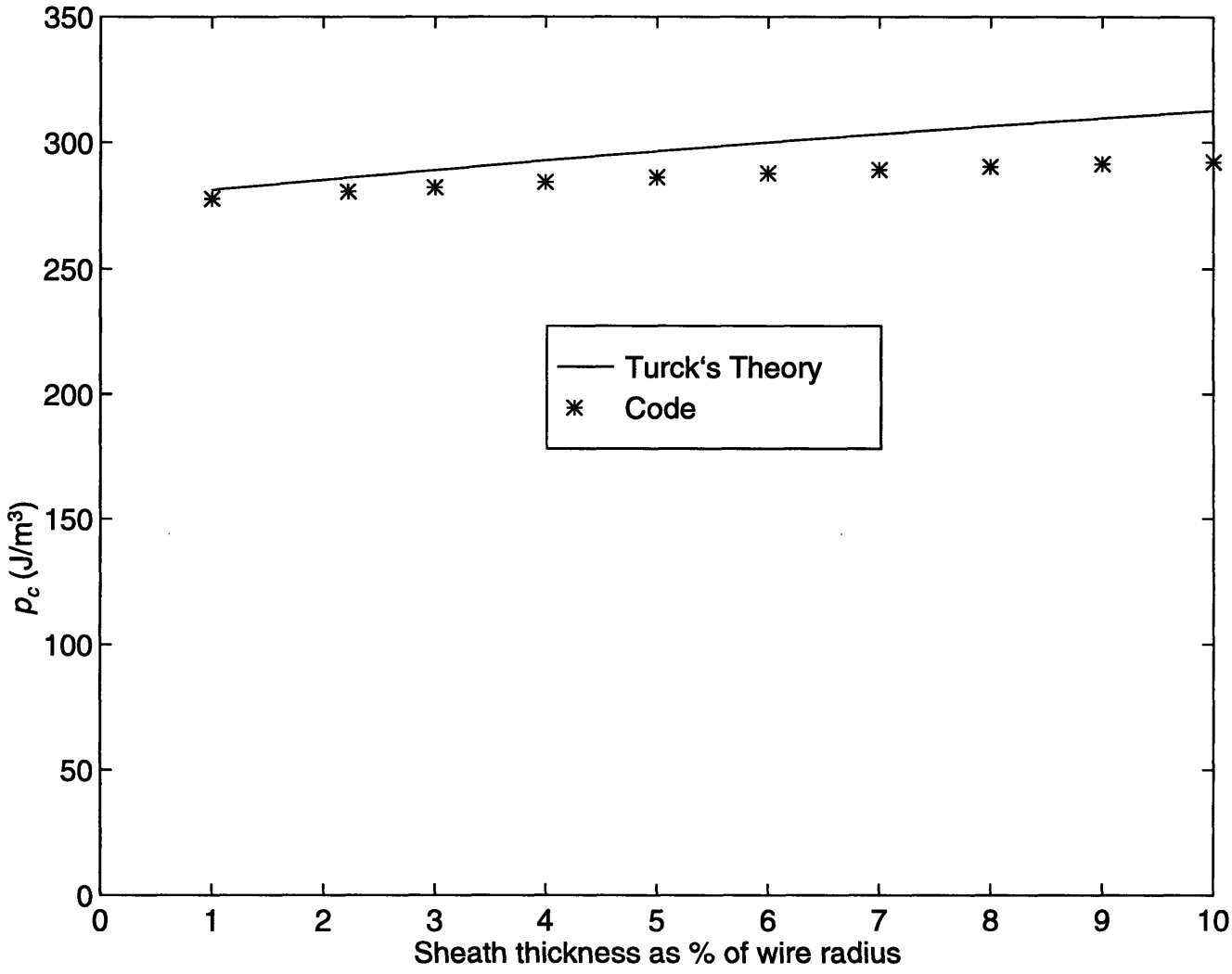

Figure 4-5: Comparison of steady-state power loss of various outer shell thicknesses for $\dot{B}^A$=1 T/sec.

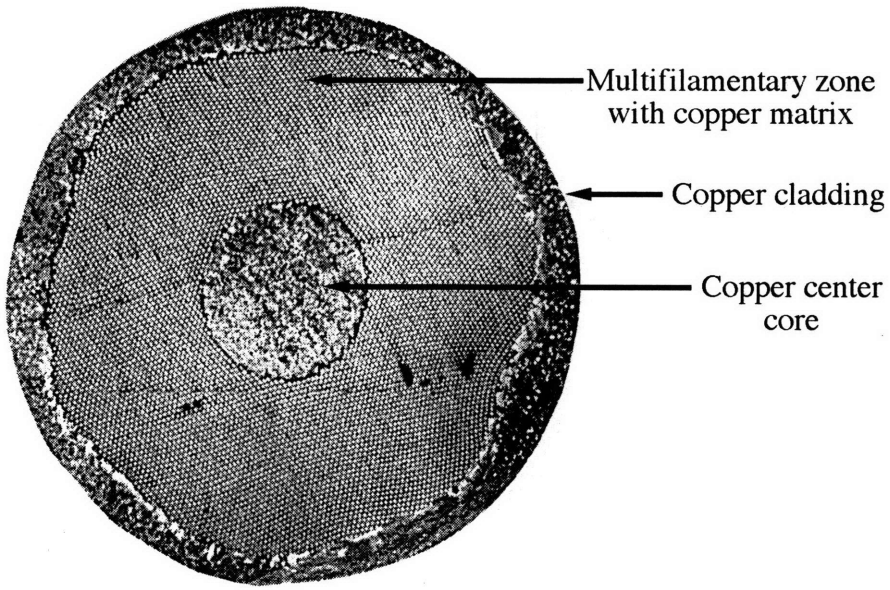

Figure 4-6: Cross-sectional view of SSC NbTi strand

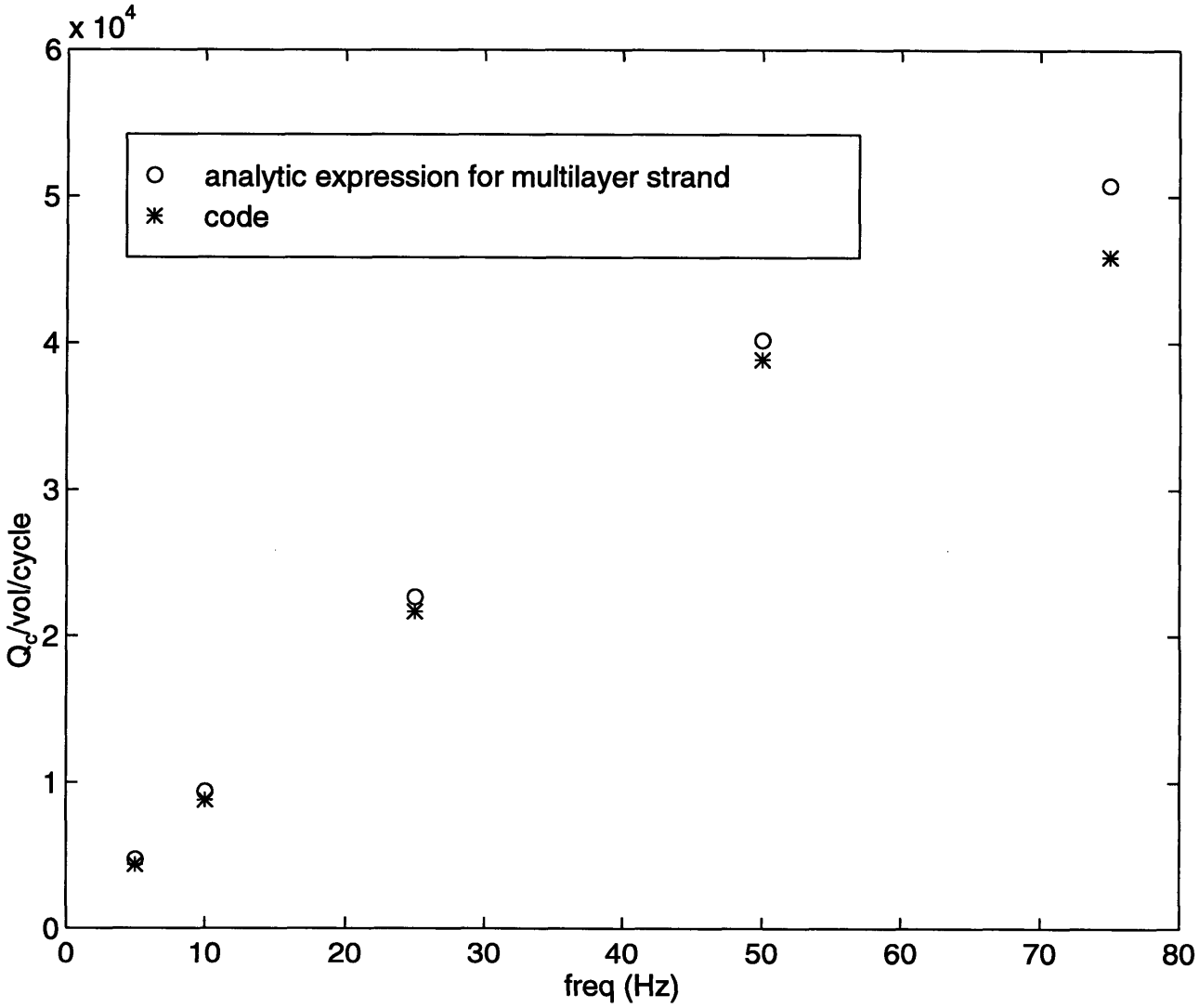

Figure 4-7: Comparison of steady-state power loss of SSC NbTi strand for ripple fields of various frequencies

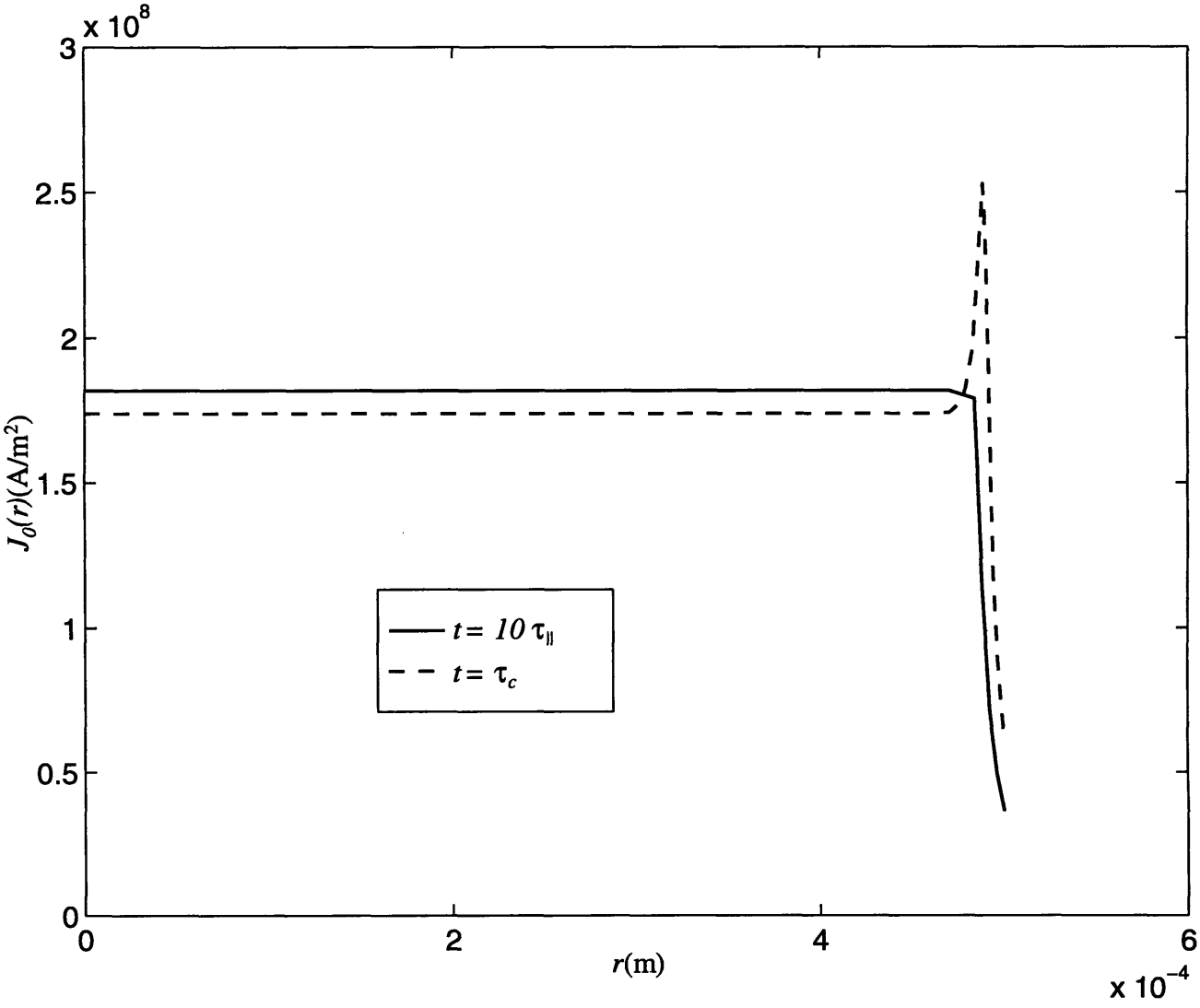

Figure 4-8: Evolution of transport current density in a ramped field.

Chapter 5

3D code

This chapter is devoted to the study of AC losses in the ITER cable. To find the behavior of such a large scale cable, one must find an accurate method for finding the trajectory of the strands. A new approach, which takes into account compaction during the manufacturing process, tracks the winding path of individual strands within the cable. Such effort has culminated into what is known as the cable winder code. The strand trajectories derived from the cable winder, although time consuming, is a one-time simulation. They are then applied to the governing set of equations and a new set of equations in 3D emerge.

There is a brief description of the numerics developed for this code. A set of results are shown for ramped fields - field profiles and loss comparison with experimental data. A surprising phenomenon emerges from the code runs - a behavior that may have significant impact on the loss and quench properties of the cable.

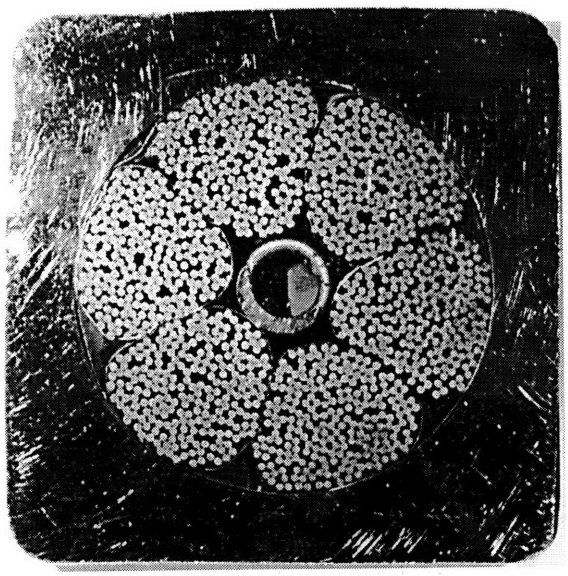

Figure 5-1: Cross-sectional view of ITER cable.

5.1 The Cable Winder

5.1.1 The algorithm

In most cables, the final product is manufactured through several stages. For the proposed ITER CICC, a cable with 5 stages holds 1152 strands. Fig. 5-1 shows the cross-section of the cable. A cable winder program has been developed that traces the path of each of the 1152 strands and can easily be extended to analyze other cable patterns. An outline of the algorithm is described here.

The specifications for this particular geometry is shown in Table 5.1. For the first four stages, the strands/subsections are twisted together with the specified twist pitch of that stage. It is then extruded through a circular die of increasing size with increasing stage. After extrusion at the fourth stage, it is compacted into a leaflet shape. Six of these are then fitted and twisted around the core of the cable to form the final stage. The process is shown schematically in fig. 5-2.

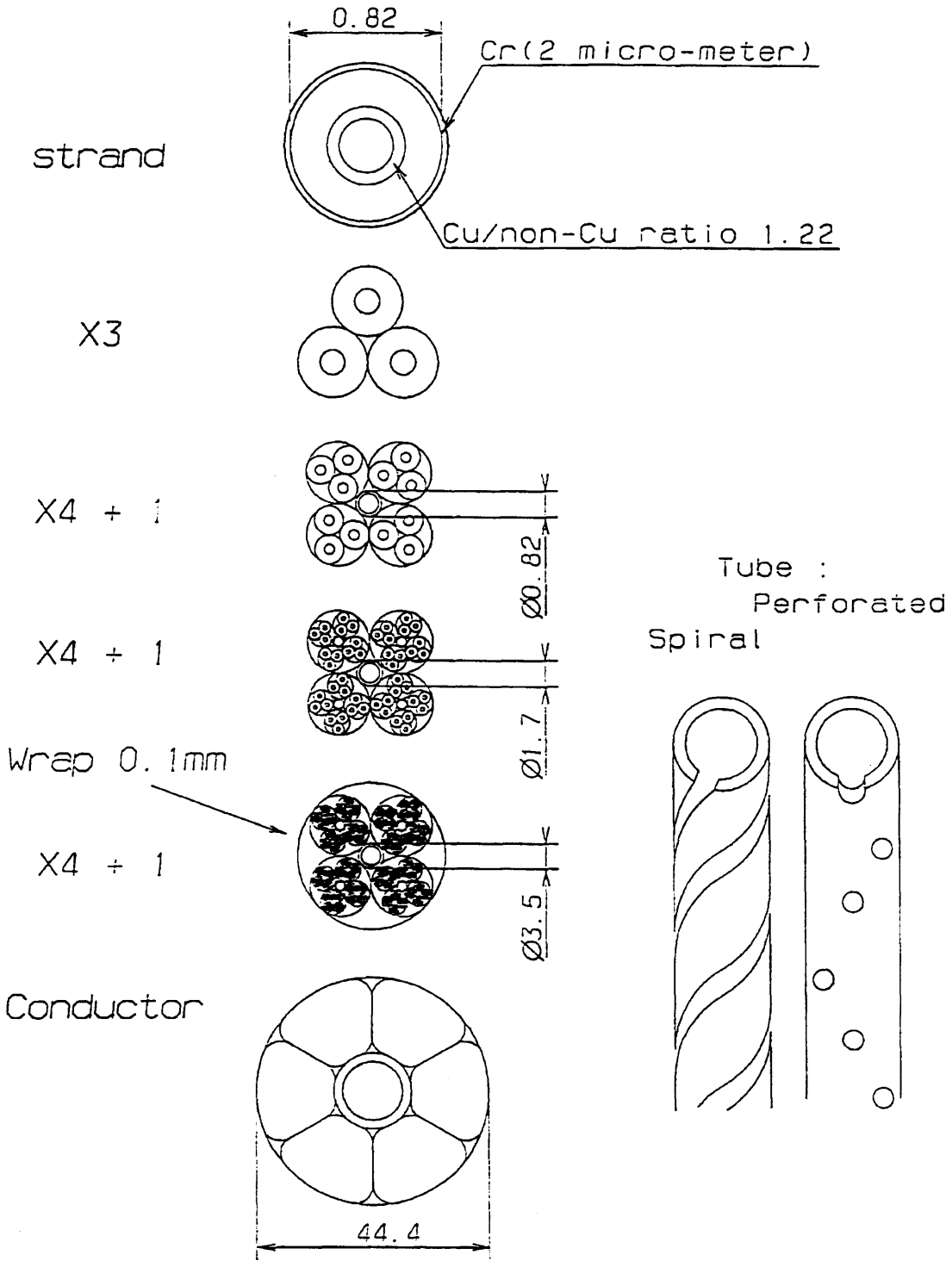

Figure 5-2: Winding process of ITER cable

Stage	Cable	Desired Pitch (L_p)	Estimated Die Size
1	3 x 0.81mm strand	50mm	1.7mm
2	4 x 3 x 1	100mm	3.53mm
3	4 x 4 x 3 x 1	150mm	7.1mm
4	4 x 4 x 4 x 3 x 1	250mm	15.2mm
* At this stage the cable is wrapped and compacted.			
5	6 x 4 x 4 x 4 x 3 x 1	390mm	38.0mm
* This cable will include a center hole 13mm in diameter.			

Table 5.1: Provisional specifications for ITER cable design.

The position of the ith strand for a given cross-section can be written as

$$x_i = \sum_{n=1}^{5} r_n \cos(k_n z - \phi_{in})$$
$$y_i = \sum_{n=1}^{5} r_n \sin(k_n z - \phi_{in}) \tag{5.1}$$

where ϕ_{in} represents the initial position of the ith strand at the nth stage. k_n corresponds to the pitch number of each stage and is equal to $2\pi/L_{pn}$. If r_n, the radius of rotation, is either constant or can be written analytically, our problem is already solved. Unfortunately, the actual geometry is much more complicated due to extrusion through fixed die sizes and compaction at the end of the fourth stage. The winding laws become distorted - the radius of rotation is almost haphazardous because of the compaction. How then do these strands rotate and still keep the leaflet shape?

The solution lies in the concept that strands/substages rotate about a *center of mass/inertia.* Simultaneously, they must obey the winding laws of (5.1). A step-by-step schematic of the algorithm is shown in fig. 5-3. The first step is to take the leaflet shape and find the center of mass. This can easily be done if one assumes a constant

void fraction throughout the cable. The coordinate of the center of mass is

$$x_c = \frac{\int_A x\,dx\,dy}{\int_A dx\,dy}$$
$$y_c = \frac{\int_A y\,dx\,dy}{\int_A dx\,dy} \tag{5.2}$$

Next draw a line from (x_c, y_c) to one of the edges. This will be the reference line. Because each leaflet contains 4 substages, one then draws three other lines such that four equal area subsections are created. These correspond to the four sections that comprise the fourth stage.

Then find the center of mass for each of the four subsections. Draw the reference lines and divide each subsection into four equal area sub-subsections. Repeat this process until you have reached the level of a single strand. The centers of mass found at this stage correspond to the centers of each strand and there should be 4x4x4x3 = 192 strands.

The final step is to move apart any strands which may be overlapping. Since the desired void fraction is quite high (40%), this last step is straightforward. The output of the program is shown in fig. 5-4 with the dividing lines and strands shown to scale.

For the strands in the other 5 leaflets in the cable, one can simply rotate all of the coordinates of the strands $\frac{\pi}{3}$ m times for the mth leaflet (counting the reference one as the 0th leaflet).

$$x_{i+192m} = r_i \cos(\phi_i + \frac{\pi}{3}m)$$
$$y_{i+192m} = r_i \sin(\phi_i + \frac{\pi}{3}m) \tag{5.3}$$

To get the strand distribution somewhere Δz away, one has to use the winding laws. Take the reference lines used to divide up the leaflet and rotate them by an

angle of $\Delta\phi$. $\Delta\phi$ is determined by the amount of rotation affecting each substage. The strands rotate about their own center of mass *and* they also translate due to the rotations of the larger stages. In other words, the total angle of rotation for stage N is

$$\Delta\phi = 2\pi\Delta z \sum_{n=N}^{5} \frac{1}{L_{pn}} \tag{5.4}$$

Then redivide the sections with the new reference lines starting from the fourth stage. Remember that the leaflets themselves also rotate so the new positions for the final stage are

$$\begin{aligned} x_i &= r_{i0}\cos(\phi_{i0} + \frac{2\pi}{L_{p5}}\Delta z) \\ y_i &= r_{i0}\sin(\phi_{i0} + \frac{2\pi}{L_{p5}}\Delta z) \end{aligned} \tag{5.5}$$

where r_{i0} and ϕ_{i0} are the initial coordinates of the strands generated for the fourth stage.

If we follow the path of a particular strand as it travels down the length of the cable, we can calculate the direction coefficients in polar coordinates, $\dot{\rho}_i$ and $\rho\dot{\psi}_i$ where

$$\begin{aligned} \dot{\rho}_i &= \dot{x}_i\cos\phi_i + \dot{y}\sin\phi_i \\ \rho\dot{\psi}_i &= -\dot{x}_i\sin\phi_i + \dot{y}\cos\phi_i \end{aligned} \tag{5.6}$$

and $\dot{x}_i$ and $\dot{y}_i$ are z derivatives of x_i and y_i at z_i. The path of a typical strand is shown in fig. 5-5.

A plot of $\dot{\rho}$ and $\rho\dot{\psi}$ taken at every $\Delta z = 10$mm for an arbitrary strand are shown in fig. 5-6(a) and 5-7(a). It's difficult to extract much information out of these plots but looking at the Fourier transform of them in fig. 5-6(b) and 5-7(b) show distinct harmonics which correspond to the twist pitch of each stage. In fact, the zeroth-

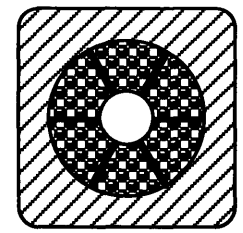

(a)

Stage 5

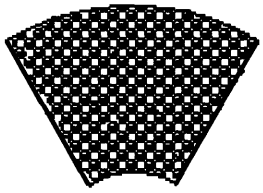

(b)

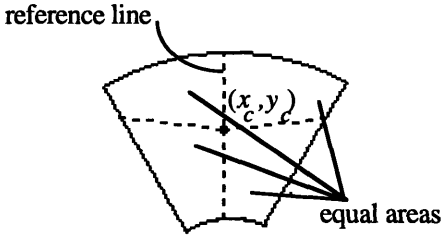

(c)

Stage 4

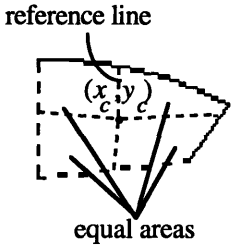

(d)

Stage 3

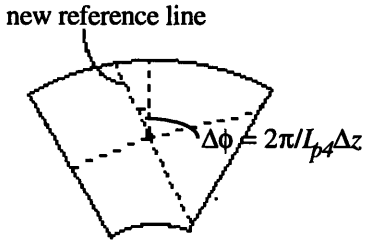

(e)

redivision of the stages for new cross-section at $z+\Delta z$

Figure 5-3: Steps to cable winder algorithm: (a)Cross-section of cable (stage 5). (b)Cross-section of leaflet (stage 4). (c)Center of mass and division of stage 4 into stage 3 subsections. (d)Center of mass and division of stage 3 into stage 2 subsections. (e)Rotation of reference line corresponding to Δz

frequency value of $\rho\dot{\psi}$ should be $\frac{2\pi}{L_{p5}}r_5$ where r_5 is some "effective" radius of rotation of the 5th stage. Here, $\rho\dot{\psi}(f = 0) \approx .25$ which yields an effective radius of rotation of r_5=15.3mm.

So far, we have all of the information in Lagrangian or local coordinates of the strand. However, the field equations are solved in the Eulerian coordinate system of the cable. This means that $\dot{\rho}$ and $\rho\dot{\psi}$ have to be converted from (x_i, y_i, z_i) to (x, y, z). As one traverses axially through the cable, for a fixed (x, y), one would encounter many different strands, all travelling in their own directions. One even encounters empty space; after all, the void fraction is over 40%. If we assume a truly continuous medium, we can assume that $\dot{\rho}$ and $\rho\dot{\psi}$ also behave continuously. Therefore, where there is empty space, the values for $\dot{\rho}$ and $\rho\dot{\psi}$ are interpolated from neighboring strands. At each cross-section (constant z), there is a mesh of points corresponding to the location of the center of each strand with the values of $\dot{\rho}$ and $\rho\dot{\psi}$ associated with each point. The coefficients for locations in between the points are interpolated via a simple linear two-dimensional interpolation method.

5.1.2 Results of cable winder

The results are quite surprising. The direction coefficients behave very well. In fact, as seen from fig. 5-8(b) and 5-9(b), the fourier coefficients of $\dot{\rho}$ are relatively small and $\rho\dot{\psi}$ has a very strong dc component. A radial profile of $\rho\dot{\psi}$ in the next graph shows that it behaves relatively linearly across the radius of the cable. This means that we can write $\rho\dot{\psi}$ simply as

$$\rho\dot{\psi} = \alpha_1 r - \alpha_0 \tag{5.7}$$

For a better fit, $\rho\dot{\psi}$ can be expressed as a polynomial. Fig. 5-10 shows a linear

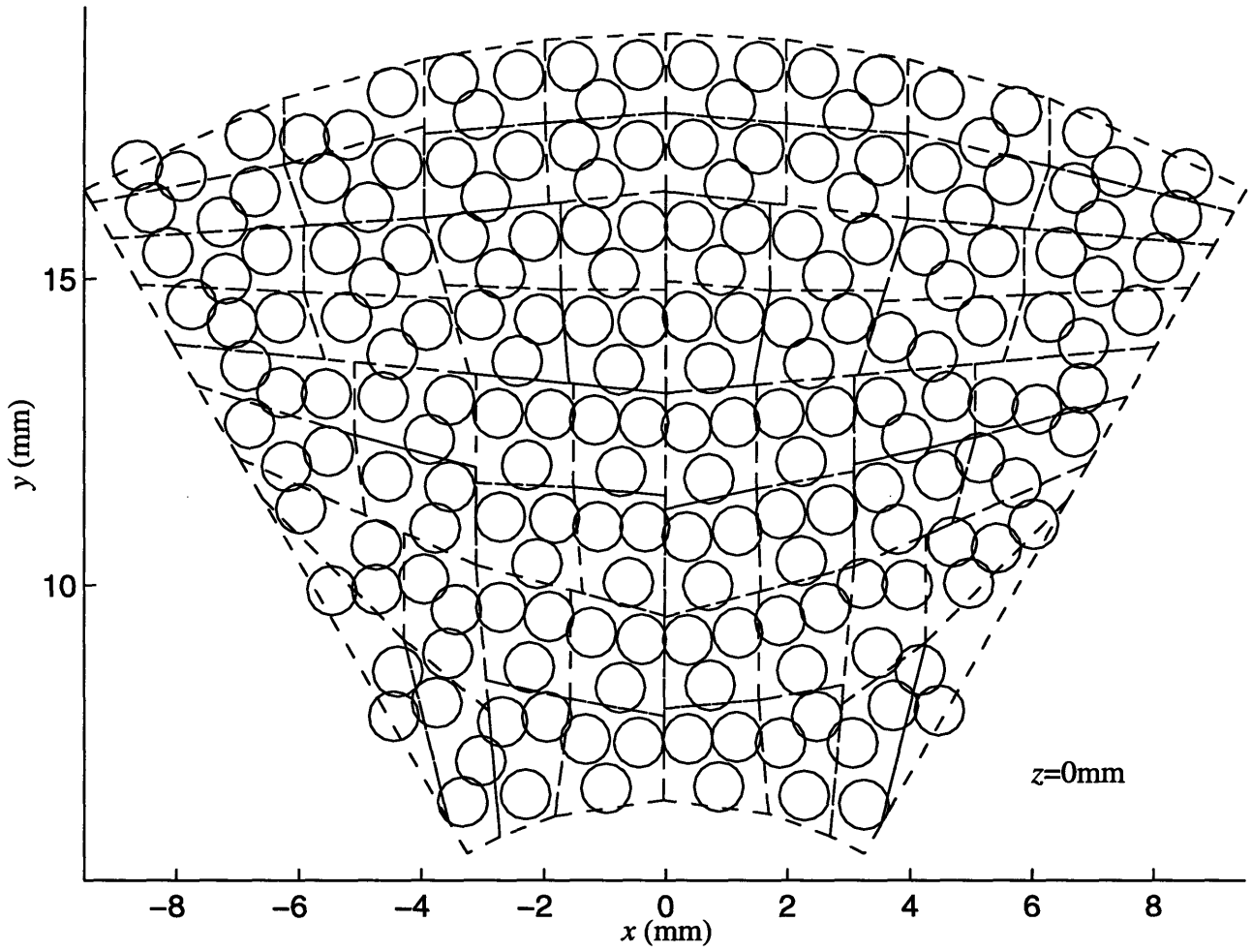

Figure 5-4: Generated strands and borders in a single leaflet.

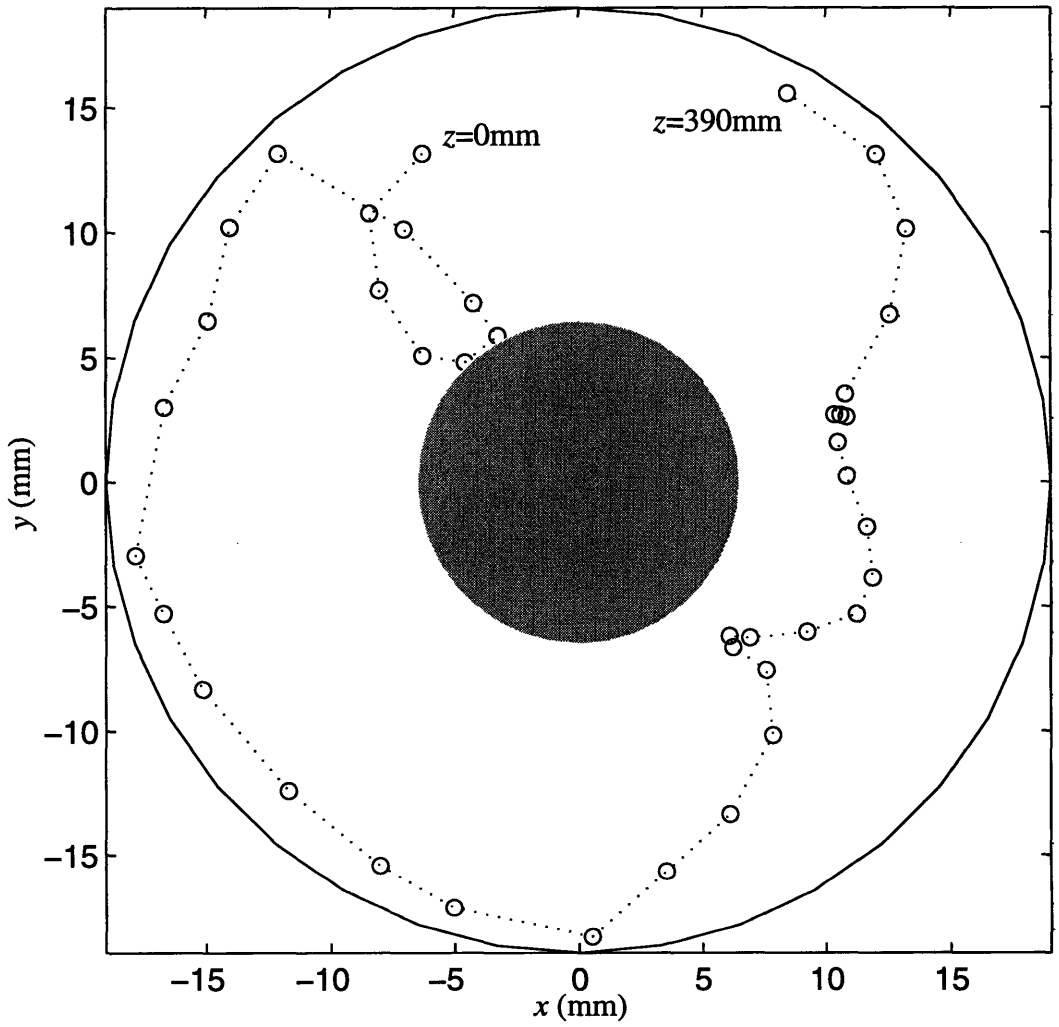

Figure 5-5: Typical strand path as it winds through the cable.

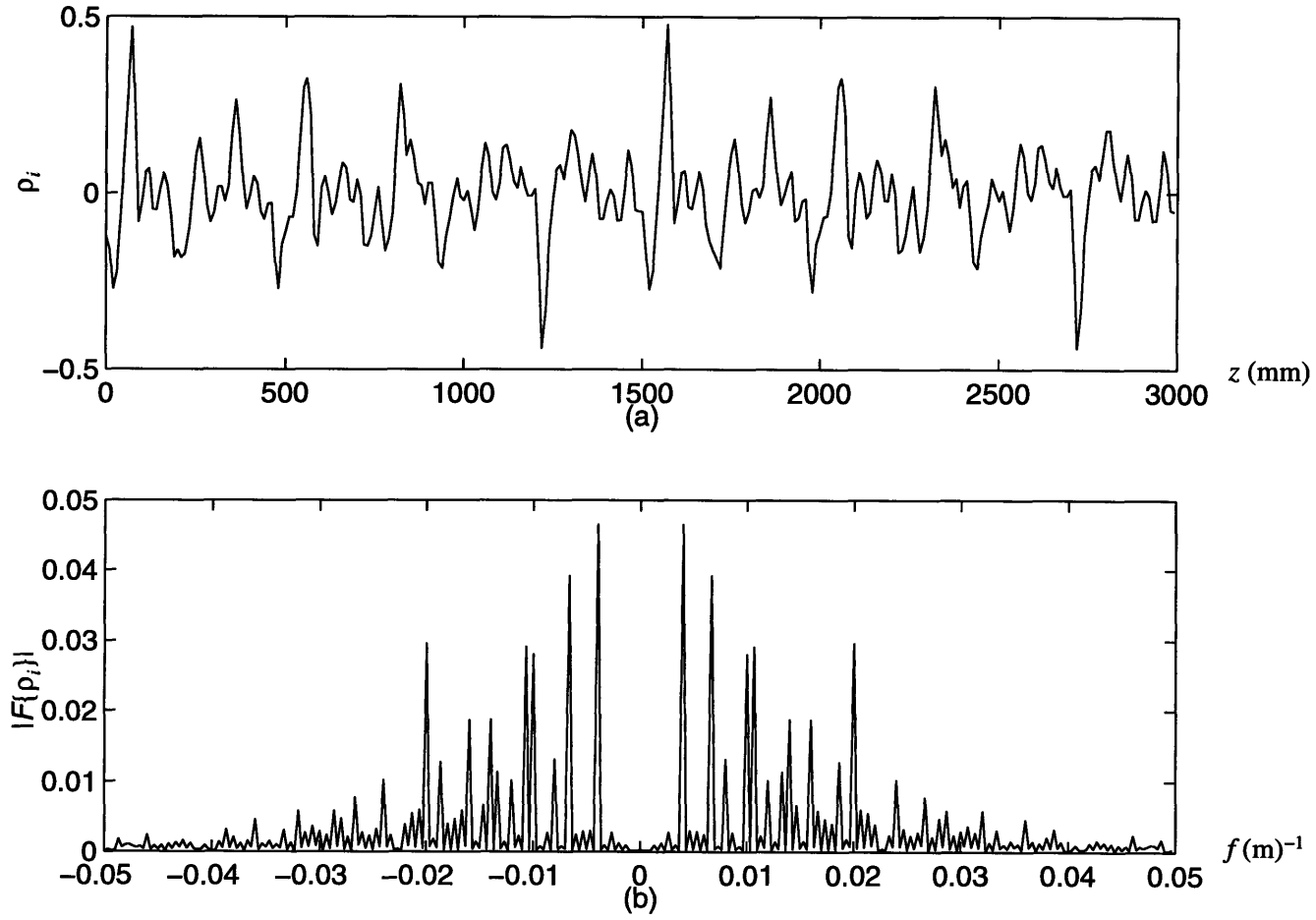

Figure 5-6: (a) radial trajectory $\dot{\rho}$ for ith strand vs. z and (b) the magnitude of it's Fourier transform.

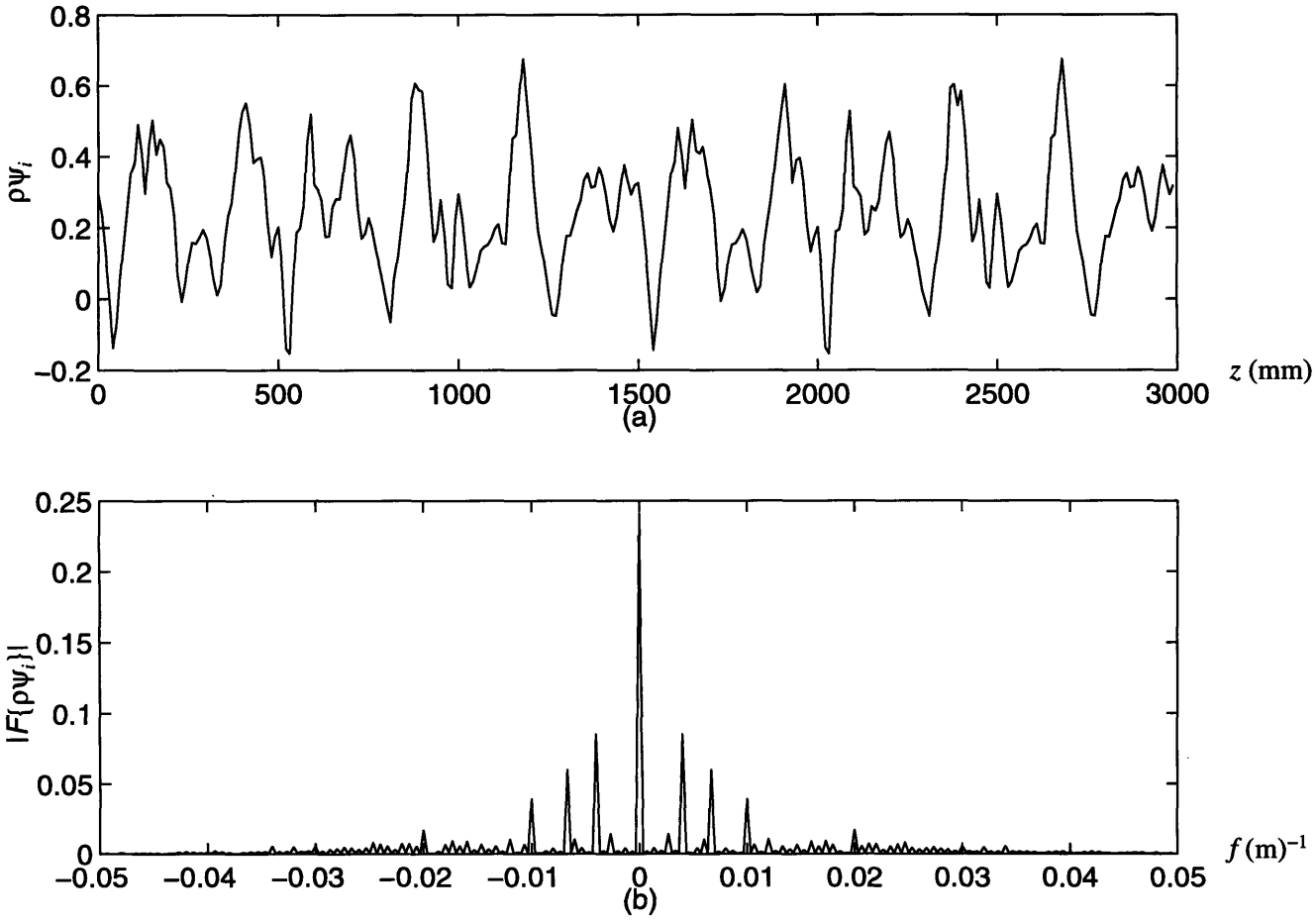

Figure 5-7: (a) azimuthal trajectory $\rho\dot{\psi}$ for ith strand vs. z and (b) the magnitude of it's Fourier transform.

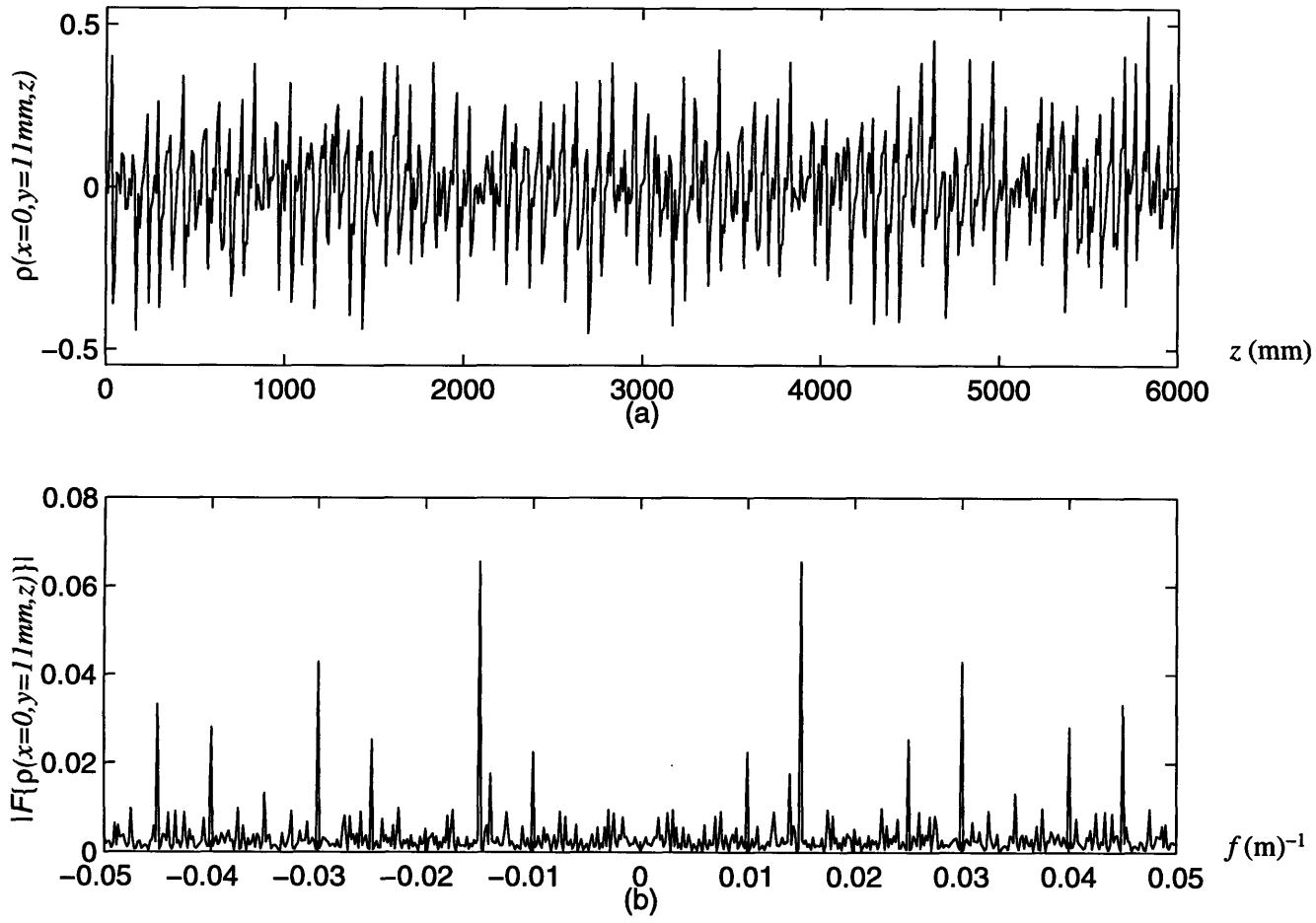

Figure 5-8: (a) radial trajectory at x=0mm,y=11mm plotted vs. z and (b) the magnitude of it's Fourier transform.

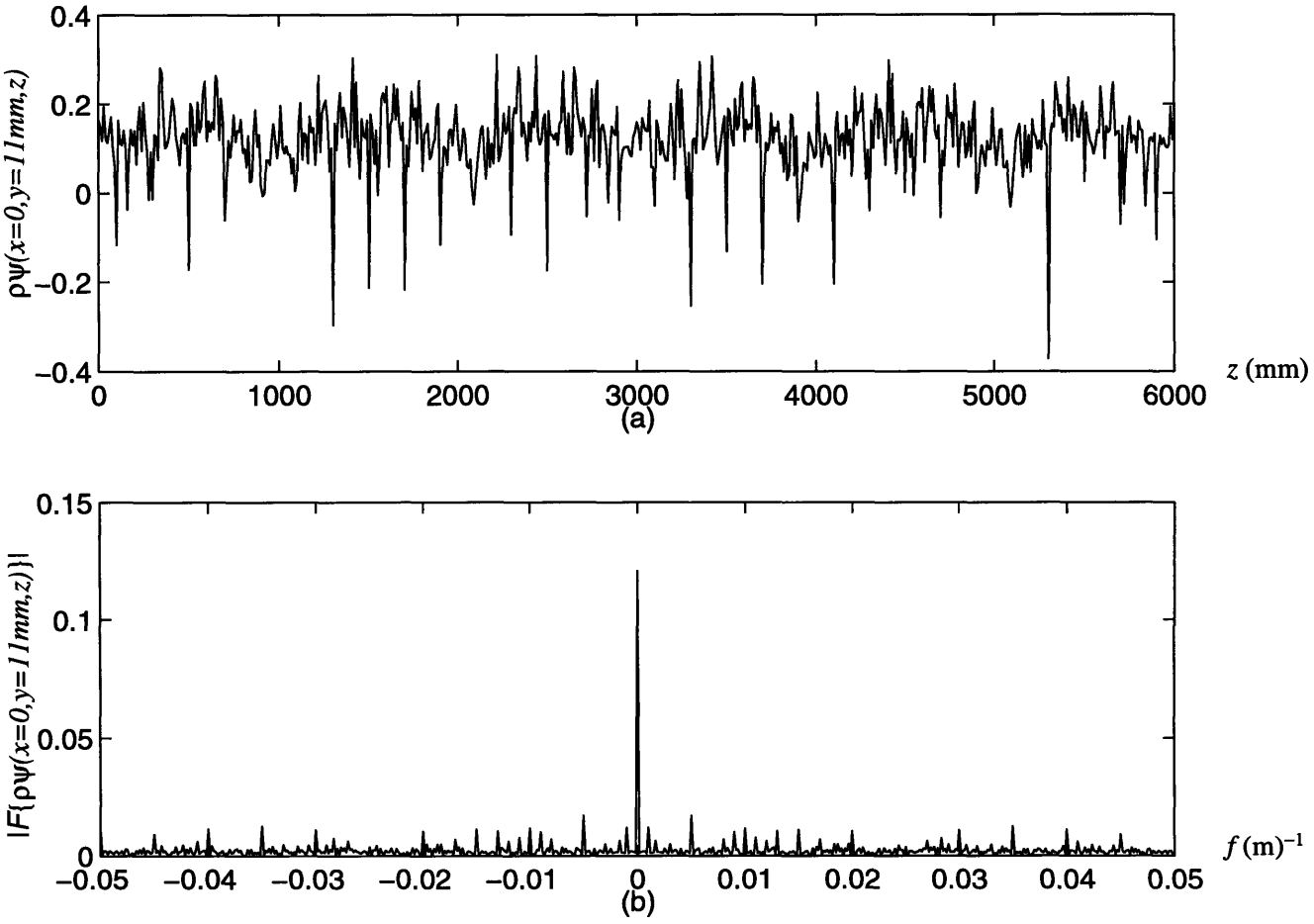

Figure 5-9: (a) azimuthal trajectory at x=0mm,y=11mm plotted vs. z and (b) the magnitude of it's Fourier transform.

and a 5th degree polynomial curvefit. For a linear fit,

$$\begin{aligned} \alpha_1 &= 45 \\ \alpha_0 &= -.373 \end{aligned} \tag{5.8}$$

For a polynomial fit where $\alpha = \alpha_5 r^5 + \alpha_4 r^4 + \alpha_3 r^3 + \alpha_2 r^2 + \alpha_1 r + \alpha_0$, the coefficients are

$$\begin{aligned} \alpha_5 &= 2.75\text{e}10 \\ \alpha_4 &= -1.74\text{e}9 \\ \alpha_3 &= 4.38\text{e}7 \\ \alpha_2 &= -5.50\text{e}5 \\ \alpha_1 &= 3.46\text{e}3 \\ \alpha_0 &= -8.705 \end{aligned} \tag{5.9}$$

For a simple helically wound system such as filaments in a strand, $\alpha_0 = 0$ and $\alpha_1 = 2\pi/L_p$.

Fig. 5-11 shows a horizontal cut-away view of the cable. One is looking *down* on the cable. Notice that the cross-section of the strands become increasingly large as one travels from the outer to the inner radius. This is due to $\rho\dot{\psi}$ having the opposite trend. The angle of rotation is less sharp on the inside, i.e. the strand are "straighter", and so yields a bigger cross-section.

For $\dot{\rho}$, the harmonics mainly correspond to multiples of the twist pitch of the final stage (400mm) divided by 6 which corresponds to the number of leaflets. This is because the strands cannot stray outside each of the leaflets and therefore $\dot{\rho} = 0$ at the perimeter of the leaflets in the same way it is zero at the inner and outer

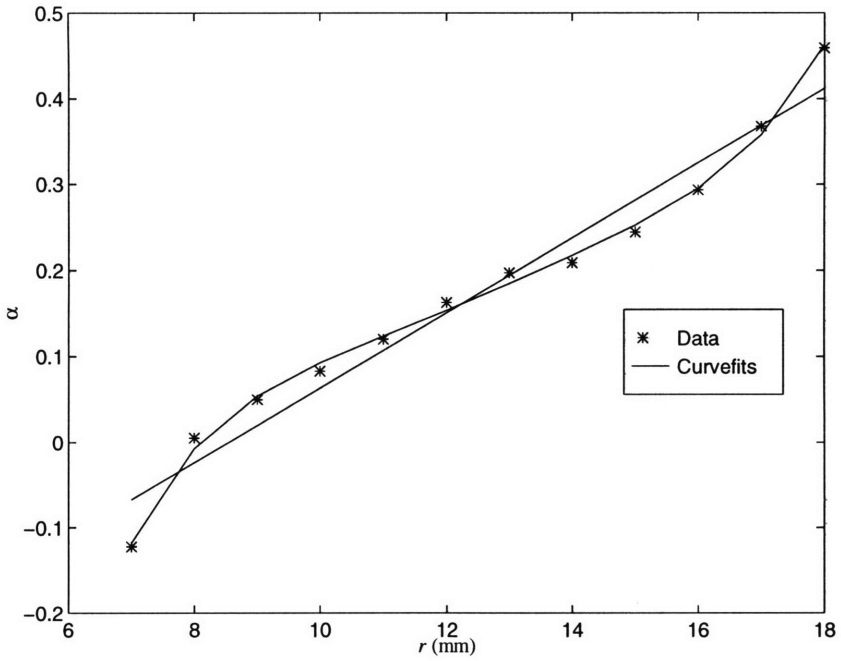

Figure 5-10: Radial profile of $\rho\dot{\psi}$ (α)

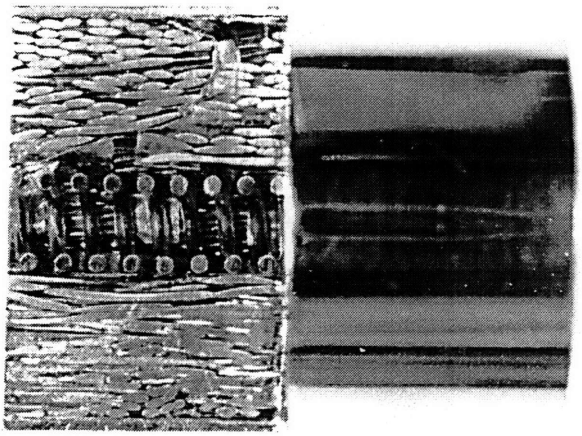

Figure 5-11: Horizontal cross-section of cable showing effect of α

perimeters of the cable itself.

$\dot{\rho}(r, \phi, z)$ can be expressed simply as

$$\dot{\rho} = \sum_n \epsilon_n(r) \sin 6n(\phi - kz) \tag{5.10}$$

ϵ_n is the radial dependence of $\dot{\rho}$ and the first two (largest) harmonics are plotted in fig. 5-12.

5.1.3 Analytic model of $\rho\dot{\psi}$

The cable winder program, albeit versatile and accurate, is not the perfect tool for designing or analyzing a large number of cable configurations. There is a need for an analytical model of the coefficients from a design point of view.

Presently, a fairly accurate closed-form expression for the azimuthal strand trajectory has been derived and verified. The first step is to assume that the last two stages dominate the behavior of the strand paths. Therefore the winding law for a strand can be expressed as

$$x = r_0 \cos\phi_0 + r_1 \cos\phi_1 \tag{5.11}$$

$$y = r_0 \sin\phi_0 + r_1 \sin\phi_1 \tag{5.12}$$

where

$$\phi_0 = k_0 z \tag{5.13}$$

$$\phi_1 = (k_1 + k_0) z \tag{5.14}$$

where k_0 corresponds to the wave number of the last twist pitch and k_1 is the second

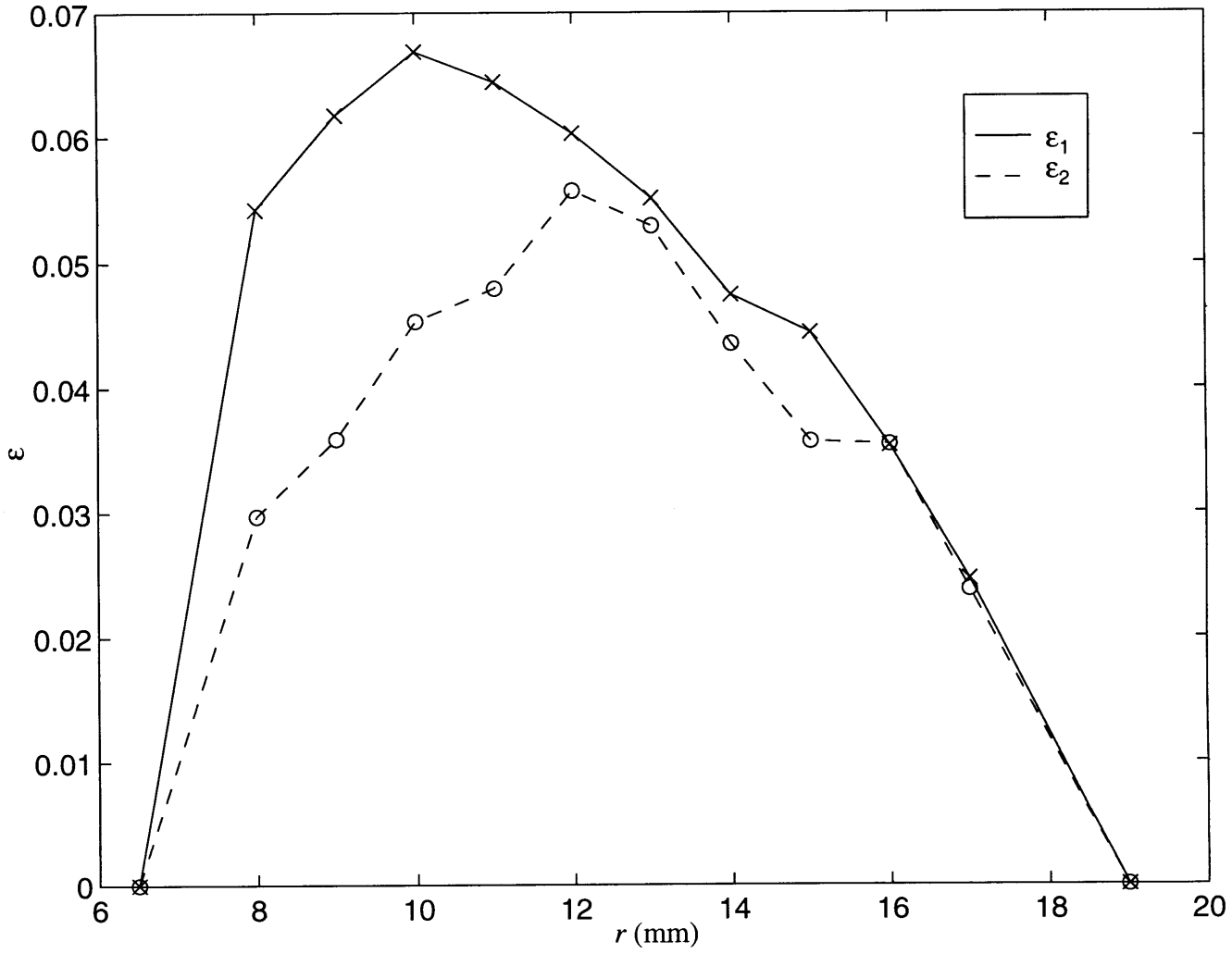

Figure 5-12: Radial profile of harmonics of $\dot{\rho}$

to last twist pitch. The position of a strand is

$$\rho^2 = r_0^2 + r_1^2 + 2r_0 r_1 \cos(\phi_0 - \phi_1) \tag{5.15}$$

$$\tan\psi = \frac{r_0 \sin\phi_0 + r_1 \sin\phi_1}{r_0 \cos\phi_0 + r_1 \cos\phi_1} \tag{5.16}$$

Taking the z derivative of ψ and multiplying by ρ gives

$$\rho\dot{\psi} \equiv \rho\frac{\partial}{\partial z}\psi = \frac{1}{\rho}\left[k_0\rho^2 + k_1 r_1^2 + k_1 r_0 r_1 \cos(\phi_0 - \phi_1)\right] \tag{5.17}$$

Converting to Eulerian coordinates, we make the following substitutions.

$$\rho = r$$

$$\psi = \phi$$

which yields

$$\rho\dot{\psi}(r,\phi,z) = (k_0 + \frac{k_1}{2})r + \frac{k_1}{2}\left(\frac{r_1^2 - r_0^2}{r}\right) \tag{5.18}$$

Figure 5-13 shows a plot of the comparison between (5.18) and the data from the cable winder. The radius of rotations are $r_1 = 3$mm and $r_0 = 13$mm. $k_1 = \frac{2\pi}{.25\text{m}}$ and $k_0 = \frac{2\pi}{.4\text{m}}$. The curvature is somewhat different but otherwise, it is a very good fit.

5.2 Governing equations for the ITER cable

To recap, the coefficients of the parallel directional vector are

$$\dot{\rho} = \sum_n \epsilon_n(r)\sin 6n(\phi - kz) \tag{5.19}$$

$$\rho\dot{\psi} = \alpha(r) \tag{5.20}$$

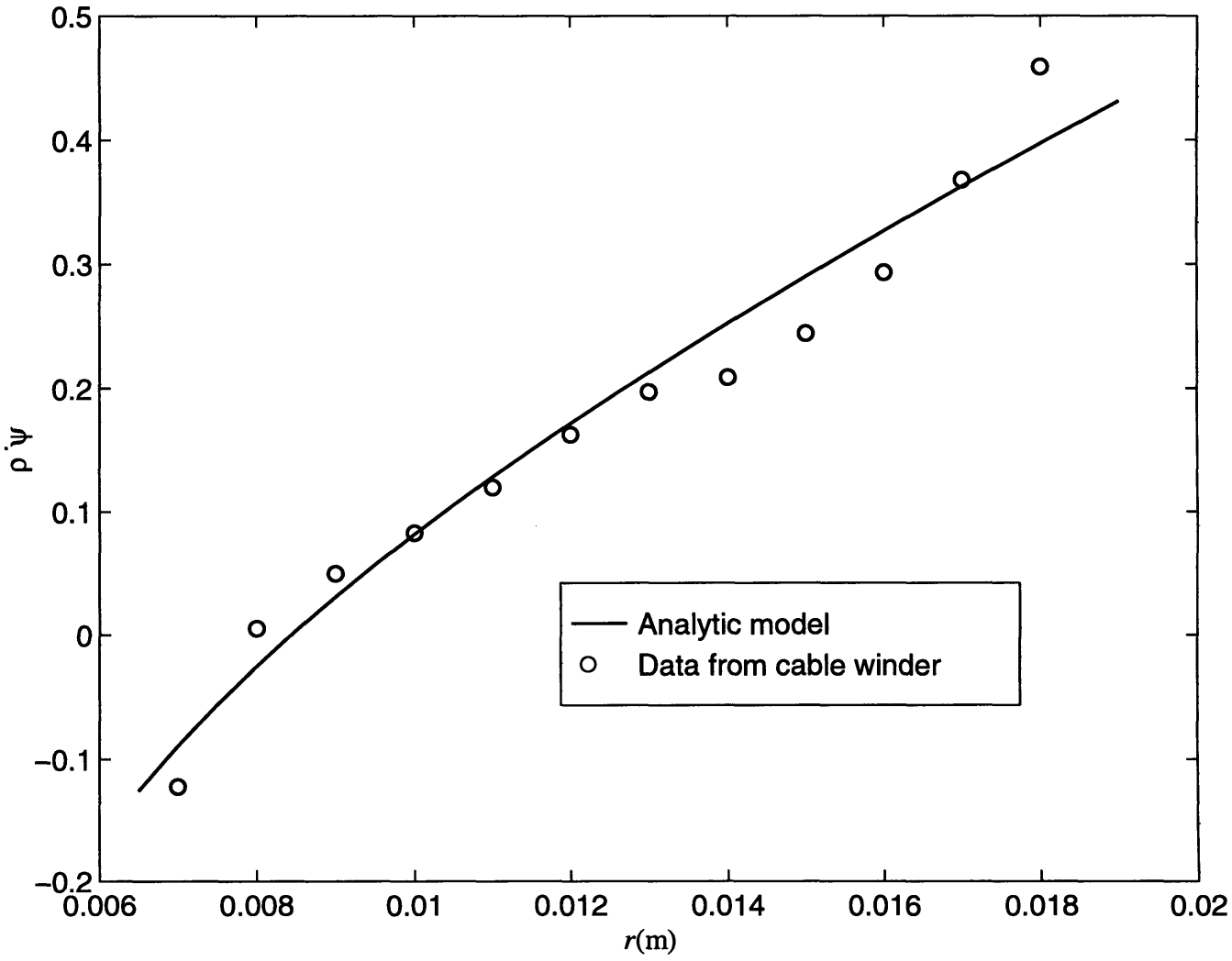

Figure 5-13: Comparison between result from analytic expression and data from cable winder for $\rho\dot{\psi}$.

where $k = 6 \times \frac{2\pi}{.4\text{m}}$ (.4m being the pitch length of the final stage) and the α values can be found in the last section. Introducing the Lagrangian derivative defined as

$$\frac{d}{dz} = \dot{\rho}\frac{\partial}{\partial r} + \rho\dot{\psi}\frac{\partial}{\partial \phi} + \frac{\partial}{\partial z} \tag{5.21}$$

and substituting in (5.20), we can rewrite the governing equations as

$$\nabla_T^2(E_{||} + \frac{d}{dz}\Phi) = \mu_0\frac{\partial}{\partial t}\sigma_{||}E_{||} \tag{5.22}$$

$$\sigma_\perp\nabla_T^2\Phi = \frac{1}{r}\frac{\partial}{\partial r}r(\dot{\rho}\sigma_{||}E_{||}) + \frac{1}{r}\frac{\partial}{\partial \phi}(\alpha\sigma_{||}E_{||}) + \frac{\partial}{\partial z}\sigma_{||}E_{||} \tag{5.23}$$

Introducing the variable σ from chapter 4 such that

$$\frac{\partial}{\partial \bar{x}}\sigma_{||}E_{||} = \sigma\frac{\partial}{\partial \bar{x}}E_{||} \tag{5.24}$$

where

$$\sigma = \sigma_{||} + E_{||}\frac{\partial}{\partial E_{||}}\sigma_{||} \tag{5.25}$$

and substituting it into (5.23) gives

$$\begin{aligned}
\sigma_\perp\nabla_T^2\Phi &= (\dot{\rho}\sigma_{||}E_{||})' + \frac{\dot{\rho}}{r}\sigma_{||}E_{||} + \frac{1}{r}\frac{\partial}{\partial \phi}(\alpha\sigma_{||}E_{||}) + \frac{\partial}{\partial z}\sigma_{||}E_{||} \\
&= \dot{\rho}\sigma E_{||}' + (\dot{\rho}' + \frac{\dot{\rho}}{r})\sigma_{||}E_{||} + \sigma(\frac{\alpha}{r}\frac{\partial}{\partial \phi} + \frac{\partial}{\partial z})E_{||} \\
\sigma_\perp\nabla_T^2\Phi &= \sigma\frac{d}{dz}E_{||} + (\dot{\rho}' + \frac{\dot{\rho}}{r})\sigma_{||}E_{||}
\end{aligned} \tag{5.26}$$

The primes denote partial derivatives in r and are used for ease of notation.

Expanding the second term in equation 5.22 yields

$$\nabla_T^2\frac{d}{dz}\Phi = \frac{d}{dz}\nabla_T^2\Phi + 2(\nabla_T\dot{\rho})\cdot(\nabla_T\Phi') + 2(\nabla_T\frac{\alpha}{r})\cdot(\nabla_T\frac{\partial}{\partial \phi}\Phi) + (\nabla_T^2\dot{\rho})\Phi' + (\nabla_T^2\frac{\alpha}{r})\frac{\partial}{\partial \phi}\Phi$$

$$= (\frac{d}{dz} + 2\dot{\rho}')\nabla_T^2\Phi + \left[\frac{\dot{\rho}}{r^2} - \frac{\dot{\rho}'}{r} + \dot{\rho}'' + \frac{1}{r^2}\frac{\partial^2}{\partial\phi^2}\dot{\rho} + 2\left(\frac{1}{r^2}\frac{\partial}{\partial\phi}\dot{\rho} + (\frac{\alpha}{r})'\right)\frac{\partial}{\partial\phi}\right]\Phi'$$
$$+ \left[\frac{2}{r^2}(\frac{\dot{\rho}}{r} - \dot{\rho}')\frac{\partial^2}{\partial\phi^2} + (\nabla_T^2\frac{\alpha}{r})\frac{\partial}{\partial\phi}\right]\Phi \quad (5.27)$$

Plugging (5.26) into the above equation for $\nabla_T^2\Phi$ yields

$$\nabla_T^2 E_{||} + \frac{1}{\sigma_\perp}(\frac{d}{dz} + 2\dot{\rho}')[\sigma\frac{d}{dz}E_{||} + (\dot{\rho}' + \frac{\dot{\rho}}{r})\sigma_{||}E_{||}]$$
$$+ \left[\frac{\dot{\rho}}{r^2} - \frac{\dot{\rho}'}{r} + \dot{\rho}'' + \frac{1}{r^2}\frac{\partial^2}{\partial\phi^2}\dot{\rho} + 2\left(\frac{1}{r^2}\frac{\partial}{\partial\phi}\dot{\rho} + (\frac{\alpha}{r})'\right)\frac{\partial}{\partial\phi}\right]\Phi' + \left[\frac{2}{r^2}(\frac{\dot{\rho}}{r} - \dot{\rho}')\frac{\partial^2}{\partial\phi^2} + (\nabla_T^2\frac{\alpha}{r})\frac{\partial}{\partial\phi}\right]\Phi$$
$$= \nabla_T^2 E_{||} + \frac{\sigma}{\sigma_\perp}\frac{d^2}{dz^2}E_{||} + \frac{1}{\sigma_\perp}\left[\frac{d}{dz}\sigma + (3\dot{\rho}' + \frac{\dot{\rho}}{r})\sigma\right]\frac{d}{dz}E_{||} + \frac{1}{\sigma_\perp}\left[\frac{d}{dz}(\dot{\rho}' + \frac{\dot{\rho}}{r}) + 2\dot{\rho}'(\dot{\rho}' + \frac{\dot{\rho}}{r})\right]\sigma_{||}E_{||}$$
$$+ \left[\frac{\dot{\rho}}{r^2} - \frac{\dot{\rho}'}{r} + \dot{\rho}'' + \frac{1}{r^2}\frac{\partial^2}{\partial\phi^2}\dot{\rho} + 2\left(\frac{1}{r^2}\frac{\partial}{\partial\phi}\dot{\rho} + (\frac{\alpha}{r})'\right)\frac{\partial}{\partial\phi}\right]\Phi' + \left[\frac{2}{r^2}(\frac{\dot{\rho}}{r} - \dot{\rho}')\frac{\partial^2}{\partial\phi^2} + (\nabla_T^2\frac{\alpha}{r})\frac{\partial}{\partial\phi}\right]\Phi$$
$$= \mu_0\sigma\frac{\partial}{\partial t}E_{||} \quad (5.28)$$

5.3 Numerical strategy

We now need to choose the form of the solutions for $E_{||}$ and Φ. The source gives the ϕ dependence and $\dot{\rho}$ gives both the z and ϕ dependence. From inspection, the following series expansion would make sense.

$$E_{||}(r,\phi,z,t) = \sum_{n=0}^{\infty}\sum_{m=0}^{\infty} E_{mn}(r,t)\cos[6n(\phi - kz) \pm m\phi] \quad (5.29)$$

$$\Phi(r,\phi,z,t) = \sum_{n=0}^{\infty}\sum_{m=0}^{\infty} \Phi_{mn}(r,t)\sin[6n(\phi - kz) \pm m\phi] \quad (5.30)$$

This set of solutions follows the behavior of $\dot{\rho}$ (thus satisfying the differential equations) and would satisfy boundary conditions in an infinitely long cable.

For ease of notation, we introduce a new set of coordinate variables.

$$\phi' = \phi \tag{5.31}$$

$$\xi = 6(\phi - kz) \tag{5.32}$$

After a Jacobian transformation, the partial derivatives are now

$$\frac{\partial}{\partial \phi} = \frac{\partial \phi'}{\partial \phi}\frac{\partial}{\partial \phi'} + \frac{\partial \xi}{\partial \phi}\frac{\partial}{\partial \xi} = \frac{\partial}{\partial \phi'} + 6\frac{\partial}{\partial \xi} \tag{5.33}$$

$$\frac{\partial}{\partial z} = \frac{\partial \phi'}{\partial z}\frac{\partial}{\partial \phi'} + \frac{\partial \xi}{\partial z}\frac{\partial}{\partial \xi} = -6k\frac{\partial}{\partial \xi} \tag{5.34}$$

The series for $\dot{\rho}$, $E_{||}$, and Φ in these new variables are

$$\dot{\rho} = \sum_n \epsilon_n(r)\sin n\xi \tag{5.35}$$

$$E_{||}(r,\phi',\xi,t) = \sum_{n=0}^{\infty}\sum_{m=0}^{\infty} E_{mn}(r,t)\cos(n\xi \pm m\phi) \tag{5.36}$$

$$\Phi(r,\phi',\xi,t) = \sum_{n=0}^{\infty}\sum_{m=0}^{\infty} \Phi_{mn}(r,t)\sin(n\xi \pm m\phi) \tag{5.37}$$

This change of variable actually saves computation time as well because the harmonics are no longer multiples of 6. This cuts the number of sample points for the FFT operations by 6(as will be described later).

Making the variable transformation on the most common derivative term yields

$$\frac{\alpha}{r}\frac{\partial}{\partial \phi} + \frac{\partial}{\partial z} = 6\frac{\alpha_e}{r}\frac{\partial}{\partial \xi} + \frac{\alpha}{r}\frac{\partial}{\partial \phi'} \tag{5.38}$$

where $\alpha_e = \alpha - kr$.

The singularity in the ξ and ϕ' derivatives of σ can be treated similarly to section 4.1. Here the Fourier decomposition involves double integrals - one in ϕ' and one

in ξ. The problematic term in (5.28) is

$$(\frac{d}{dz}\sigma)(\frac{d}{dz}E_{||}) \tag{5.39}$$

because of the derivative of σ. Again, as in section 4.1, we can try to circumvent this problem by absorbing the derivatives into the Fourier integrals.

We can write the cosine Fourier integrals in more general terms.

$$\mathcal{F}\{(\frac{d}{dz}\sigma)(\frac{d}{dz}E_{||})\} = \int_0^{2\pi}\int_0^{2\pi}(\frac{d}{dz}\sigma)(\frac{d}{dz}E_{||})f(\phi',\xi)d\phi' d\xi \tag{5.40}$$

where $f(\phi',\xi) = \cos(p\phi' + q\xi)$. Now,

$$\begin{aligned}
\iint(\frac{d}{dz}\sigma)(\frac{d}{dz}E_{||})f(\phi',\xi)\,d\phi'\,d\xi &= \iint f\dot{\rho}\sigma'\frac{d}{dz}E_{||}\,d\phi'\,d\xi + \frac{1}{r}\iint f(6\alpha_e\frac{\partial}{\partial\xi}\sigma + \alpha\frac{\partial}{\partial\phi'}\sigma)\frac{d}{dz}E_{||}\,d\phi'\,d\xi \\
&= \mathcal{F}\{\dot{\rho}\sigma'\frac{d}{dz}E_{||}\} \\
&+ \frac{6\alpha_e}{r}\left[\int(f\sigma\frac{d}{dz}E_{||})\Big|_{\xi=0}^{2\pi}d\phi' - \iint\sigma\frac{\partial}{\partial\xi}(f\frac{d}{dz}E_{||})\,d\phi'\,d\xi\right] \\
&+ \frac{\alpha}{r}\left[\int(f\sigma\frac{d}{dz}E_{||})\Big|_{\phi'=0}^{2\pi}d\xi - \iint\sigma\frac{\partial}{\partial\phi'}(f\frac{d}{dz}E_{||})\,d\phi'\,d\xi\right]
\end{aligned} \tag{5.41}$$

$\mathcal{F}$ denotes the Fourier cosine transformation. Unlike the 2D code, the Fourier integrals are evaluated by an FFT routine rather than numerical integration. This is chosen because there are multiple harmonics that need to be extracted and one would have to integrate n times for n number of harmonics.

The above manipulations avoid the problem of having to evaluate the ξ and ϕ' derivatives of σ. However, the first term in the above equation contains an r derivative of σ. This term is computationally costly. As yet, there has been no alternative method in evaluating it. Summarizing, since σ,f, and $E_{||}$ are all periodic functions,

the single integral terms in the above equation simply go to zero so that

$$\begin{aligned}\iint (\frac{d}{dz}\sigma)(\frac{d}{dz}E_{||})f(\phi',\xi)d\phi' d\xi &= \mathcal{F}\{\left[\dot{\rho}\sigma' - \frac{\sigma}{r}(\alpha\frac{\partial}{\partial\phi'} + 6\alpha_e\frac{\partial}{\partial\xi})\right](\frac{d}{dz}E_{||})\} \\ &\quad + \frac{1}{r}(\alpha p + 6\alpha_e q)\Im(\mathcal{F}\{\sigma\frac{d}{dz}E_{||}\}) \qquad (5.42)\end{aligned}$$

$\Im$ stands for the imaginary part of the Fourier transform which corresponds to the sine transformation. A couple of the terms in (5.28) combine to become for the pqth harmonic,

$$\begin{aligned}&\mathcal{F}\{\sigma\frac{d^2}{dz^2}E_{||} + (\frac{d}{dz}\sigma)(\frac{d}{dz}E_{||})\} \\ &= \mathcal{F}\{\dot{\rho}\sigma'(\frac{d}{dz}E_{||})\} + \mathcal{F}\{\dot{\rho}\sigma\frac{d}{dz}E'_{||}\} + \frac{1}{r}(\alpha p + 6\alpha_e q)\Im(\mathcal{F}\{\sigma\frac{d}{dz}E_{||}\}) \qquad (5.43) \\ &= \mathcal{F}\left\{\sigma\left[\dot{\rho}^2 E''_{||} + \dot{\rho}\left(\frac{1}{r}(\alpha\frac{\partial}{\partial\phi'} + 6\alpha_e\frac{\partial}{\partial\xi}) + \dot{\rho}\frac{\sigma'}{\sigma}\right)E'_{||} + \dot{\rho}\frac{\sigma'}{\sigma}\frac{1}{r}(\alpha\frac{\partial}{\partial\phi'} + 6\alpha_e\frac{\partial}{\partial\xi})E_{||}\right]\right\} \\ &\quad + \frac{1}{r}(\alpha p + 6\alpha_e q)\Im(\mathcal{F}\{\sigma\frac{d}{dz}E_{||}\}) \qquad (5.44)\end{aligned}$$

We rewrite the differential equations in (5.28) as

$$\mathrm{L}_2 E''_{||} + \mathrm{L}_1 E'_{||} + \mathrm{L}_0 E_{||} + \mathrm{P}_1\Phi' + \mathrm{P}_0\Phi = \mu_0\sigma\frac{\partial}{\partial t}E_{||} \qquad (5.45)$$

$$\nabla_T^2\Phi = \mathrm{J}_1 E'_{||} + \mathrm{J}_0 E_{||} \qquad (5.46)$$

where the operators are

$$\mathrm{L}_2 = 1 + \frac{\sigma}{\sigma_\perp}\dot{\rho}^2 \qquad (5.47)$$

$$\begin{aligned}\mathcal{F}\{\mathrm{L}_1\} &= \frac{1}{r} + \frac{1}{\sigma_\perp}\mathcal{F}\left\{\left[\sigma\left(\frac{\dot{\rho}}{r}(\alpha\frac{\partial}{\partial\phi'} + 6\alpha_e\frac{\partial}{\partial\xi}) + 4\dot{\rho}\dot{\rho}' + \frac{\dot{\rho}^2}{r}\right) + \dot{\rho}^2\sigma'\right]\right\} \\ &\quad + \frac{1}{\sigma_\perp}\frac{1}{r}(\alpha p + 6\alpha_e q)\Im\left(\mathcal{F}\{\dot{\rho}\sigma\}\right) \qquad (5.48)\end{aligned}$$

$$\begin{aligned}
\mathcal{F}\{\mathrm{L}_0\} &= \frac{1}{r^2}(\frac{\partial}{\partial\phi'}+6\frac{\partial}{\partial\xi})^2+\mathcal{F}\left\{\frac{1}{\sigma_\perp}\left[\sigma_{||}\left(2\dot\rho'^2+\dot\rho\ddot\rho+3\frac{\dot\rho\dot\rho'}{r}-\frac{\dot\rho^2}{r^2}+6\frac{\alpha_e}{r}\frac{\partial}{\partial\xi}(\dot\rho'+\frac{\dot\rho}{r})\right)\right.\right.\\
&\quad\left.\left.+\sigma\left(\dot\rho(\frac{\alpha}{r})'(\frac{\partial}{\partial\phi'}+6\frac{\partial}{\partial\xi})+\frac{1}{r}(3\dot\rho'+\frac{\dot\rho}{r}+\dot\rho\frac{\sigma'}{\sigma})(\alpha\frac{\partial}{\partial\phi'}+6\alpha_e\frac{\partial}{\partial\xi})\right)\right]\right\}\\
&\quad+\frac{1}{\sigma_\perp}\frac{1}{r}(\alpha p+6\alpha_e q)\Im\left(\mathcal{F}\left\{\frac{\sigma}{r}(\alpha\frac{\partial}{\partial\phi'}+6\alpha_e\frac{\partial}{\partial\xi})\right\}\right) \qquad (5.49)\\
\mathrm{P}_1 &= \frac{\dot\rho}{r^2}-\frac{\dot\rho'}{r}+\ddot\rho+\frac{36}{r^2}\frac{\partial^2}{\partial\xi^2}\dot\rho+2(\frac{6}{r^2}\frac{\partial}{\partial\xi}\dot\rho+(\frac{\alpha}{r})')(\frac{\partial}{\partial\phi'}+6\frac{\partial}{\partial\xi}) \qquad (5.50)\\
\mathrm{P}_0 &= \frac{2}{r^2}(\frac{\dot\rho}{r}-\dot\rho')(\frac{\partial}{\partial\phi'}+6\frac{\partial}{\partial\xi})^2+(\nabla_T^2\frac{\alpha}{r})(\frac{\partial}{\partial\phi'}+6\frac{\partial}{\partial\xi}) \qquad (5.51)\\
\mathrm{J}_1 &= \frac{\sigma}{\sigma_\perp}\dot\rho \qquad (5.52)\\
\mathrm{J}_0 &= \frac{1}{\sigma_\perp}[\sigma_{||}(\dot\rho'+\frac{\dot\rho}{r})+\frac{\sigma}{r}(6\alpha_e\frac{\partial}{\partial\xi}+\alpha\frac{\partial}{\partial\phi'})] \qquad (5.53)
\end{aligned}$$

For the constant $\sigma_{||}$ case, the equations become linear and computation time can be drastically reduced if some of the FFT operations are performed *outside* of the ODE solver COLSYS. Since it has been determined that the ratio of $\frac{\sigma_{||}}{\sigma_\perp}$ is very large, any interpolation scheme is out of the question. Rewriting the operators for a constant $\sigma_{||}$, we have, for the pqth equation,

$$\begin{aligned}
\mathcal{F}\{\mathrm{L}_2E_{||}\} &= 1+\frac{\sigma_{||}}{\sigma_\perp}\sum_{m,n}{}''E''_{mn}\mathcal{F}\left\{\dot\rho^2\cos(m\phi'+n\xi)\right\} \qquad (5.54)\\
\mathcal{F}\{\mathrm{L}_1E_{||}\} &= \frac{1}{r}E'_{pq}\\
&\quad+\frac{\sigma_{||}}{\sigma_\perp}\sum_{m,n}{}''E'_{mn}\mathcal{F}\left\{-\frac{\dot\rho}{r}(\alpha m+6\alpha_e n)\sin(m\phi'+n\xi)+(4\dot\rho\dot\rho'+\frac{\dot\rho^2}{r})\cos(m\phi'+n\xi)\right\}\\
&\quad+\frac{\sigma_{||}}{\sigma_\perp}\frac{1}{r}(\alpha p+6\alpha_e q)\sum_{m,n}E'_{mn}\Im\left(\mathcal{F}\{\dot\rho\cos(m\phi'+n\xi)\}\right) \qquad (5.55)\\
\mathcal{F}\{\mathrm{L}_0E_{||}\} &= -\frac{1}{r^2}\left[(p+6q)^2+(\frac{\sigma_{||}}{\sigma_\perp})(\alpha p+6\alpha_e q)^2\right]E_{pq}\\
&\quad-\frac{\sigma_{||}}{\sigma_\perp}\sum_{m,n}{}''E_{mn}\mathcal{F}\left\{\left[\dot\rho\left(\frac{\alpha}{r}\right)'(m+6n)+\frac{1}{r}(3\dot\rho'+\frac{\dot\rho}{r})(\alpha m+6\alpha_e n)\right]\sin(m\phi'+n\xi)\right.
\end{aligned}$$

$$- \left[2\dot{\rho}'^2 + \dot{\rho}\dot{\rho}'' + \frac{3\dot{\rho}\dot{\rho}'}{r} - \frac{\dot{\rho}^2}{r^2} + \frac{6\alpha_e}{r}\frac{\partial}{\partial\xi}(\dot{\rho}' + \frac{\dot{\rho}}{r}) \right] \cos(m\phi' + n\xi) \Big\} \tag{5.56}$$

$$\mathcal{F}\{\mathrm{P}_1\Phi\} = \sum_{m,n}{}'' \Phi'_{mn} \mathcal{F}\left\{ \left(\frac{\dot{\rho}}{r^2} - \frac{\dot{\rho}'}{r} + \dot{\rho}'' + \frac{36}{r^2}\frac{\partial^2}{\partial\xi^2}\dot{\rho} \right) \sin(m\phi' + n\xi) \right.$$
$$\left. +2\left(\frac{6}{r^2}\frac{\partial}{\partial\xi}\dot{\rho} + \left(\frac{\alpha}{r}\right)' \right)(m+6n)\cos(m\phi' + n\xi) \right\} \tag{5.57}$$

$$\mathcal{F}\{\mathrm{P}_0\Phi\} = \sum_{m,n}{}'' \Phi_{mn} \mathcal{F}\left\{ (\nabla_T^2 \frac{\alpha}{r})(m+6n)\cos(m\phi' + n\xi) \right.$$
$$\left. - \frac{2}{r^2}(\frac{\dot{\rho}}{r} - \dot{\rho}')(m+6n)^2 \sin(m\phi' + n\xi) \right\} \tag{5.58}$$

$$\mathcal{F}\{\mathrm{J}_1 E_{||}\} = \frac{\sigma_{||}}{\sigma_\perp} \sum_{m,n}{}'' E'_{mn} \mathcal{F}\{\dot{\rho}\cos(m\phi' + n\xi)\} \tag{5.59}$$

$$\mathcal{F}\{\mathrm{J}_0 E_{||}\} = \frac{\sigma_{||}}{\sigma_\perp} \sum_{m,n}{}'' E_{mn} \mathcal{F}\left\{ (\dot{\rho}' + \frac{\dot{\rho}}{r})\cos(m\phi' + n\xi) - \frac{1}{r}(\alpha m + 6\alpha_e n)\sin(m\phi' + n\xi) \right\} \tag{5.60}$$

An alternative approach, assuming a small number of harmonics for $\dot{\rho}$, would be to isolate the terms that contain ξ and ϕ' and integrate before feeding it into COLSYS. There are only a limited number of combinations.

As an improvement to the present equations, one can add an additional constraint. One can assure that the cable is incompressible, that there are no extra compaction or expansion solely due to an incomplete model of the geometry. This can be done mathematically by enforcing

$$\nabla \cdot \hat{e}_{||} = 0 \tag{5.61}$$

which translates to a relationship between α and $\dot{\rho}$.

$$\frac{6}{r}\frac{\partial}{\partial\xi}\alpha = -\dot{\rho}' - \frac{\dot{\rho}}{r} \tag{5.62}$$

The additional ξ dependent term in α is small. Substituting the above relation into

the governing equations yield a new set of operators as listed below.

$$\mathcal{F}\{\mathrm{L}_1 E_{||}\} = \frac{1}{r}E'_{pq} + \frac{\sigma_{||}}{\sigma_\perp}\sum_{m,n}{}'' E'_{mn}\mathcal{F}\left\{-2\frac{\dot\rho}{r}(\alpha m + 6\alpha_e n)\sin(m\phi' + n\xi) + (3\dot\rho\dot\rho' + \frac{6\alpha_e}{r}\frac{\partial}{\partial\xi}\dot\rho)\cos(m\phi' + n\xi)\right\} \quad (5.63)$$

$$\mathcal{F}\{\mathrm{L}_0 E_{||}\} = -\frac{1}{r^2}\left[(p+6q)^2 + (\frac{\sigma_{||}}{\sigma_\perp})(\alpha p + 6\alpha_e q)^2\right]E_{pq} - \frac{\sigma_{||}}{\sigma_\perp}\sum_{m,n}{}'' E_{mn} \quad (5.64)$$

$$\mathcal{F}\left\{\left[\left(\dot\rho\left(\frac{\alpha}{r}\right)' - \frac{\alpha_e}{r}(\dot\rho' + \frac{\dot\rho}{r})\right)(m+6n) + \frac{2\dot\rho}{r}(\alpha m + 6\alpha_e n)\right]\sin(m\phi' + n\xi)\right\}$$

$$\mathcal{F}\{\mathrm{P}_1\Phi\} = \sum_{m,n}{}'' \Phi'_{mn}\mathcal{F}\left\{\left(\frac{\dot\rho}{r^2} - \frac{\dot\rho'}{r} + \dot\rho'' + \frac{36}{r^2}\frac{\partial^2}{\partial\xi^2}\dot\rho\right)\sin(m\phi' + n\xi) + 2\left(\frac{6}{r^2}\frac{\partial}{\partial\xi}\dot\rho + \left(\frac{\alpha}{r}\right)'\right)(m+6n)\cos(m\phi' + n\xi)\right\} \quad (5.65)$$

$$\mathcal{F}\{\mathrm{P}_0\Phi\} = \sum_{m,n}{}'' \Phi_{mn}\mathcal{F}\left\{(\nabla_T^2\frac{\alpha}{r})(m+6n)\cos(m\phi' + n\xi) - \frac{4}{r^2}\dot\rho'(m+6n)^2\sin(m\phi' + n\xi)\right\} \quad (5.66)$$

$$\mathcal{F}\{\mathrm{J}_1 E_{||}\} = \frac{\sigma_{||}}{\sigma_\perp}\sum_{m,n}{}'' E'_{mn}\mathcal{F}\{\dot\rho\cos(m\phi' + n\xi)\} \quad (5.67)$$

$$\mathcal{F}\{\mathrm{J}_0 E_{||}\} = -\frac{\sigma_{||}}{\sigma_\perp}\sum_{m,n}{}'' E_{mn}\mathcal{F}\left\{\frac{1}{r}(\alpha m + 6\alpha_e n)\sin(m\phi' + n\xi)\right\} \quad (5.68)$$

The terms in the equations are expanded into the possible combinations of harmonics. This is, of course, impractical for a large number of harmonics. We decided to take the largest two harmonics of $\dot\rho$, thereby making this approach feasible. For instance, the first term in operator P_0 (eqn. 5.51) is

$$\frac{2}{r}(\frac{\dot\rho}{r} - \dot\rho')(\frac{\partial}{\partial\phi'} + 6\frac{\partial}{\partial\xi})^2\Phi \quad (5.69)$$

Integration of this term to obtain the pqth equation yields

$$-\frac{2}{r}\sum_m\sum_n(m+6n)^2\Phi_{mn}\left\{\left(\frac{\epsilon_1}{r}-\epsilon_1'\right)\iint\sin\xi\sin(m\phi'+n\xi)\cos(p\phi'+q\xi)\,d\phi'\,d\xi\right.$$
$$\left.+\left(\frac{\epsilon_2}{r}-\epsilon_2'\right)\iint\sin 2\xi\sin(m\phi'+n\xi)\cos(p\phi'+q\xi)\,d\phi'\,d\xi\right\}$$

The integrals can be easily evaluated. The values of these integrals for each $pqmn$th combination are evaluated and stored in arrays that are fed into COLSYS.

The array of equations has the form

$$\begin{bmatrix} \\ \mathrm{L}_{2,pqmn} \\ \\ \end{bmatrix}\begin{bmatrix} \\ E''_{mn} \\ \\ \end{bmatrix} = \begin{bmatrix} \\ \mathrm{L}_{1,pqmn} \\ \\ \end{bmatrix}\begin{bmatrix} \\ E'_{mn} \\ \\ \end{bmatrix} + \begin{bmatrix} \\ \mathrm{L}_{0,pqmn} \\ \\ \end{bmatrix}\begin{bmatrix} \\ E_{mn} \\ \\ \end{bmatrix} +$$
$$\begin{bmatrix} \\ \mathrm{P}_{1,pqmn} \\ \\ \end{bmatrix}\begin{bmatrix} \\ \Phi'_{mn} \\ \\ \end{bmatrix} + \begin{bmatrix} \\ \mathrm{P}_{0,pqmn} \\ \\ \end{bmatrix}\begin{bmatrix} \\ \Phi_{mn} \\ \\ \end{bmatrix}$$
$$\begin{bmatrix} \\ \Phi''_{pq} \\ \\ \end{bmatrix} = -\frac{1}{r}\begin{bmatrix} \\ \Phi'_{pq} \\ \\ \end{bmatrix} + \frac{1}{r^2}(p+6q)^2\begin{bmatrix} \\ \Phi_{pq} \\ \\ \end{bmatrix} +$$
$$\begin{bmatrix} \\ \mathrm{J}_{1,pqmn} \\ \\ \end{bmatrix}\begin{bmatrix} \\ E'_{mn} \\ \\ \end{bmatrix} + \begin{bmatrix} \\ \mathrm{J}_{0,pqmn} \\ \\ \end{bmatrix}\begin{bmatrix} \\ E_{mn} \\ \\ \end{bmatrix} \qquad (5.70)$$

However, COLSYS does not allow a matrix to preface the highest derivative term. In other words, the program does not allow $[\mathrm{L}_2]$ in it's original form.

One easy way to cast the equations into an acceptable form is to divide (5.45) through by $\mathrm{L}_2 = 1 + \frac{\sigma}{\sigma_\perp}\dot{\rho}^2$. One soon discovers that the Fourier transformation of

these coefficients after the division is a numerical nightmare. The functions have sharp gradients and vary over a large range due to the $\frac{\sigma}{\sigma_\perp}\dot{\rho}^2$ term.

Another method that saved a lot of computation time is to convert the equations into their Fourier components first before dividing by L_2. This casts L_2 into a matrix form of size dependent on the number of Fourier harmonics one chooses. The matrix is then inverted and multiplied to the right-hand side of the equation. The reason why this saves time is because the Fourier series for L_2 has been truncated first before bringing it over to the right side of the equation. The first equation now becomes

$$\begin{bmatrix} E''_{pq} \end{bmatrix} = \begin{bmatrix} \mathrm{L}_{2,pqmn} \end{bmatrix}^{-1} \left\{ \begin{bmatrix} \mathrm{L}_{1,pqmn} \end{bmatrix} \begin{bmatrix} E'_{mn} \end{bmatrix} + \begin{bmatrix} \mathrm{L}_{0,pqmn} \end{bmatrix} \begin{bmatrix} E_{mn} \end{bmatrix} + \begin{bmatrix} \mathrm{P}_{1,pqmn} \end{bmatrix} \begin{bmatrix} \Phi'_{mn} \end{bmatrix} + \begin{bmatrix} \mathrm{P}_{0,pqmn} \end{bmatrix} \begin{bmatrix} \Phi_{mn} \end{bmatrix} \right\} \quad (5.71)$$

5.4 Results

The decision was made to keep this code linear. As is, it is already computationally costly. Running some 2D cases with and without the nonlinearity in $\sigma_{||}$ convinced us that using a linear $\sigma_{||}$ is effective for calculating AC losses. At 1T/s, the discrepancy as shown in fig. 5-14 is small. Even at 10T/s, the discrepancy in loss calculations for a single strand is only 25% as shown in fig. 5-15. Saturation effects for a cable-size geometry is even less important because it takes a higher $\dot{B}$ rate to saturate the same percentage area as for something as small as a strand.

Since $\dot{\rho}$ is assumed to have 2 harmonics, then $\dot{\rho}^2$ (or some derivative combination), which is the highest order of $\dot{\rho}$ that appears in the equations, has 4 harmonics. The-

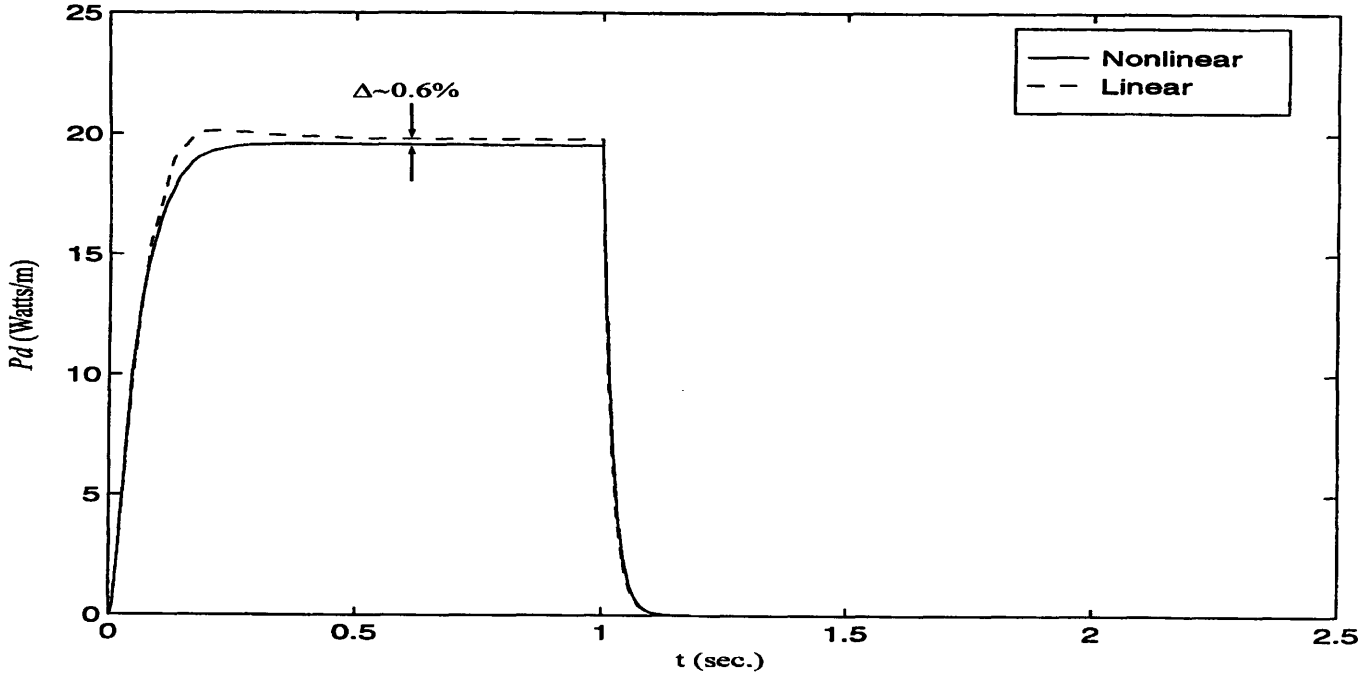

Figure 5-14: Saturated vs. non-saturated power loss for $\dot{B}$= 1T/s

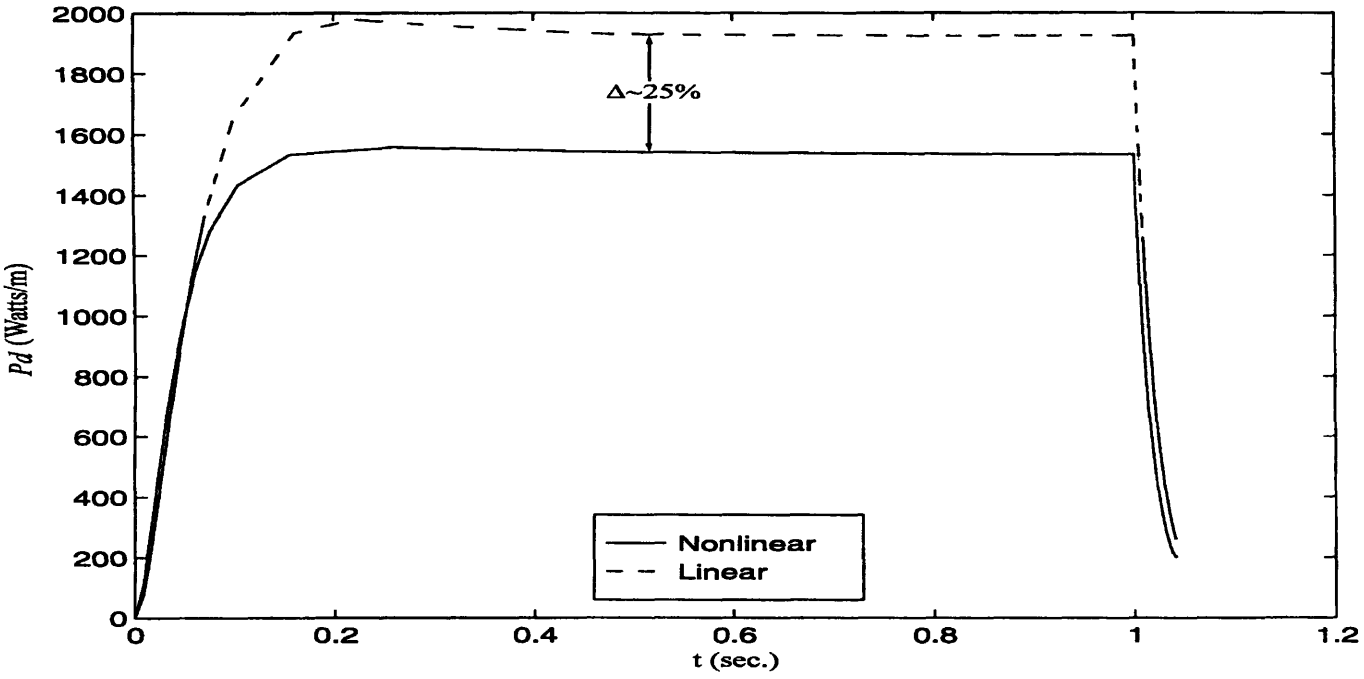

Figure 5-15: Saturated vs. non-saturated power loss for $\dot{B}$= 10T/s

oretically, there should be an infinite number of E_{pq} since lower harmonics couple to form higher harmonics and this process can go on indefinitely.

The number of coupled ODE's that need to be solved is dependent on the number of harmonics picked for the variables

$$E_{||}(r,\phi^{'},\xi,t) = \sum_{n=0}^{N}\sum_{m=-M}^{M} E_{mn}(r,t)\cos(n\xi + m\phi') \tag{5.72}$$

$$\Phi(r,\phi^{'},\xi,t) = \sum_{n=0}^{N}\sum_{m=-M}^{M} \Phi_{mn}(r,t)\sin(n\xi + m\phi') \tag{5.73}$$

For the outer summation, for $n \neq 0$, there are $2\times M+1$ terms in the inner summation for each n. For $n = 0$, since the negative m terms are the same as the positive m's, there are only $M + 1$ distinct harmonics. Lastly, there are two equations for each harmonic. Therefore, the total number of equations is $2 \times [N \times (2 \times M + 1) + M + 1]$.

Since $\sigma_{||}$ is taken to be constant, the ϕ' harmonics will come from the source terms. Since the field is uniform and transverse to the cable, $\dot{B}^A$ has only one harmonic (see section 2.5.1). Thus, $M = 1$. This leaves the choice for N open. The limit on N is determined by the amount of computation time needed to solve $2 \times N \times (3N + 2)$ number of equations.

For instance, for the case $N = 4$, this translates to 28 coupled equations and 56 variables for COLSYS! Curiously, the losses for different N values are quite different, specifically, the loss increases with increasing number of harmonics and the answer does not converge as one goes to higher harmonics. This, in itself, shows an inconsistency in the results. As one goes to higher harmonics, the difference in the losses should be of second order, to be consistent with the higher harmonic fields being second order. However this is not the case. It turns out that solving for more harmonics actually changes the leading order term!

To circumvent this strange, unphysical behaviour, we need to examine more closely

why there seems to be positive feedback between the leading order harmonics and the higher order ones. Fig. 5-16 shows the profile along the x-axis of $E_{||}$ and E_r at $z = 0$. It is even clearer here that there is a concentration of current around $\pm$8mm. This is a very curious effect unique to this cable configuration.

The peaking of the current coincides with the zero crossing of α as shown in fig. 5-10. Physically this corresponds to a cylindrical sheet around $r \approx 8$mm where there is no helical twist. For radii less than the zero crossing, the strands are winding in one direction and for radii larger than the zero-crossing, the strands are winding in the other direction. The result is that currents are trapped around this area. The problem becomes inherently without bound. The only saving grace is $\dot{\rho}$ which allows for some transverse flow of currents. The coefficients of $\dot{\rho}$ are also what contributes to the ξ harmonics.

The question to be asked here is: does it make any physical sense to have this zero-crossing in the $\rho\dot{\psi}$ coefficient? Does having this cylindrical sheath that traps current represent a physical reality or a numerical anomaly due to the smoothing of the trajectory components?

To answer this question, a *noise* factor is introduced. Since α is never uniformly zero in any cross-section (see fig. 5-17), a noise term actually seems more realistic. This new α is expressed as

$$\alpha = \alpha(r) + n_s(r, \phi, z) \tag{5.74}$$

One can see the frequency spectrum of $\rho\dot{\psi}$ to have a small background noise and a dominant dc harmonic. n_s, on its own, has a neglible effect and does not couple to the fields. However, due to the fact that the governing equations have an α^2 term *and* that the dc component of α goes to zero somewhere, n_s can be significant in the

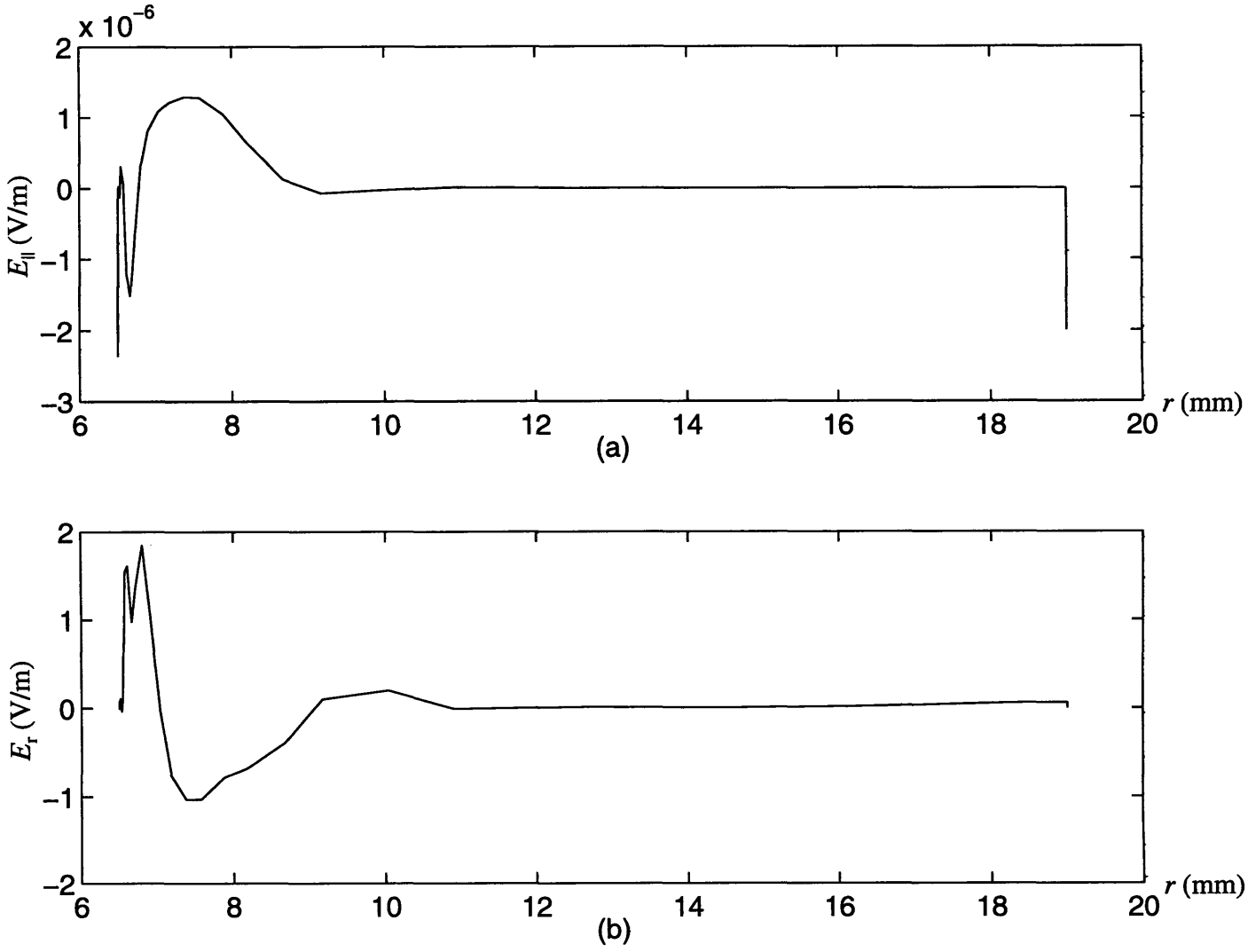

Figure 5-16: (a) $E_{||}$ profile showing peaks around zero-crossing of α and similary (b) E_r profile.

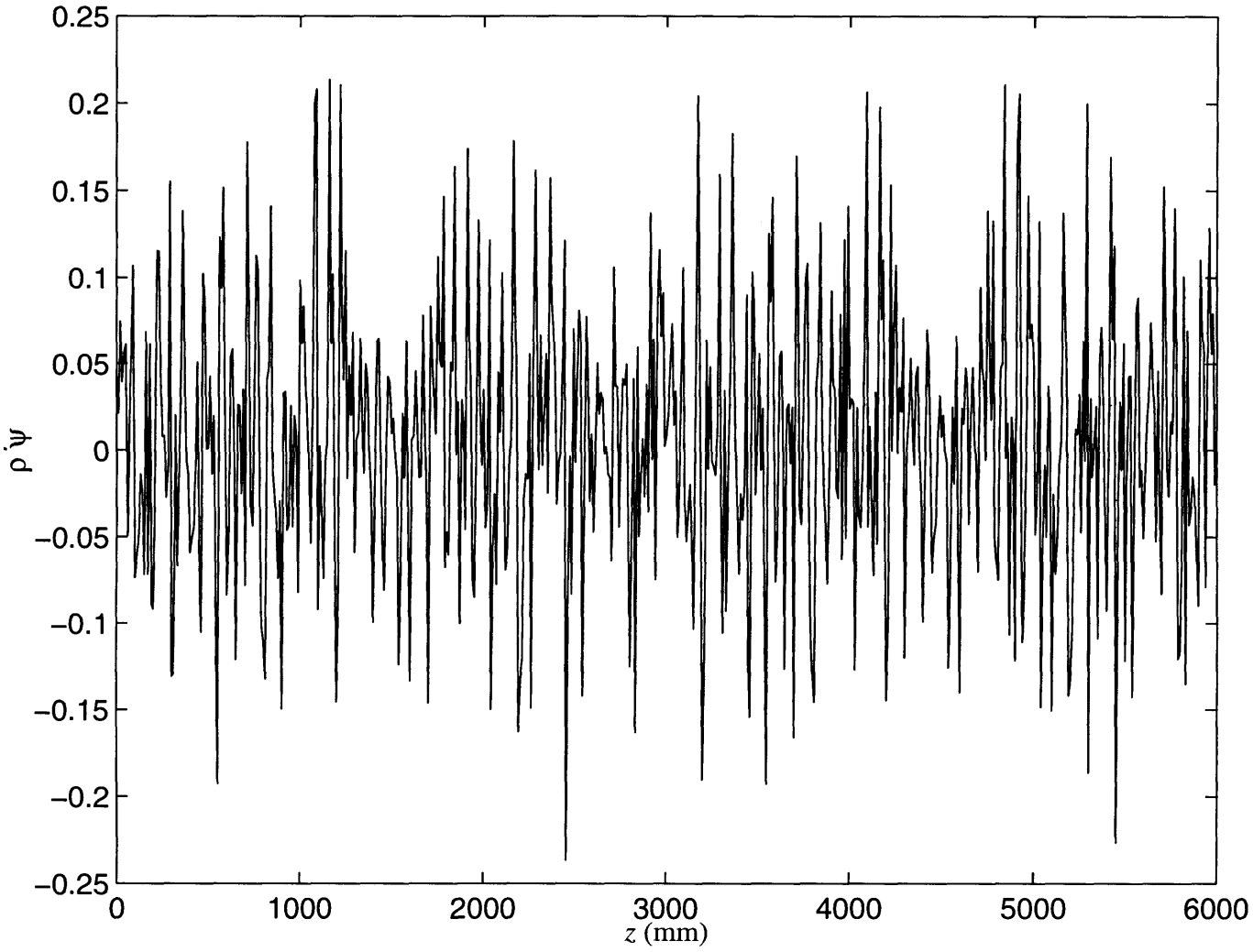

Figure 5-17: $\rho\dot{\psi}$ vs. z at x=0 and y=8mm. Illustration of noise at r=8mm which is the zero-crossing of α.

zero-crossing region. Part of the first term in equation 5.56 is

$$\frac{\sigma_{||}}{\sigma_{\perp}}\frac{1}{r}(\alpha p + 6\alpha_e q)^2$$

Only the squared terms of α contain contributions from n_s since n_s^2 has a dc component. Therefore, the additional terms are

$$< n_s >^2 (p + 6q)^2 \tag{5.75}$$

where $< n_s^2 >$ is the average or dc value of n_s^2.

Because 2 harmonics were picked for $\dot{\rho}$ (ξ and 2ξ), the same harmonics were picked for n_s to be consistent. Fig. 5-18 shows the value of $< n_s^2 >$ ranging from 7mm to 18mm. The fitted quadratic curve is what is used in the code.

A set of cases with varying number of harmonics using this new α is examined. Table 5.2 shows the steady-state power loss for different harmonics in ξ. In this case, it is clear that the results converge. COLSYS is set to allow a maximum of 40 equations and 80 unknowns, the equivalent of $N = 6$ as the highest value of N allowed. COLSYS can be expanded to accomodate even more harmonics but the computation time is already costly for $N = 4$. Originally, COLSYS could only take 20 equations or $N = 2$. The computation time between the $N = 2$ and the $N = 4$ cases is almost 5 times. This leads one to believe that COLSYS is optimized for a maximum of 20 equations.

A typical case takes approximately one hour to run with $N = 4$. This is a reasonable amount of time and the discrepancy in results between $N = 4$ and $N = 6$ is quite small. Thus, $N = 4$ will be used for all future cases.

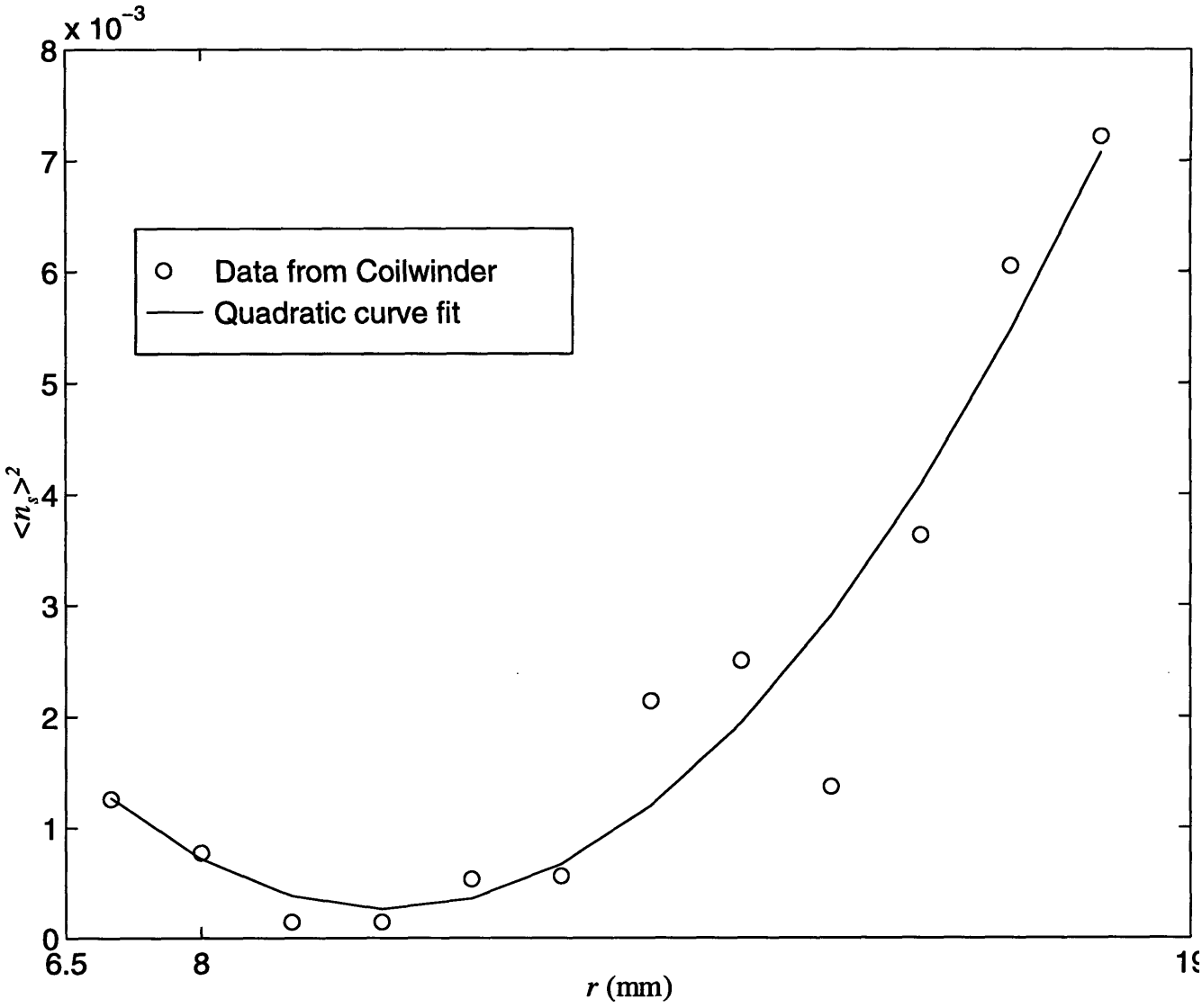

Figure 5-18: Mean-squared noise of α vs. radius of cable.

(M=1)	Steady-state power loss (W/m^3)	Error
N=2	1560.8	14.4%
N=4	1378.1	1%
N=6	1364.6	0%

Table 5.2: List of code results using different number of harmonics to describe $E_{||}$ and Φ

5.4.1 Field and Loss Profiles

Figures 5-19 to 5-21 show the 3D mesh plots of the steady-state electric fields in ramped B-field conditions. The radial and azimuthal currents have a large peak of opposite sign near either side of the inner rim. A plot of the magnitude of E_r vs. r at $\phi = \pi/2$ is shown in fig. 5-22. One can see that the concentration of transverse currents is in the proximity of the zero-crossing. In fact, the spatial distribution of power density as shown in fig. 5-23 is added evidence of the concentration of loss and currents in the vicinity of the zero-crossing. Therefore, the added noise in (5.74) did not change the qualitative behavior of the system although it stabilized the numerics.

Losses

The loss expression for a cable most often found in literature is similar to that of a single strand but with a different geometric factor.

$$p_d = \frac{\dot{B}^2}{\mu_0} n\tau \tag{5.76}$$

where $n\tau$ is a function of $\sigma_\perp$.

Fig. 5-24 shows a plot of normalized steady-state power density loss vs. $\sigma_\perp$. It is reassuring to see that power loss is still a linear function of the transverse conductivity similar to a single strand. Fig. 5-25 shows a plot of normalized power loss vs. $\dot{B}$. It is a squared dependence of the ramp rate which is also consistent with eqn. 5.76.

The value for the transverse conductivity $\sigma_\perp$ is a topic of much debate. No one is certain as to how to go about obtaining it experimentally. There have been estimates ranging anywhere as low as 10^4 to as high as 10^7. Since there is no reliable number available for $\sigma_\perp$, this can be used as a parameter to be determined by fitting code results with experimental loss data. The code can be used in this way to find the

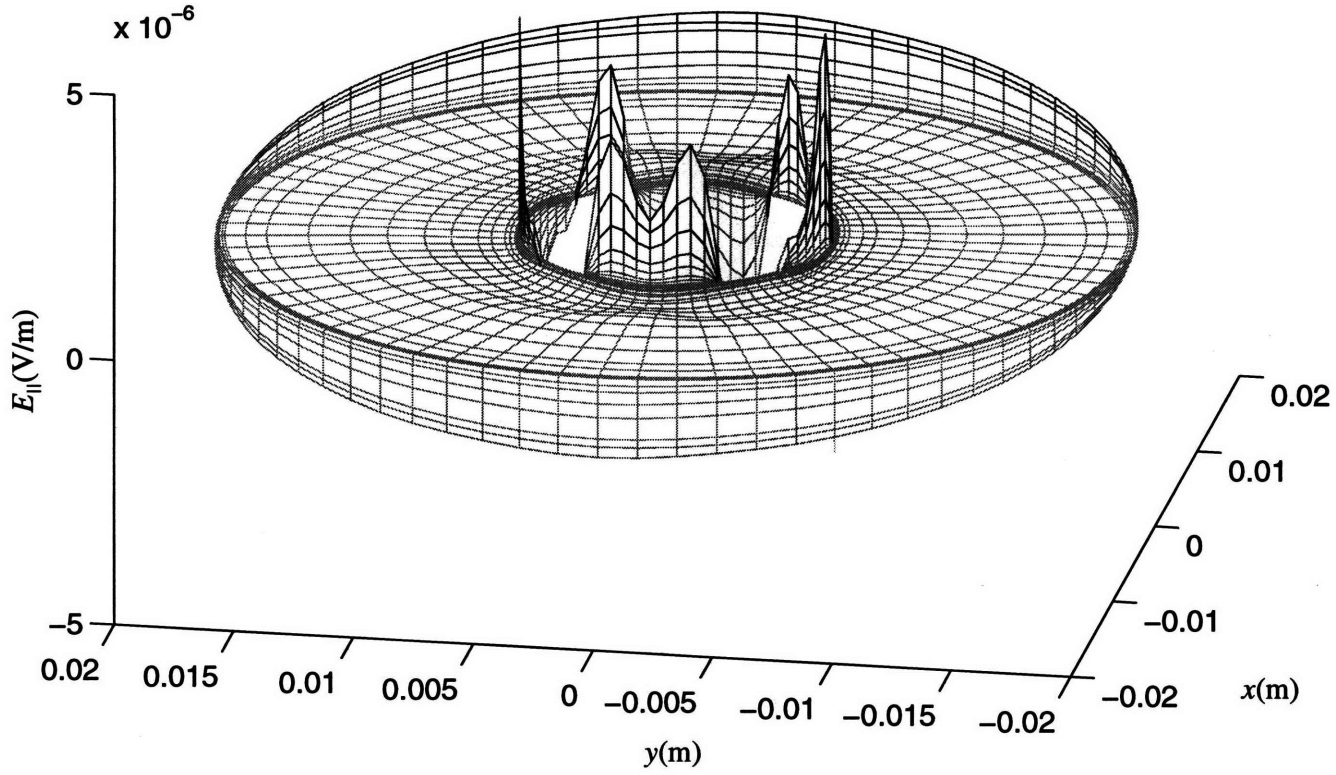

Figure 5-19: Profile of $E_{||}$ at $z = 0$. One can see 6 peaks corresponding to the 6 petals.

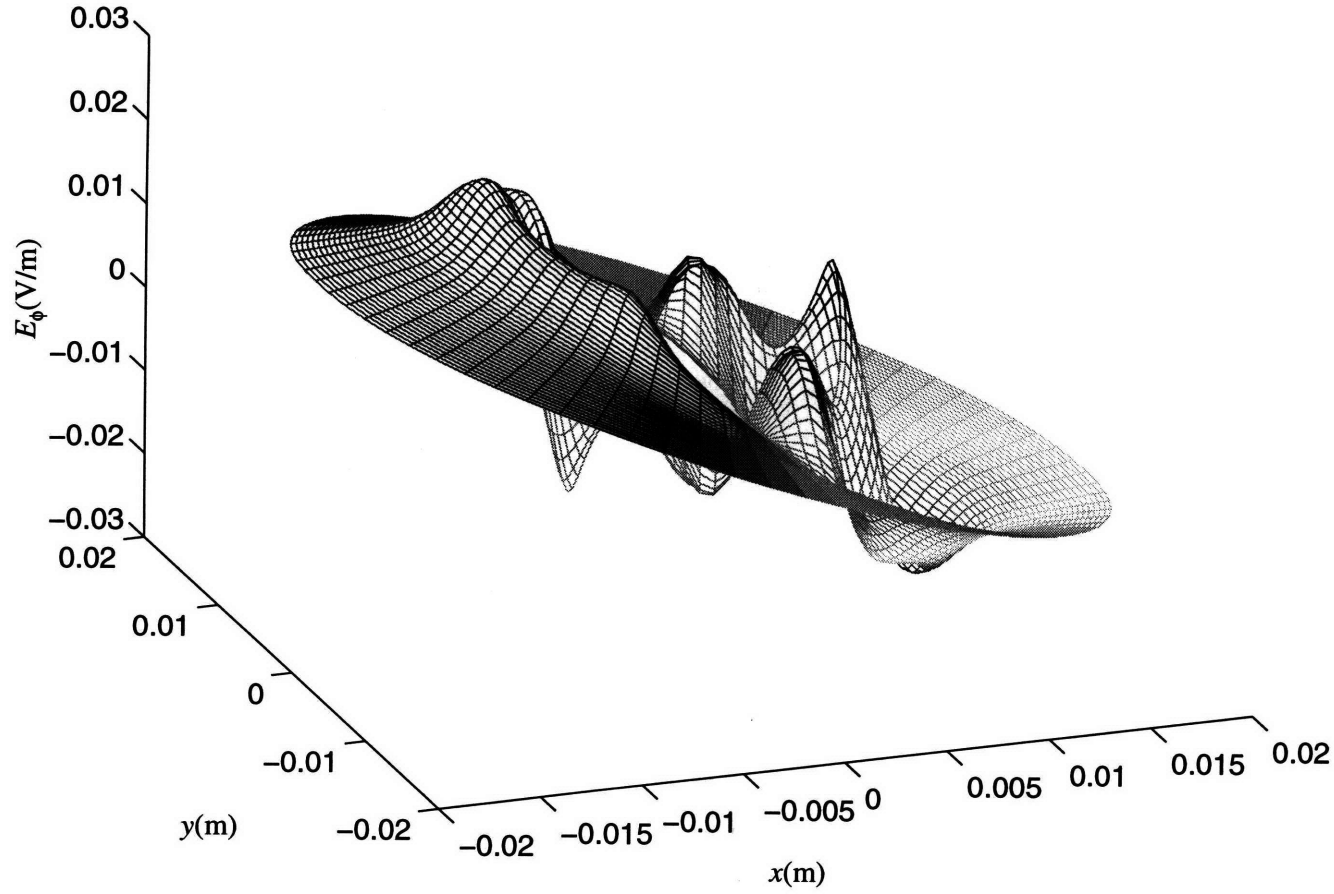

Figure 5-20: Profile of E_ϕ at $z = 0$. The azimuthal field reverses signs at the zero-crossing.

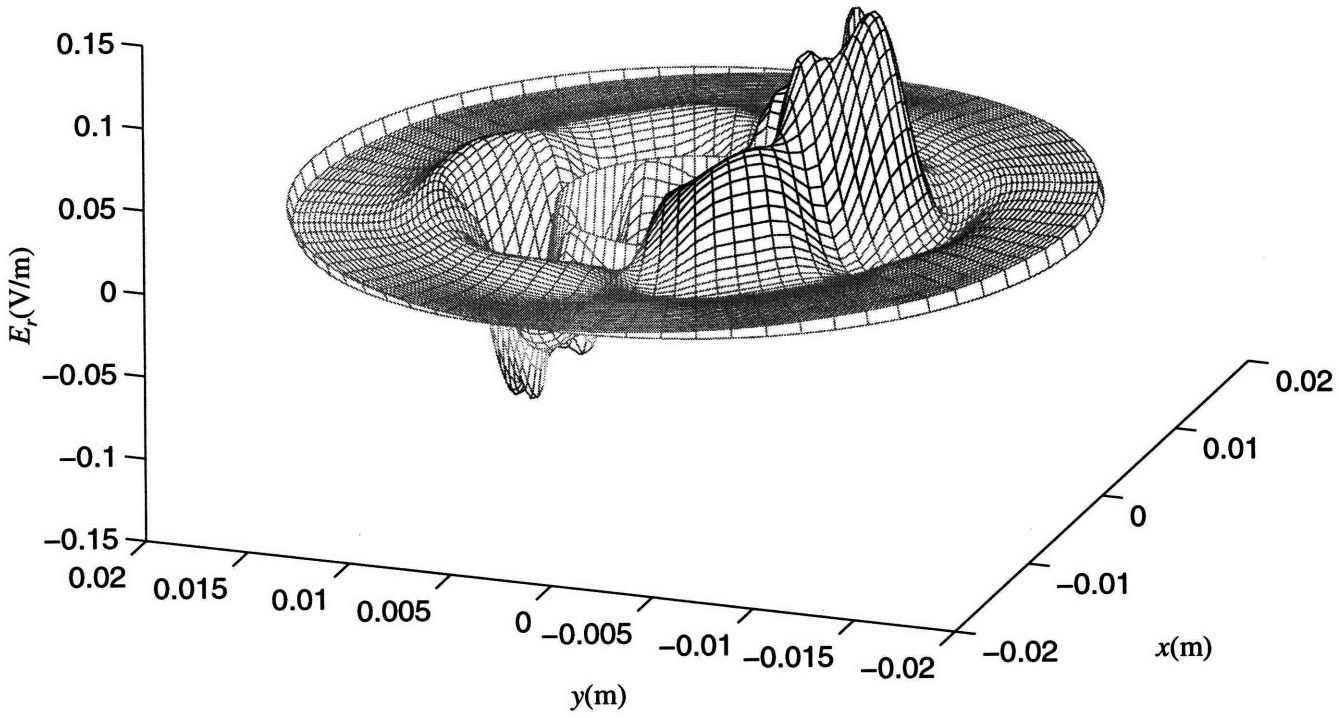

Figure 5-21: Profile of E_r at $z = 0$.

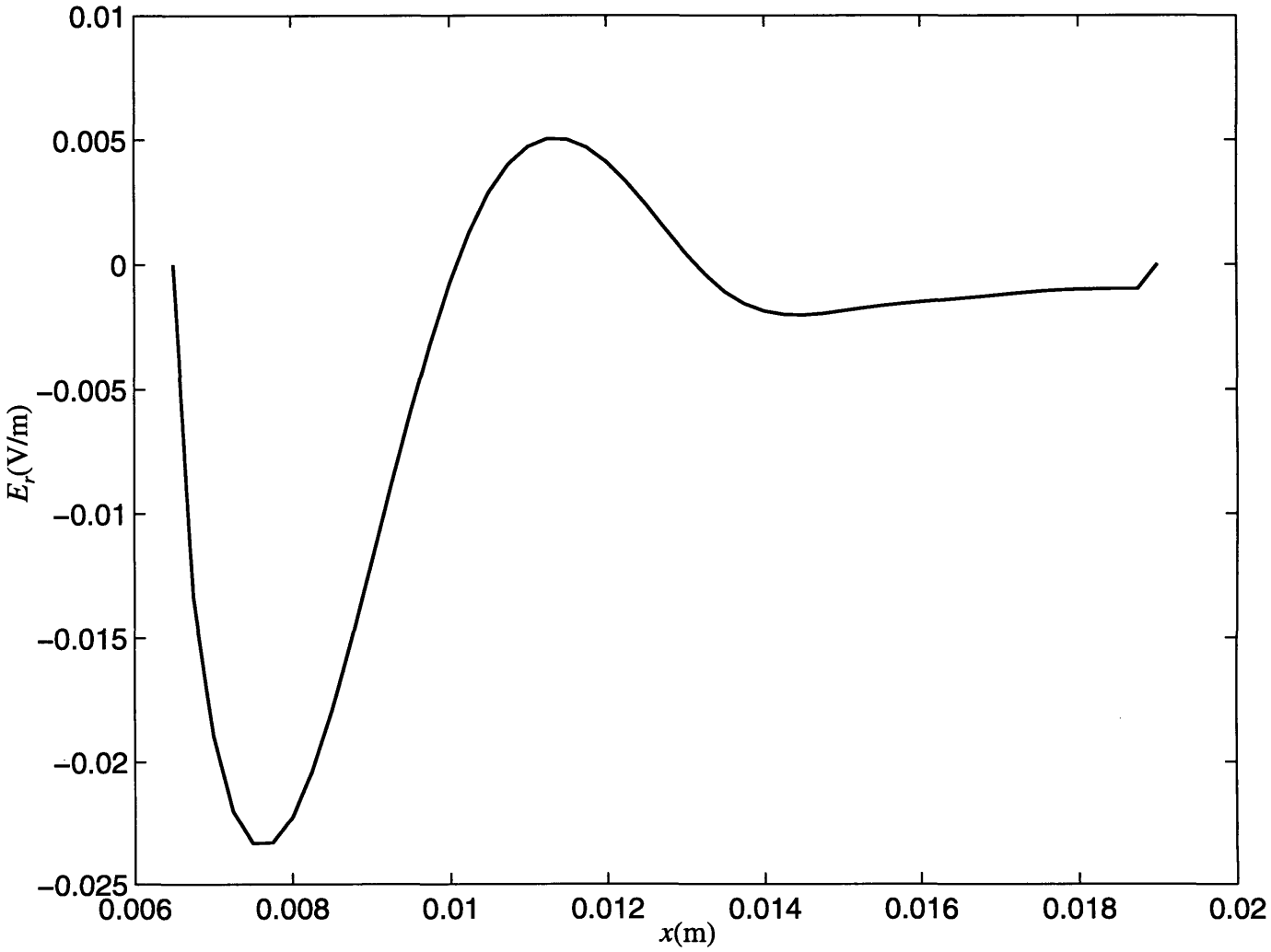

Figure 5-22: Profile of E_r at $z = 0, \phi = \pi/2$. There are large peaks in the vicinity of the zero-crossing(8mm).

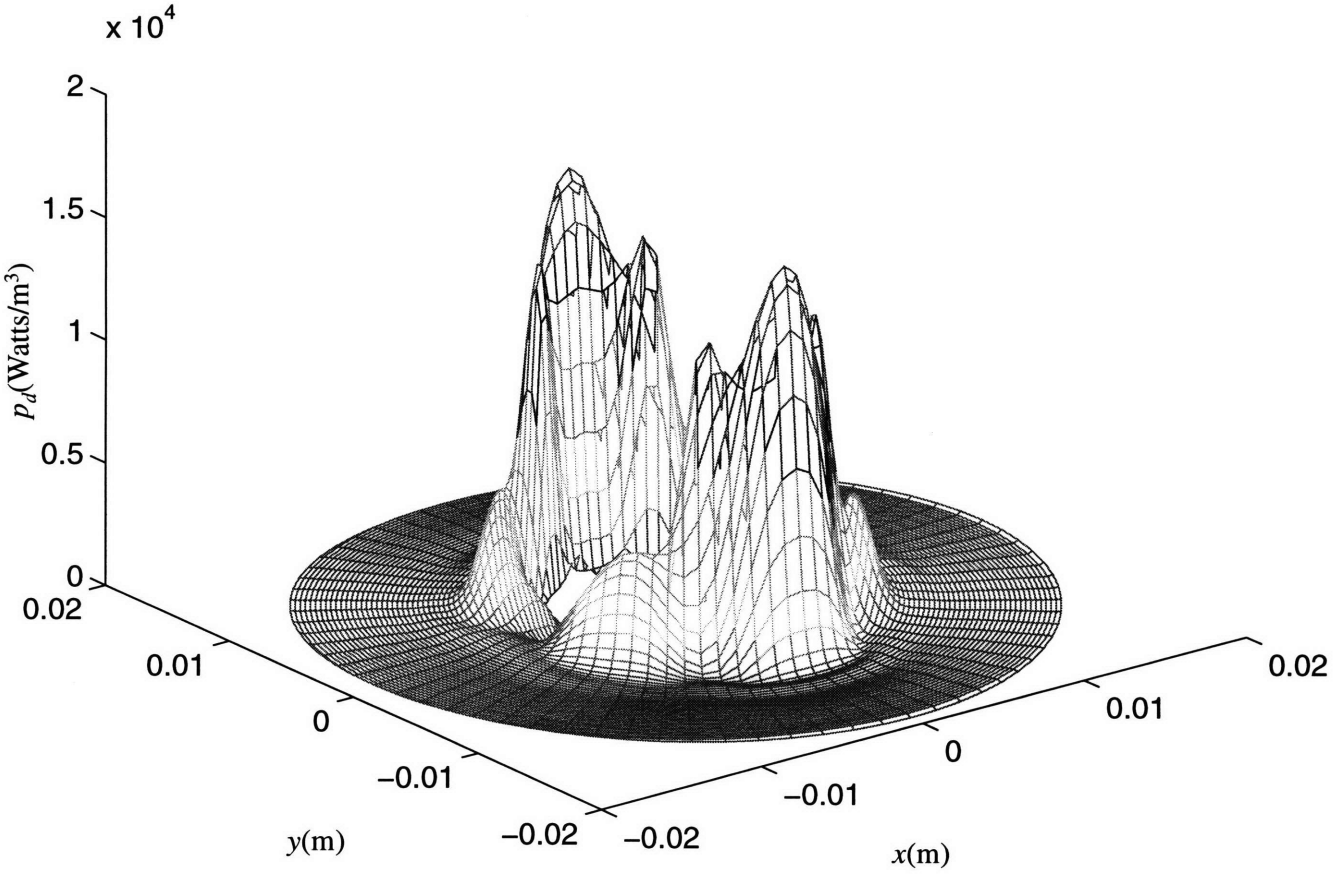

Figure 5-23: Profile of p_d at $z = 0$. One can see that the loss due to E_r dominate.

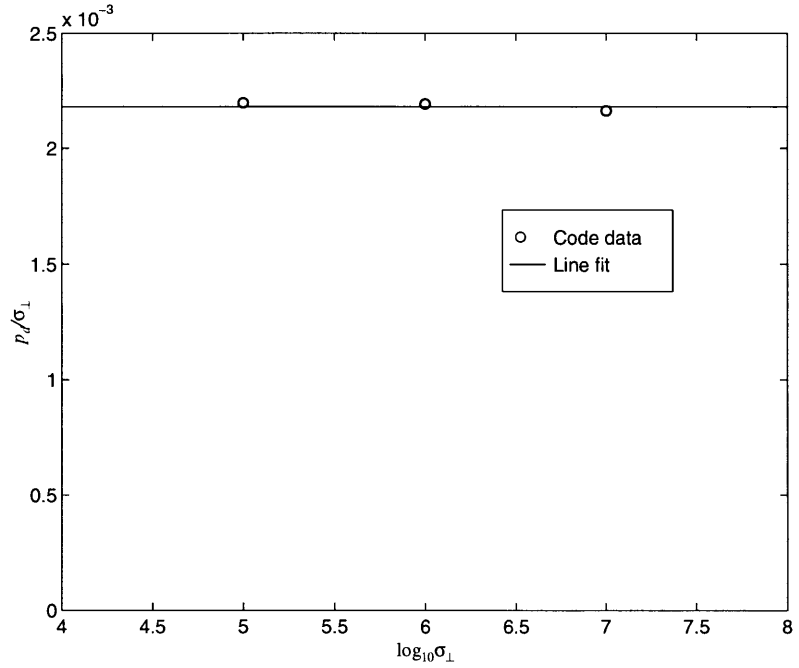

Figure 5-24: A plot of power density p_d normalized to $\sigma_\perp$ to show that the power loss is linearly dependent on $\sigma_\perp$.

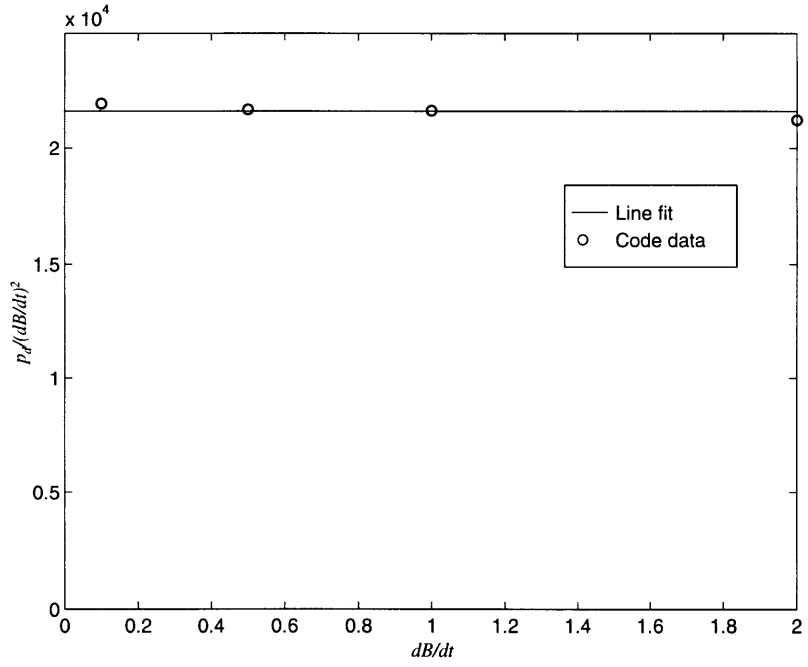

Figure 5-25: A plot of power density p_d normalized to $\dot{B}^2$ to show that the power loss is dependent on $\dot{B}^2$.

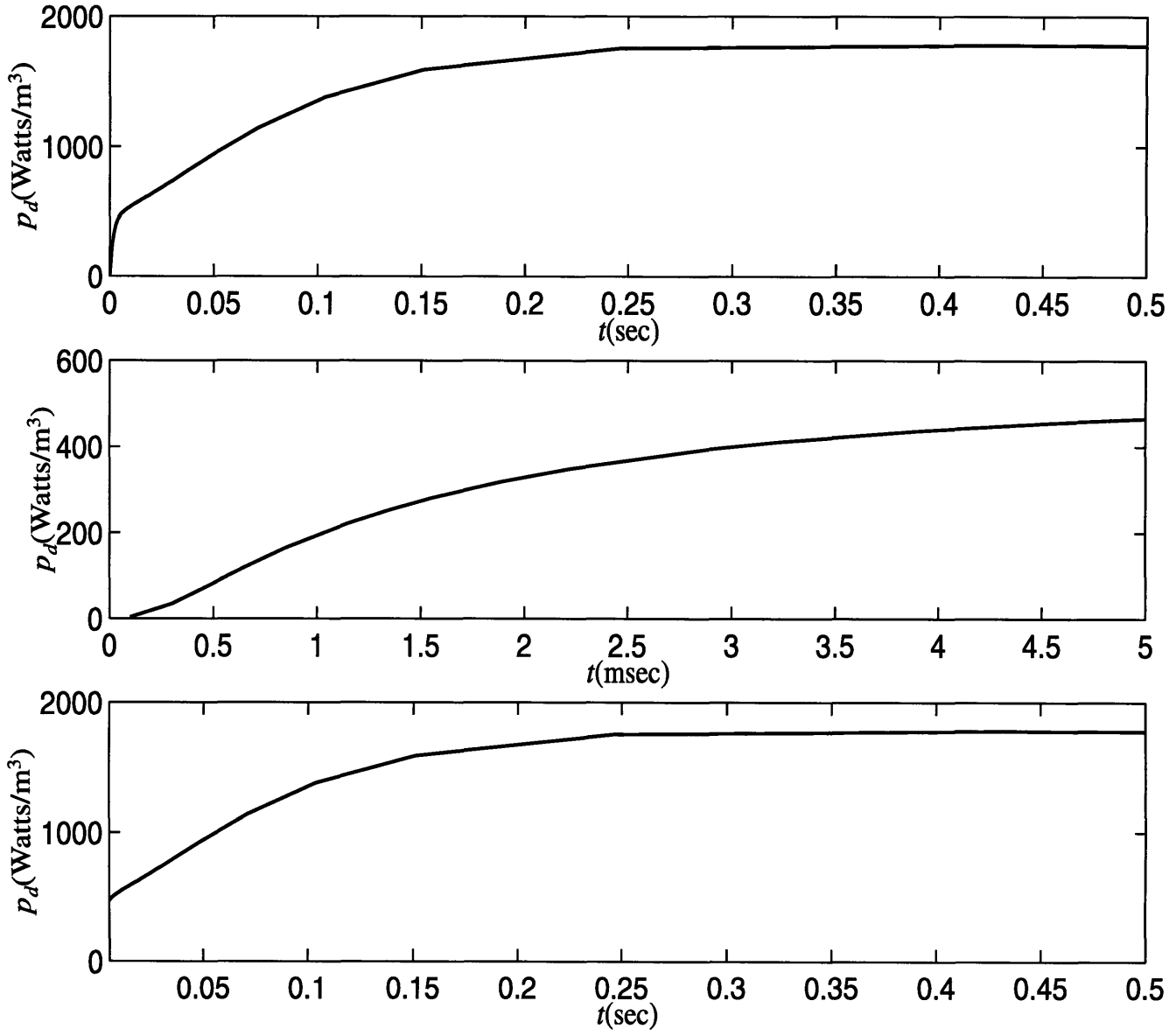

Figure 5-26: A plot of power density p_d vs. time. The first curve shows a very short time constant (τ_s) close to $t = 0$ and a much longer one (τ_l) past 5msec. The second curve is a magnification of the curve around $t = 0$ to show τ_s. Third graph is a plot of power loss between 5msec and .5sec to show long time constant.

"effective transconductance" of the cable.

Fig. 5-26 shows the time evolution of the power loss density for a cable with $\sigma_\perp = 1 \times 10^6(\Omega\text{-m})^{-1}$. On close examination, the curve looks like it has more than one major time constant. In fact it seems to have two distinct ones - a short one (τ_s) and a long one (τ_l). Fig. 5-26 shows a blow-up view of p_d in the two different regimes. The effective time constant, if one uses $p_d \approx p_0(1 - e^{\frac{-2t}{\tau}})$ where p_0=1.74kWatts/m^3, and choosing the $1/e$ roll-off point, yields a value of $\tau \approx$ 130msec.

Substituting into the equation for steady-state p_d, we have

$$\begin{aligned} p_d &= \frac{\dot{B}^2}{\mu_0} n\tau \\ n &= \mu_0 \frac{p_d}{\tau \dot{B}^2} \\ &= .067 \end{aligned} \tag{5.77}$$

This is a far departure from the $n = 2$ value used for a strand. This is due to the additional τ_l as mentioned before. A closer examination of the electric fields show relatively smooth, low gradient profiles for $0 < t < \tau_s$. However, the peaks around the zero-crossing start to grow after τ_s with a longer time constant associated with it. Because peak losses occur within the zero-crossing zone and not over the whole cable, it contributes only to a fraction of the loss. This explains the reason why n, the geometric factor, is so small. This leads us to believe that without the zero-crossing, we may achieve lower losses and shorter time constants. This aspect will be addressed under "Design Recommendations".

The effective twist pitch is then

$$L_{p,eff} = 2\pi\sqrt{\frac{n\tau}{\mu_0\sigma_\perp}} \tag{5.78}$$

$$= .523\text{m} \tag{5.79}$$

The effective twist pitch is a bit more than the length of the last twist pitch which is .4m.

5.4.2 Loss data

In the scope of the ITER Task Agreement for AC losses, a benchmark action was agreed in May 1993 to solve the discrepancies frequently observed between coupling loss results measured on similar samples at different labs and to provide a common basis for the assessment of the coupling losses of the ITER conductor.

The geometry of the test cable was not the full-size design. The 192-strand sub-bundle (one of the 6 substages that comprise the final stage) was tested instead. The specimen was manufactured similarly to the actual cable but as the final step, was compacted into a circular rather than a petal shape. The complete final report was not made available until Feb. 1996.

Although the experimental cable resembles nothing like the actual cable, there is one crucial similarity. The 192-strand small cable, according to the analytic expression derived for α, has a zero-crossing for this coefficient.

According to the results from our analysis of the full-size design, this zero-crossing should lead to a time constant that is very long and a resulting n that is much smaller than 2. It is the intent of this section to show that this phenomenon can be extrapolated from the measured loss data.

Fig. 5-28 and 5-29 show experimental loss data for different excitation waveforms. The first graph resulted from a sawtooth waveform with ΔB=.4T, the second a sinusoidal waveform with $\Delta B = \pm .2T$.

From Wilson, the energy loss per cycle per volume for a B-field of $\Delta B e^{i\omega t}$ is

$$q_e = \frac{\Delta \dot{B}^2}{4\mu_0} \frac{\pi \omega n \tau}{(1+\omega^2\tau^2)} \tag{5.80}$$

where $p_d = \frac{\dot{B}_i^2}{\mu_0} n\tau$ and $\dot{B}_i$ satisfies the relation

$$B_i = B - \dot{B}_i \tag{5.81}$$

For a sawtooth waveform, the derivation is fairly straightforward and the results are presented here. The waveform and variables are defined in figure 5-27. The energy loss per cycle per unit volume is

$$q_e = \frac{2}{\mu_0} n\tau(\Delta B\dot{B} - \dot{B}^2\tau) \tag{5.82}$$

The first term is the familiar linear portion of the loss. This part of the data was used to derive $n\tau$. When τ becomes a significant portion of T_m, the quadratic term also contributes. This explains why the experimental data starts to curve for higher $\dot{B}$ values.

If the theory of the zero-crossing of α holds true, then n should be small and the experimental data should show this. Figures 5-28 and 5-29 show the fit of eqns. 5.80 and 5.82. For both waveforms, it yielded a value of $n \approx .18$. These results are about 3 times bigger than the n value derived from the code. This discrepancy may be due to the fact that it is a different geometry. It may also be because loss is highly sensitive to any error in the strand trajectories and a small error in the trajectories may give a substantial error in the loss. However, the data still gives a sufficiently small n. Therefore, there is strong evidence that indeed the zero-crossing leads to a very long time constant and a small n.

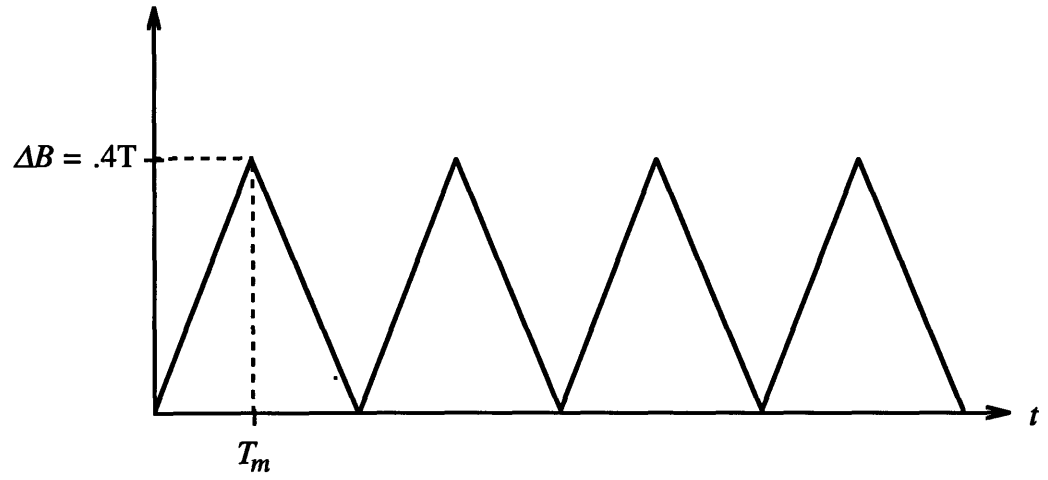

(a)

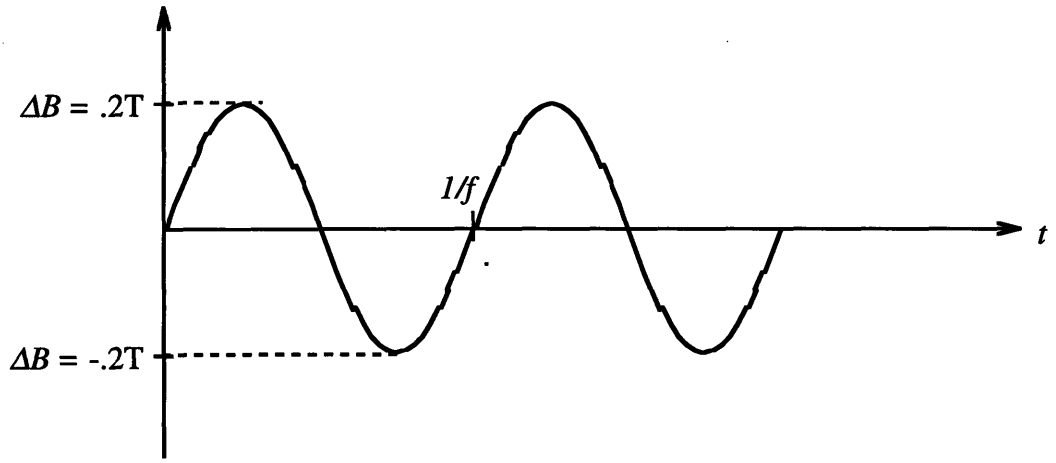

(b)

Figure 5-27: The plots show the waveforms of the excitation B-field for the 192-strand benchmark experiment and how ΔB is defined. (a) sawtooth and (b) sinusoid.

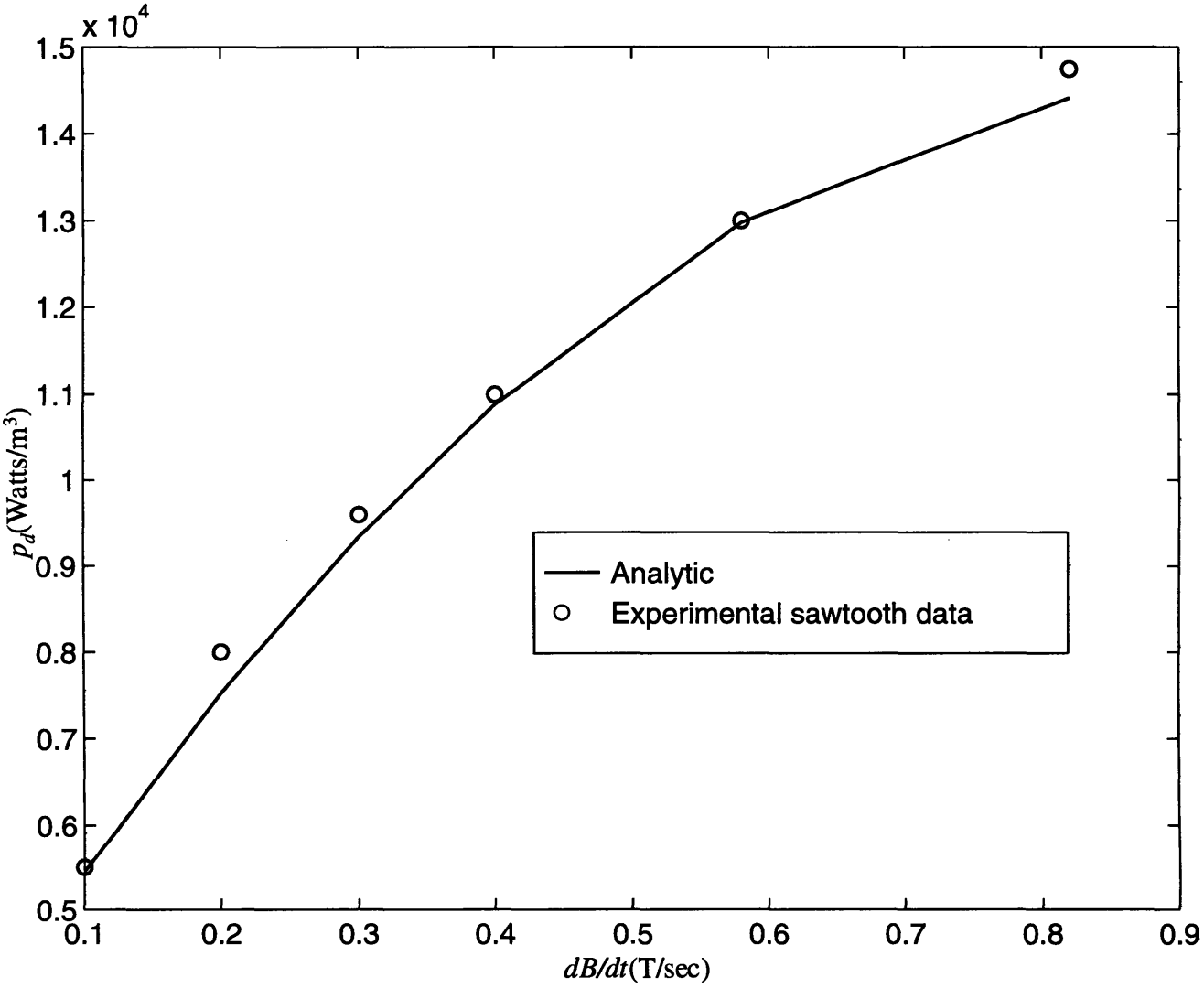

Figure 5-28: Experimental loss data of 192-strand sub-bundle for ΔB=.4T sawtooth wave form. It shows a good fit with analytic results for $n \approx .18$ and $\tau \approx 217$msec.

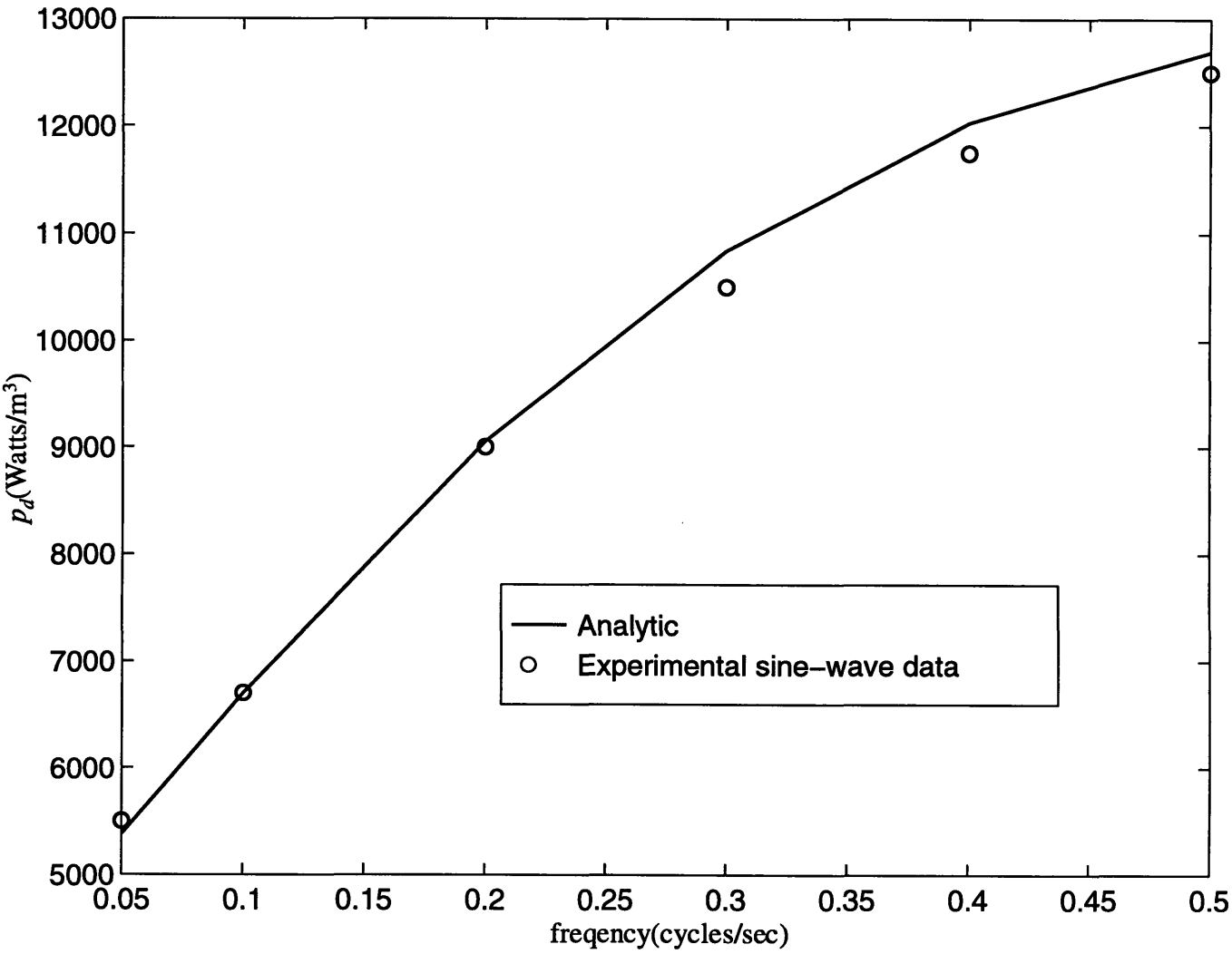

Figure 5-29: Experimental loss data for 192-strand sub-bundle for $\Delta B = \pm.2$T sinewave. It shows a good fit with analytic results for $n \approx .18$ and $\tau \approx 244$msec.

5.5 Design Recommendations

From the previous section, it is quite clear that the zero-crossing in α is an undesirable trait for a cable geometry. Let us examine the physical mechanism that leads to the zero-crossing.

We know that the direction of the twisting reverses somewhere in the cable. This is most likely due to the interaction of the rates of twist between the fourth stage (second to last) and the last stage. As pictured in fig. 5-30, the rotational motion of the two stages add to each other towards the outer rim and subtract from each other towards the inner rim. The relationship in magnitude between the two twisting motions determines the location of the zero-crossing.

To shift the zero-crossing to outside the strand area requires either increasing the twist of the final stage or decreasing the twist of the fourth stage. This is equivalent to either decreasing the fifth twist pitch (L_{p5}) or increasing the fourth twist pitch (L_{p4}). Ultimately, the choice would be made according to manufacturing constraints.

For illustrative purposes, we decided to decrease L_{p5}. The analytic expression for α was used to pick the maximum value of L_{p5} such that there is no zero-crossing in the strand region. Eqn. (5.18) yielded L_{p5}=200mm. This new twist pitch was then inputted to the cable winder program and a new α and $\dot{\rho}$ profile were extracted. The α and $\dot{\rho}$ values are plotted in figures 5-31 and 5-32.

Fig. 5-33 shows a comparison between the power density for the old and new design for an estimated $\sigma_\perp = 1 \times 10^6 (\Omega\text{-m})^{-1}$. The exact steady-state power density values are

$$p_d(\text{present design}) = 1.69\text{mJ/cc/sec.} \tag{5.83}$$

$$p_d(\text{present design}) = .103\text{mJ/cc/sec.} \tag{5.84}$$

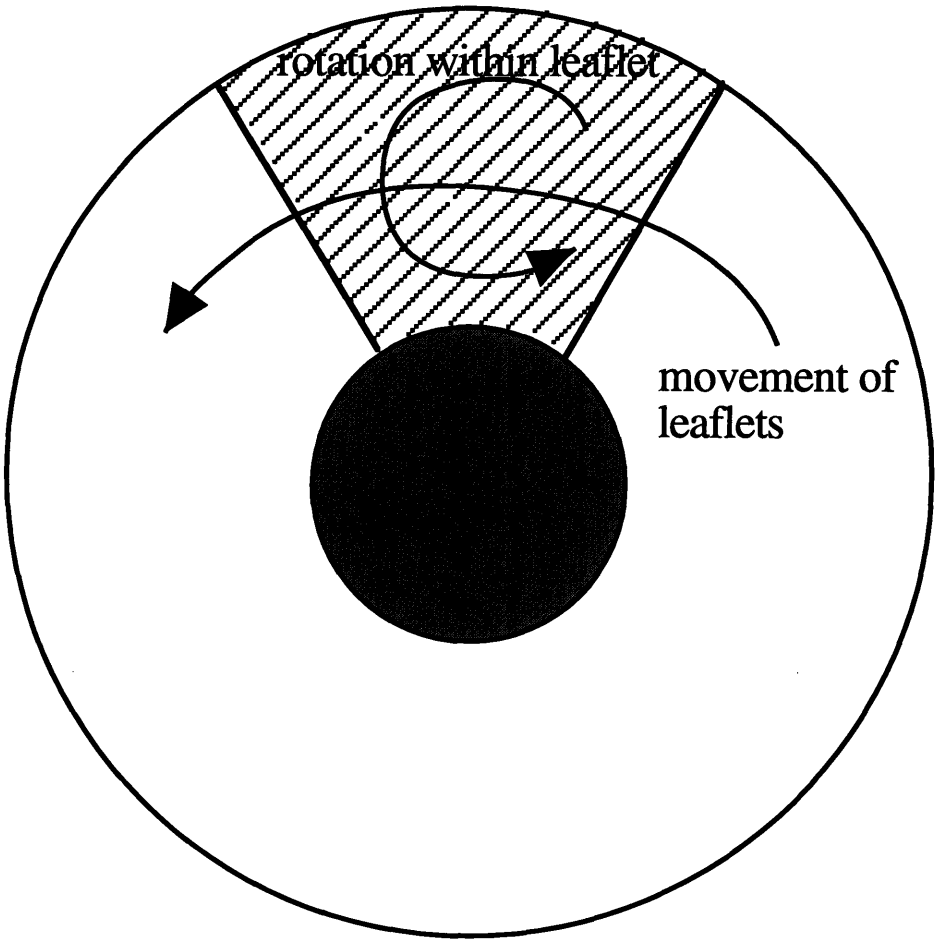

Figure 5-30: Schematic depiction of the constructive and destructive interference between the fourth and fifth stage on the rotational motion of the strands.

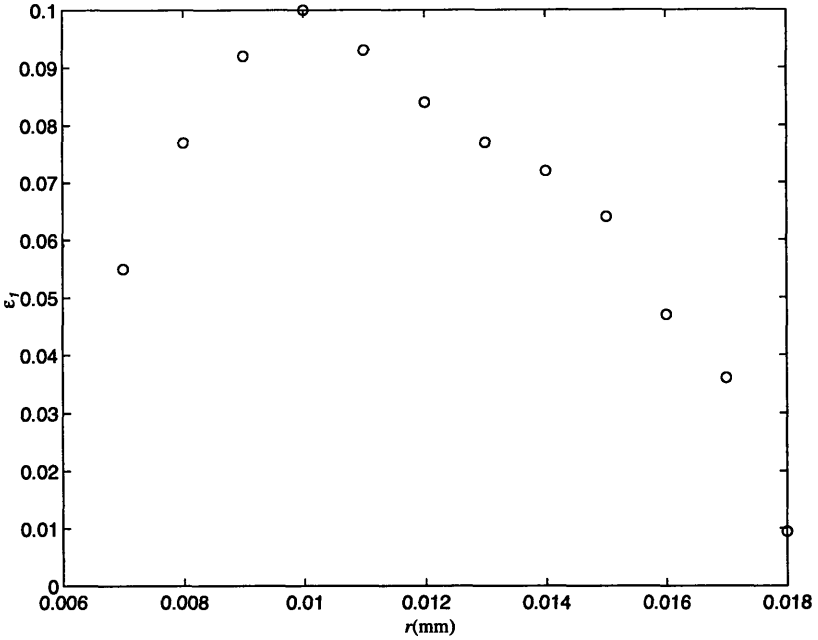

Figure 5-31: $\dot{\rho}$ data from cable winder for improved design.

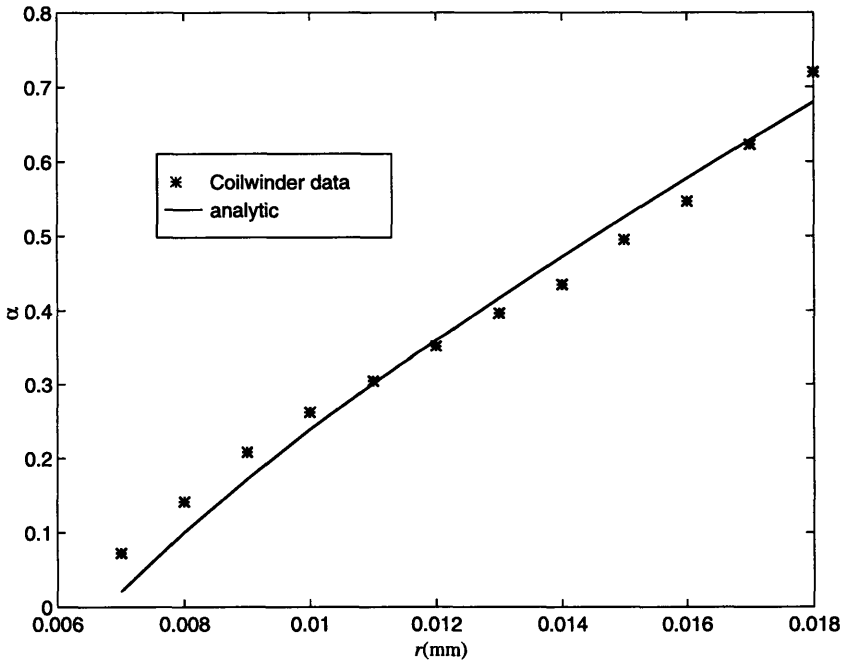

Figure 5-32: Both α data from cable winder and from analytic expression for improved design.

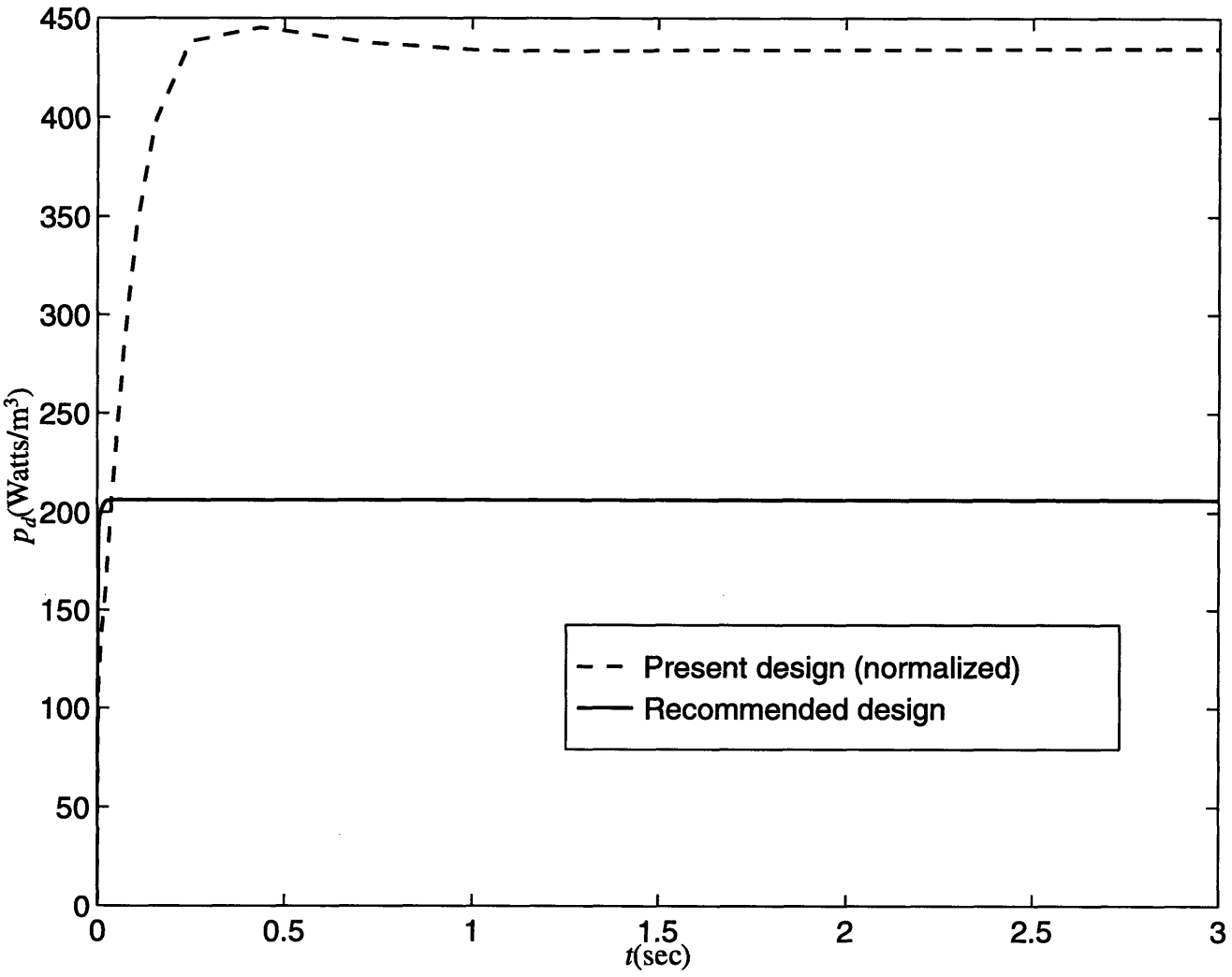

Figure 5-33: Power loss of ITER cable as a function of time for the present and recommended design. Since the recommended design has only half the twist pitch (final stage) as the present design, it should have, given no other improvements, only 1/4th the loss. Therefore the loss has been "normalized" to 1/4th the actual value to show the added improvement.

Although the reduction of the power loss is substantial, the discrepancy in the loss values are a bit misleading. The final twist pitch, L_{p5}, of the recommended design is only half that of the present design. A crude approximation to the effect of the reducing the twist pitch would be to hypothesize that the power density goes as L_{p5}^2. Therefore, the present design should yield a loss of 4 times the recommended design exclusively based upon the recution of the twist pitch. Therefore, the loss of the present cable is divided by 4 for a more accurate assessment of the advantage of the new design. The ratio of the steady-state power density for the new design over the old one is approximately 1:16 or 1:4 after the "normalization".

The difference in time constants is even more drastic. The time constant for the recommended design is in the vicinity of 1.5msec. The present design yielded an approximate τ of 130msec, which is the same order of magnitude of the derived time constant of the 192-strand cable data in the last section. The ratio of time constants is 1:87 or 1:22 after the nomalization. The reduction of the time constant is an even larger improvement over the savings in loss.

A general diagram which makes possible, at a glance, the regions where there is or is not a zero-crossing in α is shown in fig. 5-34. The ratios of the twist pitch (L_{p5}/L_{p4}) is plotted against the ratio of the two sub-radii(r_1/r_0). The location of the ITER cable is indicated by an 'X'. The diagram was based on the analytic expression in (5.18) and assumed that in general, $r_0 - 2r_1 \leq r \leq r_0 + 2r_1$.

5.6 Conclusion

A powerful algorithm which tracks the path of each individual strand in the 1152-strand ITER cable has been developed and implemented (the "cable-winder"). The winding laws, cast in the coordinate system of the cable, were extracted from the

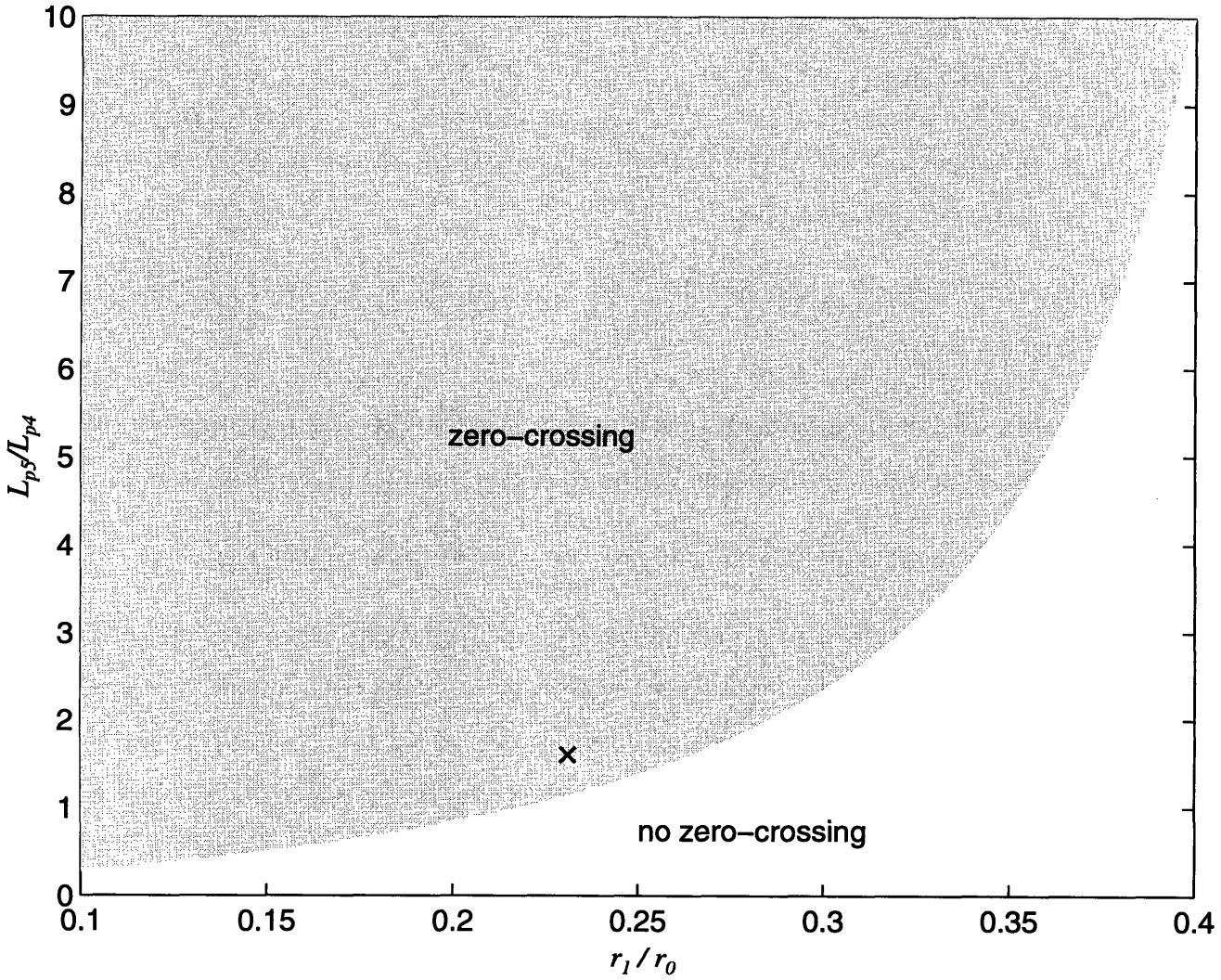

Figure 5-34: This diagram shows the set of values for the fourth and fifth twist pitch and the sub-radii that yield a zero-crossing in α. The 'X' marks the point where the ITER cable lies.

cable-winder code and utilized in the governing equations.

From the trajectory coefficients derived from the cable-winder, a 3D linear code which solves for current distributions and losses due to time-varying fields in an ITER cable has been developed, tested, and implemented. The following discoveries were made about the cable:

- Large transverse current densities are induced close to the inner rim of the cable which may create "hot spots".
- These "hot spots" are believed to be caused by the trajectory coefficient $\rho\dot{\psi}$ having a zero-value.
- A future cable design was proposed where there was no zero-crossings in $\rho\dot{\psi}$ yielding improved performance both in terms of loss and time constant.
- The loss curves vs. time show at least two distinct time constants.
- The dominant (long) time constant (an order of magnitude longer than the small time constant) is associated with the thin layer in the cable about the zero-crossing. It is much longer than the $n\tau$ value derived from power dissipation which implies that $n << 1$. Simulation of the full-size cable yielded $n = .067$ and data from the 192-strand experimental cable yielded $n = .18$.

Chapter 6

Conclusion

6.1 Summary

In the preceding chapters, we focussed on the modeling (chapter 2) and numerical analysis of frequently used composite superconductors. Some of these conductors are made of pure superconducting material (chapter 1) while others contain a mixture of superconductor and normalconducting material. Although the problems concerning various conductors may be geometrically different, the mathematical analysis is similar. The basic assumption of Carr's model, described in chapter 2, which was originally formulated for the multifilamentary strand, is to view the strand as a continuous media and derive averaged parameters and fields. The general problem is then extended to the applications of large cables. Our model takes advantage of the fact that these cables contain many strands and can thereby be modelled as a continuous media. Coupled with Maxwell's equations, the anisotropic and sometimes nonlinear constitutive relationship between σ and E, as derived by Carr and expanded by Rem, yield solutions for field and current distribution within the composite superconductor. With a strategic set of assumptions, an ordering system emerges, which

simplifies the mathematical analysis and yet includes most of the physics. This leads to an elegant set of governing equations which completely captures the geometry and the electromagnetic behavior of the system as pertinent to AC losses.

In chapter 4, the general set of equations, as well as the relevant boundary conditions, are applied to the development of a two-dimensional computer program. This code solves for problems that are naturally two-dimensional - in r and ϕ. Such geometries include multifilamentary strands and circular cables twisted with one twist pitch. The purpose of this code is to confirm the validity of the model and, at the same time, to contribute to the understanding of single strand AC losses. The form of the solutions for field and potential are written as infinite fourier series with harmonics in ϕ. This strategy decomposes the governing equations into a set of coupled one-dimensional ODE's in r. A software package named COLSYS, which uses the method of collocation, is used to solve the two-point boundary value problem. The nonlinear portion of the equations is dealt with by iterating solutions that were derived from a constant conductivity value based on the previous iteration. Results from the code are benchmarked against analytic solutions derived in chapter 3 as well as solutions found in firmly-established literature.

The full three-dimensional geometry of the ITER cable is treated in chapter 5. An innovative algorithm, which models the winding path of each of the 1152 strands in the cable, is used to extract exact strand trajectories required in the governing equations. An analytic approach to capturing the behavior of the windings is still in progress. However, an analytic expression for the azimuthal motion of the strands in the cable ($\rho\dot{\psi}$) has been derived and verified against the cable winder code results:

$$\rho\dot{\psi}(r,\phi,z) \approx (k_0 + \frac{k_1}{2})r - \frac{k_1}{2}\left(\frac{r_0^2 - r_1^2}{r}\right) \tag{6.1}$$

where k_0 and k_1 correspond to the pitch number of the last and second to last stages. r_0 and r_1 are the radii of rotation of the two stages. This implies that the electromagnetic behavior of the cable is dominated by the two last stages of a cable.

The cable is assumed to be infinitely long, which is a fairly good assumption as explained in chapter 3, and the cable is assumed to never saturate. The decision to keep the conductivity linear is based on results from the 2D code and it resolves the issue of whether a nonlinear conductivity is worth the price of computational inefficiency. In addition, the transverse conductivity is used as a fitting parameter since the experimental value is still a controversial subject.

In the attempt to compare AC loss calculations against preliminary data for an ITER subcable have yielded some surprising results. It turns out that the combinations of the twist pitches of the last two stages yields a zero-crossing in $\rho\dot{\psi}$. This zero-crossing leads to increased peaking of fields and loss around the region.

The other surprising bit of information comes from examining the time evolution of the power loss. It has been discovered that there are at least two dominant time constants in the system. There is a short time constant and a much longer one that dominates the behavior of the system. If the steady-state power loss is expressed as

$$p_d = \frac{\dot{B}^2}{\mu_0} n\tau \tag{6.2}$$

This yields a very low value for n. For the 192-strand cable used in experiments, the data yielded $n = .18$. For the full-size cable, the code yielded $n = .07$. Both these values are much smaller than for a helically twisted cable or strand where $n = 2$.

The hypothesis for such a small n value gives credit to the zero-crossing in α. Current is channeled into that region with a time constant inversely proportional to $\dot{\rho}^2$. This leads to a long τ since $\dot{\rho}^2$ is small. Although the currents are large there,

it occupies only a small portion of the total volume of the conductor. Therefore, in general,

$$n_{cable} << n_{strand} = 2 \tag{6.3}$$

6.2 Concluding remarks

The behavior of transport current in the ITER cable should be studied further. The numerics for this particular excitation have yet to be fully understood and, although not an important factor in the study of AC losses, should be a priority where ramp-rate limitations and stability are concerned.

Research on current redistribution in these large cables can take advantage of the work that has been done here. For instance, study of the effects of a nonlinear conductivity on current redistribution, which allows for saturation, can utilize the model formulated for this thesis. In addition, end conditions which account for joint effects, can be added to the existing 3D code. The current distributions generated from the code can be used for thermal and quench analysis.

Finally, there is progress on the development of an analytic model for the AC loss inside these large cables. With the assumption of weak shielding, there is hope that a closed-form solution for loss that is dependent on geometric factors will be achieved in the near future.

Bibliography

[1] Onnes, H., "Further experiments with liquid helium. C. On the change of the electric resistance of pure metals t very low temperatures etc. IV. The resistance of pure mercury at helium temperatures." **Leiden Comm.**, 120 b, 1911, pp. 3-5.

[2] Ciazynski, D. and B. Turck, "AC losses and current distribution in 40 KA NbTi and Nb3Sn Conductors for NET/ITER," **1992 ASC Conference**.

[3] Egorov, S., et al., "Interstrand coupling AC-losses in multistage cable-in-conduit superconductors," **Cryogenics**, v32, ICEC Supplement, 1992, pp. 439-442.

[4] Rem, P., *Numerical models for AC superconductors*, Thesis at the University of Twente - Netherlands, 1986.

[5] Sumiyoshi, F. et al., "Increase of coupling-current losses in superconducting cables due to first-stage cabling," **Cryogenics**, v26, Jan. 1986, pp. 39-43.

[6] Sumiyoshi, F. et al., "Numerical calculation method of inter-strand coupling current losses in superconducting conductors," **Cryogenics**, v29, July 1989, pp. 741-747.

[7] Thome, R. J., *Design Guidelines for the ITER Conductor*, ITER EDA Document, Ref. No. RJT93031006, March 10, 1993.

[8] Turck, B., "Transverse resistance in cable in conduit conductors: AC losses vs. current transfer", Paper presented at the **1992 ASC Conference**, Note P/EM 92-02.

[9] van de Klundert, L.J.M., "AC stability and AC loss in composite superconductors", **Cryogenics**, v31, July 1991, pp. 612-617.

[10] van de Klundert, L.J.M. et al., "Electromagnetic response of composite superconducting wires", **J. Engineering Mathematics**, v26, 1992, pp. 231-265.

[11] Wilson, M.N., *Superconducting Magnets*, Oxford University Press, Oxford, (1983).

[12] Carr, W.J., *AC Loss and Macroscopic Theory of Superconductors*, Gordon & Breach, New York, (1983).

[13] Hartmann, R.A., *A Contribution to the Understanding of AC Losses in Composite Superconductors*, Thesis at the University of Twente - Netherlands, 1989.

[14] Jackson, J.D., *Classical Electrodynamics*, Wiley, New York, (1962).

[15] Gung, C.Y., MITPFC Memo No. ITER/US/95/EV-MAG/C.Y.Gung/02.02/-1, Feb. 2, 1995.

[16] Painter, T.A., et al., "Manufacture and Verification Testing of Low-Resistance Nb_3Sn Joints for Cable-in-Conduit Conductors," **1994 ASC Conference**.

[17] Roovers, A., *An experimental study of AC losses in superconducting wires and cables*, Thesis at the University of Twente-Netherlands, 1989.

[18] Verweij, A., *Electrodynamics of superconducting cables in accelerator magnets*, Thesis at the Univrsity of Twente-Netherlands, 1995.

[19] Ascher, U. et al., "Collocation software for boundary-value ODE's," **ACM Trans. Math Software 7**, 1981, pp. 209-222.

[20] Bruzzone, P., *Coupling currents losses benchmark test*, addendum to the ITER EDA JCT Final Report, Feb. 1,1996.

[21] Chen, Y. and J. Freidberg,"A Method for Modeling the winding pattern of a large scale superconducting cable," to be published in **IEEE Trans. Magnetics - INTERMAG**, Sept. 1996.

[22] Sumiyoshi, F. et al., "On the distribution of a transport current inside a multifilamentary superconducting wire in a rapidly changing transverse magnetic field," **Cryogenics**, Mov. 1983, v23, pp.619-24.

[23] Ries, G., "AC-Losses in mutifilamentary superconductors at technical frequencies," **IEEE Trans. Magnetics**, vMAG-13, n1, Jan. 1977, pp.524-6.

[24] Turck, B., "Coupling losses in various outer normal layers surrounding the filament bundle of a superconducting composite," **J. Appl. Phys.**, 50(8), Aug. 1979, pp.5397-401.

[25] Duchateau, J.L. and B. Turck, **Cryogenics**, v14, 1974, p.545.

[26] Ito, D. et al., "The influence of filament bundle location on coupling losses in superconducting composites. Part I: mixed matrix conductor," **Cryogenics**, v23, Dec. 1983, pp.643-8.

[27] Tinkham, M., "AC losses in superconducting magnet suspensions for high-speed transportation," **J. Appl. Phys.**, v44, n5, May 1973, pp.2385-90.

[28] Ogasawara, T., et al., "Transient field losses in multifilamentary composite conductors carrying transport currents," **IEEE Trans. Magnetics**, vMAG-17, n1, Jan. 1981, pp. 967-70.

[29] Kim, Y. et al., "Magnetization and critical supercurrents," **Physical Review**, v129, n2, Jan. 1963, pp. 528-35.

[30] Kwabata, S. et al., "Interstrand coupling effect on losses and current distributions in superconducting cable conductors," **Cryogenics**, v34, n4, 1994, pp. .

[31] Schild, T., and D. Ciazynski, "A model for calculating AC losses in multistage superconducting cables," submitted to **Cryogenics**.

[32] Kwasnitza, K., **Cryogenics**, Nov. 1977, p.616.